天津大学博士学位论文

空间机构网格与刚性折纸的关联研究

Study on the Relationship between Mobile Assemblies of Spatial Linkages and Rigid Origami

学科专业：机械工程
研 究 生：张 霄
指导教师：陈 焱 教授

天津大学机械工程学院

2018 年 12 月

摘要

空间机构网格与刚性折纸凭借其优异的折叠特性，在航空航天、机器人等工程领域拥有巨大应用潜力。但是其运动的复杂性，使得寻求新型设计依然面临挑战。本文通过研究空间机构网格、厚板折纸与刚性折纸的内在联系，提出了刚性折纸到机构网格的基于厚板折纸的转化法和刚性折纸顶点拆分法，利用两种方法设计新型的空间机构网格、单自由度折纸以及具有平整展开表面的厚板折纸。其中，本文的主要研究内容如下：

首先，以四折痕厚板折纸为桥梁，提出四折痕刚性折纸到 Bennett 机构网格的转化法。将该方法应用至 Miura-ori 折纸和渐变的 Miura-ori 折纸中，得到由等杆长 Bennett 机构组成的可展机构网格。在互补型折纸中应用该方法，发现其三种不同的山谷线分布方式对应可形成拥有不同负杆长特征的 Bennett 机构网格。进一步将该转化法应用至 identical linkage-type 折纸上，得到一种新型的 Bennett 机构网格。

其次，基于前述转化法建立起 diamond 厚板折纸与面对称 Bricard 机构网格的运动等价关系。通过分析从 diamond 厚板折纸转化得到的机构网格的运动协调关系，发现两种由面对称 Bricard 机构组成的机构网格。其中一种机构网格的构造条件可用于改变 diamond 厚板折纸的扇形角和板厚。由此设计具有平整展开表面的厚板折纸。此外，还设计同时拥有平整展开表面和螺旋折叠构型的新型 diamond 厚板折纸，其在多单元扩展中可以保证无物理干涉。

最后，基于 diamond 折纸提出一种顶点拆分法，用于减少多自由度折纸的自由度数。在单顶点 diamond 折纸上应用其两种拆分方式，获得三种运动等价的折纸单元。将该方法应用至包含多顶点的 diamond 型折纸中，建立多组具有单自由度特征的基本折纸图案和大量单自由度折纸图案，并讨论了由四折痕和六折痕顶点组成的平面可折叠型折纸与由四折痕、五折痕和六折痕顶点组成的非平面可折叠折纸。此外，从 Bennett 机构建立 Waldron 混联六杆机构的过程中分析其对应厚板折纸的变化情况，提出厚板折纸去除铰链的方法。利用该方法可以去除厚板折纸中相邻两个四折痕顶点间的共用铰链，构造与其运动等价的六折痕厚板折纸，进一步构造出具有平整展开表面的厚板折纸。

本文基于前述转化法和顶点拆分法的研究，揭示了空间机构网格、厚板折纸与刚性折纸间的关系，为新型机构网格、刚性折纸和厚板折纸的设计提供新路径，有利于它们在工程中的应用。

关键词：刚性折纸，厚板折纸，空间机构网格，Bennett 机构，Bricard 机构，转化法，顶点拆分法

ABSTRACT

Mobile assemblies of spatial linkages and rigid origami are of superiorly foldable properties. Therefore, they have great potential in various engineering fields, such as aerospace and robotics. Due to the motion complexity of them, it is a challenge to seek for novel designs. In this dissertation, the relationships between mobile assemblies of spatial linkages, thick-panel origami and rigid origami are studied. *Transition technique* based on thick-panel origami and *vertex-splitting technique* are proposed to design new mobile assemblies of spatial linkages, one-DOF (degree of freedom) origami and thick-panel origami with flat-surface unfolded profiles. The major findings of this dissertation are as follows.

Firstly, the transition technique from four-crease origami patterns to mobile assemblies of Bennett linkages is developed by taking the thick-panel form of an origami pattern as an intermediate bridge. Applying this transition technique to the Miura-ori and graded Miura-ori patterns, assemblies of Bennett linkages with identical link lengths are obtain. Three cases of mountain-valley crease assignments of supplementary-type origami patterns correspond to different types of Bennett linkage assemblies with negative link lengths. And a new assembly of Bennett linkages is derived from the identical linkage-type origami pattern with the application of the transition technique.

Secondly, the kinematic equivalence between the diamond thick-panel origami and mobile assembly of plane-symmetric Bricard linkages is set up based on the transition technique. Two general cases of mobile assemblies of plane-symmetric Bricard linkages are discovered by analysing the compatibility of diamond assembly which is derived from a diamond thick-panel origami pattern. One of the newly-found mobile assemblies inspires the variation of the sector angle and thickness of diamond thick-panel origami pattern. Thus, new diamond thick-panel origami patterns with flat unfolded profiles and/or spirally folded configuration are invented, and the graded one can be extended infinitely without physical interference.

Finally, to reduce the number of DOF in the multi-DOF rigid origami pattern, a vertex-splitting technique including two splitting schemes on the diamond vertex are proposed to generate three types of unit patterns. Then, the technique is applied to the multi-vertex diamond origami pattern to produce several one-DOF basic assemblies and a number of one-DOF origami patterns. Two of the one-DOF origami patterns are discussed. One is flat-foldable origami pattern mixed with four-crease and six-crease vertices, and the other is non-flat-foldable origami pattern mixed with four-crease, five-crease, and six-crease origami vertices. Hinge-removing is proposed by analysing the relationship between the construction of Waldron's hybrid 6*R* linkage from Bennett linkages and the variation of their corresponding thick-panel origami pattern. This

indicates the thick-panel origami pattern with two four-crease vertices can be transformed into a kinematically equivalent pattern with six creases by removing the shared hinges to construct thick-panel origami patterns with flat-surface unfolded profiles.

Therefore, the research in this dissertation is based on the transition technique and vertex-splitting technique. It reveals the close relationships among mobile assemblies of spatial linkages, rigid origami and thick-panel origami, which offers approaches to propose the new designs, and facilitates their applications.

KEYWORDS: Rigid origami, thick-panel origami, mobile assembly of spatial linkages, Bennett linkage, Bricard linkage, transition technique, vertex-splitting technique

Contents

List of Figures

List of Tables

Notation

Parameters

a^{K}, b^{K}	Link lengths of Bennett linkage K in mobile assemblies
$a_{i(i+1)}$, $b_{i(i+1)}$, $c_{i(i+1)}$, $d_{i(i+1)}$	Link lengths of linkages between joint *i* and joint *i*+1
b	Number of bars in truss in Chapter 1 and 4
a_i, b_i, c_i, d_i, e_i, f_i, g_i, h_i, l_i	Creases of origami pattern or joints of linkage
j	Number of joints in truss in Chapter 1 and 4
m	Number of degrees of freedom
t_0, t_0'	The thickness of special panels in Chapter 4
$t_{i(i+1)}$, $t'_{i(i+1)}$	The thickness of panels in the single-vertex thick-panel origami between creases k_i and k_{i+1}
t_{P}	The total thickness of panel P
u^{K}, v^{K}, w^{K}	Link lengths of Bricard linkage K in mobile assembly corresponding to links with α^{K}, β^{K}, γ^{K}, respectively
x_i, y_i, z_i	x, y, z coordinate axis of system i
A, B, C, D, E, F, G, H, L, M, N, O, Q, R, S, T	The origami vertex and its corresponding spherical linkage; the thick-panel origami vertex and its corresponding spatial linkage
V_i	The points at the edge of an origami pattern in Chapter 4
W_i	The points out of plane to generate the equivalent truss form in Chapter 4
$\boldsymbol{I}_i$	Identity matrix
$\mathrm{P}^{\mathrm{K}}_{i(i+1)}$, P	The origami panels between creases k_i and k_{i+1} of origami vertex K. P is the central panel in Miura-ori pattern and diamond origami pattern
$\boldsymbol{Q}_{(i+1)i}$	3×3 transformation matrix from the ith coordinate system to the $i+1$th coordinate system
R_i	Offset of joint i
$\boldsymbol{T}_{(i+1)i}$	4×4 transformation matrix from the ith coordinate system to the $i+1$th coordinate system

Symbolic Variables

$\alpha_{i(i+1)}$	The twist or the angle from z_i to z_{i+1} about axis x_{i+1}
α, β, γ, δ	The sector angles of origami pattern, related to the twists of spatial linkage
α^{K}, β^{K}, γ^{K}	Twists of Bricard linkage K in the mobile assembly.

σ, τ, ρ, ν	Revolute variables in mobile assembly derived from the identical linkage-type origami pattern
$\theta_i^{\mathrm{K}}, \theta_i$	Kinematic variables in the mobile assembly
$\varphi_i^{\mathrm{K}}, \varphi_i$	The dihedral angle between two panels joined by a crease or the revolute joint i in vertex K.

Abbreviations

Be	Bennett linkage
Br	Plane-symmetric Bricard linkage
D-H notation	Denavit-Hartenberg notation
DOF	Degree of freedom
Wa	Waldron's hybrid 6*R* linkage

Chapter 1 Introduction

1.1 Background and Significance

Deployable structure is a type of transformable structures, which can vary their shape from a compact, packaged configuration to an operational, expanded configuration. In most cases, the packaged configuration is used for storage and transportation, while the expanded configuration is for work requirements. They are widely used in various engineering fields [1], such as aerospace (satellite antenna [2-7], solar panels [8] and wings [9]), civil engineering (shelter [10, 11], dome [12] and bridge [13, 14]), medical devices (origami stent graft [15], forceps [16]) and robotics [17-20]. According to the different morphology of their components, the structures can be divided into two types, the bar-like deployable structure composed of bar elements or lattices and the surface-like deployable structure composed of continuous surface elements. Among them, the mobile assembly of linkages and origami are the special cases of the respective types. Because of their low degrees of freedom (DOF) and superiorly foldable properties, they have attracted more and more attention, recently.

A mobile assembly of linkages is a network or tessellation of unit linkages. Once the unit linkage has a deployable property, the corresponding mobile assembly will enhance the deployable advantage. A typical unit is a scissor-like unit [21, 22], which has reliable synchronous movement, compactness and economic use of material. Those advantages make it the most widely used unit in the design of large-scale deployable structures, such as roofs [23, 24], shelters [10], antennas [6] and so on [25]. The other unit is one-DOF and single-loop spatial overconstrained linkage, including Bennett linkage [26], Myard linkage [27], Bricard linkage [28]. The number of DOF of this type linkages does not obey the mobility criterion, Grübler-Kutzbach criterion. Their motions are due to the specific geometric conditions. As the overconstrained geometry of the linkages can provide extra stiffness and the linkages can generate complicated three-dimensional motion with small number of bars, the mobile assembly of spatial overconstrained linkages has been of a great research interest. The tessellation method [29] is a well-explored method for the construction of mobile assemblies with three-dimensional overconstrained linkages. However, due to the highly nonlinear property of the compatibility conditions among the linkages in the assemblies, it is not easy to find a new assembly made from nesting the overconstrained linkages together while retaining mobility.

On the other hand, origami is a paper folding art, which can transform a paper sheet into a three-dimensional structure. There are a large number of origami patterns to form different shapes. It can fold a large-scale surface into a smaller one, which makes it useful in designing deployable structures. Recent studies of origami have been done in a variety of engineering fields, typically in metamaterials [30, 31] and robotics [32-34]. Since the traditional materials of the deployable structures are rigid, rigid origami, where its facets can rotate around the crease and no deformation occurs on facets, has received much attention. One-DOF Miura-ori [35, 36] has been extensively studied for the reason that it has simple structure and can be easily controlled. Multi-DOF origami has been widely used to transformable robots due to its deployment of variable configurations. However, it is always a great challenge in designing of one-DOF origami patterns and controlling the multi-DOF ones.

In general, origami structures are with zero-thickness panels. Then, one rigid origami vertex can be considered as a spherical linkage by regarding the crease lines and the rigid panels as revolute joints and links [37, 38], respectively. Hence, a rigid origami pattern with multiple vertices is kinematically equivalent to a mobile assembly of spherical linkages [39]. Kinematic theories of mechanism can be used to analyse the rigid origami. Yet, some engineering applications requiring high strength or rigidity cannot ignore the thickness of the material. One effective method is to offset the revolute joints on the surfaces of thick panels so that their thickness can be accommodated [40]. The generated thick-panel origami has been proven kinematically equivalent to the overconstrained linkages. Therefore, the study of relationships between rigid origami and mobile assembly of spatial linkages with the thick-panel form as the intermediate bridge can offer a new way to design the assembly of spatial linkages from the origami perspective, while the analysis of assembly of linkage with the kinematic theory of mechanism can widen the design space of origami pattern. Such study will facilitate their applications.

1.2 Review of Previous Works

1.2.1 Kinematic Analysis Theory in Mechanism

1.2.1.1 Matrix Method

Matrix method was established by Denavit and Hartenberg [41], which is very effective in analysis of spatial linkages. The setup of each coordinate system is shown in Fig. 1-1 [42]. The axis z_i is along the axis of i th revolute joint (R joint); the axis x_i is along the common normal line from z_{i-1} to z_i; the axis y_i can be determined by the right-hand rule; $a_{i(i+1)}$ is the normal distance between axes z_i and z_{i+1}; $\alpha_{i(i+1)}$ is the angle between z_i and z_{i+1} measured from z_i to z_{i+1} along the positive direction of x_{i+1}; R_i is the normal distance between axes x_i and x_{i+1}, positive along the axis z_i; θ_i is the angle between x_i and x_{i+1} measured from x_i to x_{i+1} along the positive direction of z_i.

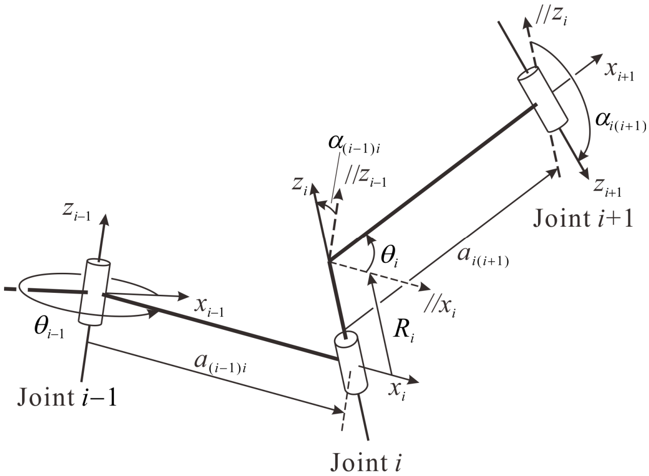

Fig. 1-1 D-H notation of two links connected by a revolute joint.

For a single closed loop linkage consisted of n links, the product of the transform matrices equals to the 4×4 identity matrix $\boldsymbol{I}_4$, which is the closure equation, as

$$\boldsymbol{T}_{21}\boldsymbol{T}_{32}\cdots\boldsymbol{T}_{n(n-1)}\boldsymbol{T}_{1n}=\boldsymbol{I}_4\,. \tag{1-1}$$

where the transformation matrix $\boldsymbol{T}_{(i+1)i}$ is transforming the i th coordinate system to the $i+1$ th coordinate system, as

$$\boldsymbol{T}_{(i+1)i}=\begin{bmatrix}\cos\theta_i & -\cos\alpha_{i(i+1)}\sin\theta_i & \sin\alpha_{i(i+1)}\sin\theta_i & a_{i(i+1)}\cos\theta_i\\ \sin\theta_i & \cos\alpha_{i(i+1)}\cos\theta_i & -\sin\alpha_{i(i+1)}\cos\theta_i & a_{i(i+1)}\sin\theta_i\\ 0 & \sin\alpha_{i(i+1)} & \cos\alpha_{i(i+1)} & R_i\\ 0 & 0 & 0 & 1\end{bmatrix}. \tag{1-2}$$

When $i+1>n$, it is replaced by 1. The inverse transformation can be expressed as

$$\boldsymbol{T}_{i(i+1)}=\boldsymbol{T}_{(i+1)i}^{-1}=\begin{bmatrix}\cos\theta_i & \sin\theta_i & 0 & -a_{i(i+1)}\\ -\cos\alpha_{i(i+1)}\sin\theta_i & \cos\alpha_{i(i+1)}\cos\theta_i & \sin\alpha_{i(i+1)} & -R_i\sin\alpha_{i(i+1)}\\ \sin\alpha_{i(i+1)}\sin\theta_i & -\sin\alpha_{i(i+1)}\cos\theta_i & \cos\alpha_{i(i+1)} & -R_i\cos\alpha_{i(i+1)}\\ 0 & 0 & 0 & 1\end{bmatrix}. \tag{1-3}$$

Due to the axes of revolute joints in spherical linkage intersecting at a point, the distances and the offsets between adjacent links are zero. Thus, Eq. (1-1) reduces to

$$\boldsymbol{Q}_{21}\boldsymbol{Q}_{32}\cdots\boldsymbol{Q}_{n(n-1)}\boldsymbol{Q}_{1n}=\boldsymbol{I}_3\,, \tag{1-4}$$

where $\boldsymbol{I}_3$ represents the 3×3 identity matrix,

$$\boldsymbol{Q}_{(i+1)i}=\begin{bmatrix}\cos\theta_i & -\cos\alpha_{i(i+1)}\sin\theta_i & \sin\alpha_{i(i+1)}\sin\theta_i\\ \sin\theta_i & \cos\alpha_{i(i+1)}\cos\theta_i & -\sin\alpha_{i(i+1)}\cos\theta_i\\ 0 & \sin\alpha_{i(i+1)} & \cos\alpha_{i(i+1)}\end{bmatrix} \tag{1-5}$$

and

$$\boldsymbol{Q}_{i(i+1)} = \boldsymbol{Q}_{(i+1)i}^{-1} = \begin{bmatrix} \cos\theta_i & \sin\theta_i & 0 \\ -\cos\alpha_{i(i+1)}\sin\theta_i & \cos\alpha_{i(i+1)}\cos\theta_i & \sin\alpha_{i(i+1)} \\ \sin\alpha_{i(i+1)}\sin\theta_i & -\sin\alpha_{i(i+1)}\cos\theta_i & \cos\alpha_{i(i+1)} \end{bmatrix}. \tag{1-6}$$

Therefore, based on the Eq. (1-1) or Eq. (1-4), the motion behaviors of spatial linkages can be analysed.

1.2.1.2 Truss Method

Maxwell has defined a frame as ‘a system of lines connecting a number of points’ and a stiff frame as ‘one in which the distance between any two points cannot be altered without altering the length of one or more of the connecting lines of the frame’ [43]. In general, a stiff frame with j nodes in three-dimensional space requires $3j-6$ bars. The mobility of one frame with j nodes and b bars can be derived from

$$m = 3j - 6 - b. \tag{1-7}$$

However, this criterion does not contain the detailed topological and geometric information, which makes it difficult to calculate the accurate mobility of overconstrained linkages.

Yang et al. [44] proposed the transformation method from the linkage to truss. He uses Maxwell’s rule and the rank of the equilibrium matrix [45] to determine the mobility of overconstrained linkages. The cases of truss form of one link with two *R*-joints are shown in Fig. 1-2, where a straight-line represents a bar and a circle represents a node which is an *S*-joint, and a straight bar with two nodes at the ends represents an *R*-joint, such as joint A represented by AA'. For a generally straight bar with two *R*-joints, it can be transformed into a truss tetrahedron, as shown in Fig. 1-2(a). When the axes of the two *R*-joints intersect, the equivalent truss form is a triangle, as shown in Fig. 1-2(b). For the two *R*-joints with parallel axes, all bars in the plane can generate instantaneous mobility, as shown in Fig. 1-2(c). An arbitrary point out of the plane is introduced to generate the equivalent truss form, as shown in Fig. 1-2(d).

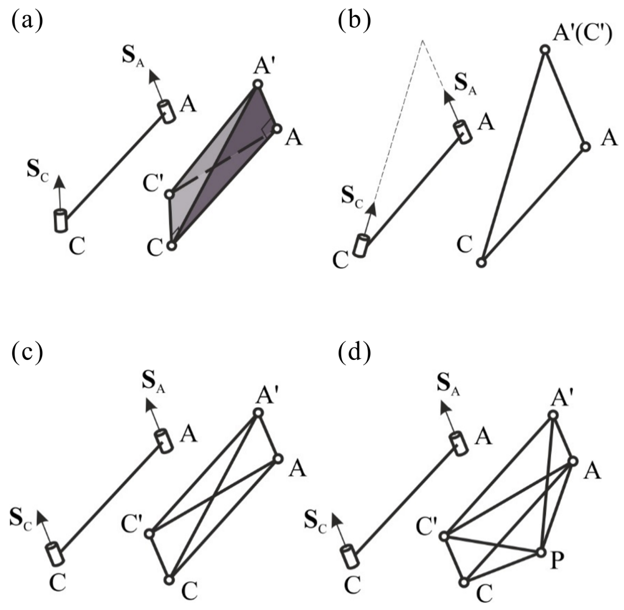

Fig. 1-2 One link with two R-joints proposed by Yang et al. [44]. (a) General case; (b) two intersecting revolute axes; (c) two parallel revolute axes with an instantaneous mobility; (d) two parallel revolute axes.

For a statically indeterminate truss, its mobility cannot be determined by Eq. (1-7). Therefore, the equilibrium equation [46] has to be considered. For a truss consisting of b bars and j joints, the equilibrium equations are obtained as

$$\boldsymbol{At} = \boldsymbol{f} \tag{1-8}$$

where $\boldsymbol{A}$ is the $3j \times b$ equilibrium matrix, $\boldsymbol{t}$ is a $b \times 1$ vector of bar axial forces and $\boldsymbol{f}$ is a $3j \times 1$ vector of node forces. Here, the truss does not have external forces, i.e., $\boldsymbol{f} = 0$. Hence, Eq. (1-8) becomes

$$\boldsymbol{At} = 0 \tag{1-9}$$

If r is the rank of matrix $\boldsymbol{A}$, the number of self-stresses is

$$s = b - r \tag{1-10}$$

and the number of mobility is

$$m = 3j - 6 - r\ . \tag{1-11}$$

According to the values of s and m, a truss can be divided into four classes [44, 47]:

$s = 0$, $m = 0$: Both statically and kinematically determinate structures, a normal structure;

$s = 0$, $m > 0$: Statically overdeterminate and kinematically indeterminate structures, a non-overconstrained mechanism;

$s > 0$, $m = 0$: Statically indeterminate and kinematically overdeterminate structures;

$s > 0$, $m > 0$: Both statically and kinematically indeterminate structures, an overconstrained mechanism.

The truss method has been applied to calculate the mobility of mechanism, such as the mobile assemblies of spatial linkages, polyhedrons [48, 49]. As one rigid origami can be regarded as a mechanism, the truss method can be used to calculate the mobility of a rigid origami, such as the triangular Resch pattern [50].

1.2.2 Spatial Overconstrained Linkages and Mobile Assemblies

1.2.2.1 Spatial Overconstrained Linkages

Mobility or DOF of one spatial linkage is the number of independent variables that must be considered for defining its configuration. It can be determined by the Grübler-Kutzbach criterion [51]:

$$m = 6(n-g-1)+\sum_{i=1}^{g} f_i \,, \tag{1-12}$$

where m is the number of DOFs, n is the number of members of mechanism, g is the number of joints and f_i is connectivity of the i th joint. The spatial overconstrained linkages are mobile without satisfying the mobility criterion in Eq.(1-12). The single closed-loop overconstrained linkage is a simple type of overconstrained mechanism. Since the first overconstrained linkage, Sarrus linkage [52, 53], was designed in 1853, the research on overconstrained mechanism has been sustained for more than 160 years. During this period, a large number of single closed-loop overconstrained linkages with one-DOF were constructed, including Bennett linkage [26, 54], Myard 5*R* linkage [27], Goldberg 5*R* linkage [55], Goldberg 6*R* linkage [55], Bricard 6*R* linkages [28, 56] and so on. These overconstrained mechanisms can be mainly classified into Bennett linkage, Bennett-based overconstrained linkages and Bricard 6*R* linkages.

(1) Bennett linkage

Bennett linkage [26] is a special overconstrained linkage with four links and four revolute joints. The joint axes of this linkage are neither parallel nor concurrent. According to the D-H notation [41], the coordinate systems are constructed, as shown in Fig. 1-3. Its geometric parameters satisfy the following conditions

$$a_{12}=a_{34}=a,\ a_{23}=a_{41}=b, \tag{1-13a}$$

$$\alpha_{12}=\alpha_{34}=\alpha,\ \alpha_{23}=\alpha_{41}=\beta, \tag{1-13b}$$

$$\frac{a}{\sin\alpha}=\frac{b}{\sin\beta}, \tag{1-13c}$$

$$R_i = 0\ (i=1,2,3,4). \tag{1-13d}$$

Its corresponding closure equations are

$$\theta_1 + \theta_3 = 2\pi,\ \theta_2 + \theta_4 = 2\pi, \tag{1-14a}$$

$$\tan\frac{\theta_1}{2}\tan\frac{\theta_2}{2} = \frac{\sin\frac{1}{2}(\beta+\alpha)}{\sin\frac{1}{2}(\beta-\alpha)}. \tag{1-14b}$$

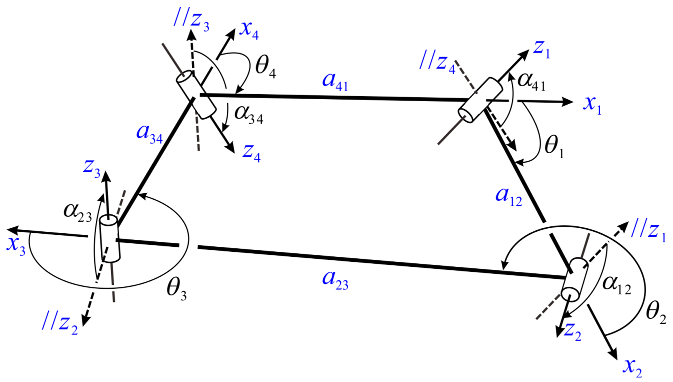

Fig. 1-3 The Bennett linkage.

(2) Bennett-based overconstrained linkages

The Bennett linkage can be regarded as a building-block, which can be used to construct new overconstrained linkages with five or six revolute joints. Goldberg 5*R* linkage [55] is constructed by combing two Bennett linkages in three steps. First, a certain link of each linkage (two links) are coincident. Second, two adjacent links are arranged in line. Third, lock the adjacent links and remove the common link. Then, a Goldberg 5*R* linkage is constructed, as shown in Fig. 1-4. By extending this method, Goldberg 6*R* linkages [55, 57] are proposed. Based on the Goldberg 5*R* linkage, Wohlhart [58] generalised it and constructed a Wohlhart double-Goldberg linkage by combining two properly Goldberg 5*R* linkages face to face and eliminating two shared links. By combing a subtractive Goldberg 5*R* linkages and a Goldberg 5*R* linkage through shared link-pair or shared Bennett-linkage, a family of double-Goldberg 6*R* linkages [59] constructed including the double subtractive Goldberg 6*R* linkage [60].

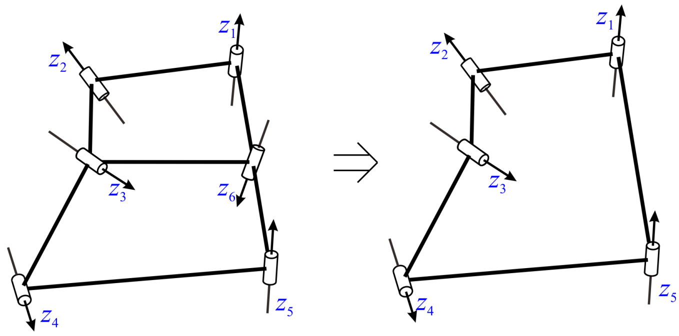

Fig. 1-4 The Goldberg 5*R* linkage.

Waldron's hybrid 6*R* linkage [61, 62] with revolute joints is an overconstrained linkage, which is made from two Bennet linkage arranged in space to make them share a common axis, as the revolute joint a_1/b_1 in Fig. 1-5. Then adding the links along the axes of joints a_2, a_4, b_2, b_4, and adding the common-perpendicular links between axes of joints a_2, b_4 and a_4, b_2, replacing the old links connected to the shared joint a_1/b_1 to construct an assembly of Bennett linkages. The shared joint a_1/b_1 and its connected links are then removed to form a 6*R* overconstrained linkage.

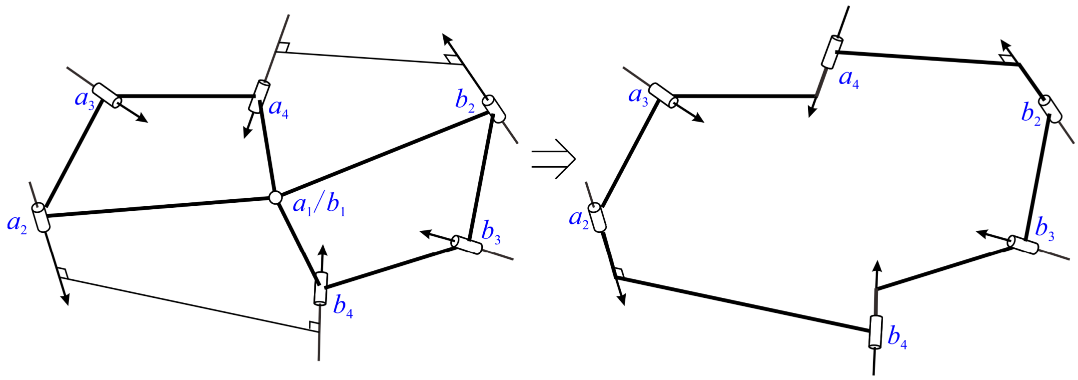

Fig. 1-5 The Waldron's hybrid 6*R* linkage from two Bennett linkages.

Recently, Song, Feng and Chen [63] proposed a network of four Bennet linkages. The network can be reconfigured among five types of overconstrained linkages by rigidifying some of the eight joints, including the generalized Goldberg 5*R* linkage [58], generalized variant of the L-shape Goldberg 6*R* linkage [55], Waldron's hybrid 6*R* linkage [61], isomerized case of the generalized L-shape Goldberg 6*R* linkage [64], and generalized Wohlhart's double-Goldberg 6*R* linkage [58]. Besides, Guo and Song [65] designed a series of spatial single-loop overconstrained linkages by combining Bennett linkages and use screw theory to analyse their mobility.

As the Bennett-based overconstrained linkages are constructed by regarding the Bennett linkage as construction unit, their geometric condition should satisfy that of Bennett linkages.

(3) Bricard 6*R* linkages

The family of overconstrained 6*R* linkages was proposed by Bricard [28, 66] consisting of six types, as shown in Fig. 1-6. Their geometric conditions were summarised [67] as follows.

For the general line-symmetric case,

$$a_{12} = a_{45},\ a_{23} = a_{56},\ a_{34} = a_{61}, \tag{1-15a}$$

$$\alpha_{12} = \alpha_{45},\ \alpha_{23} = \alpha_{56},\ \alpha_{34} = \alpha_{61}, \tag{1-15b}$$

$$R_1 = R_4, \; R_2 = R_5, \; R_3 = R_6. \tag{1-15c}$$

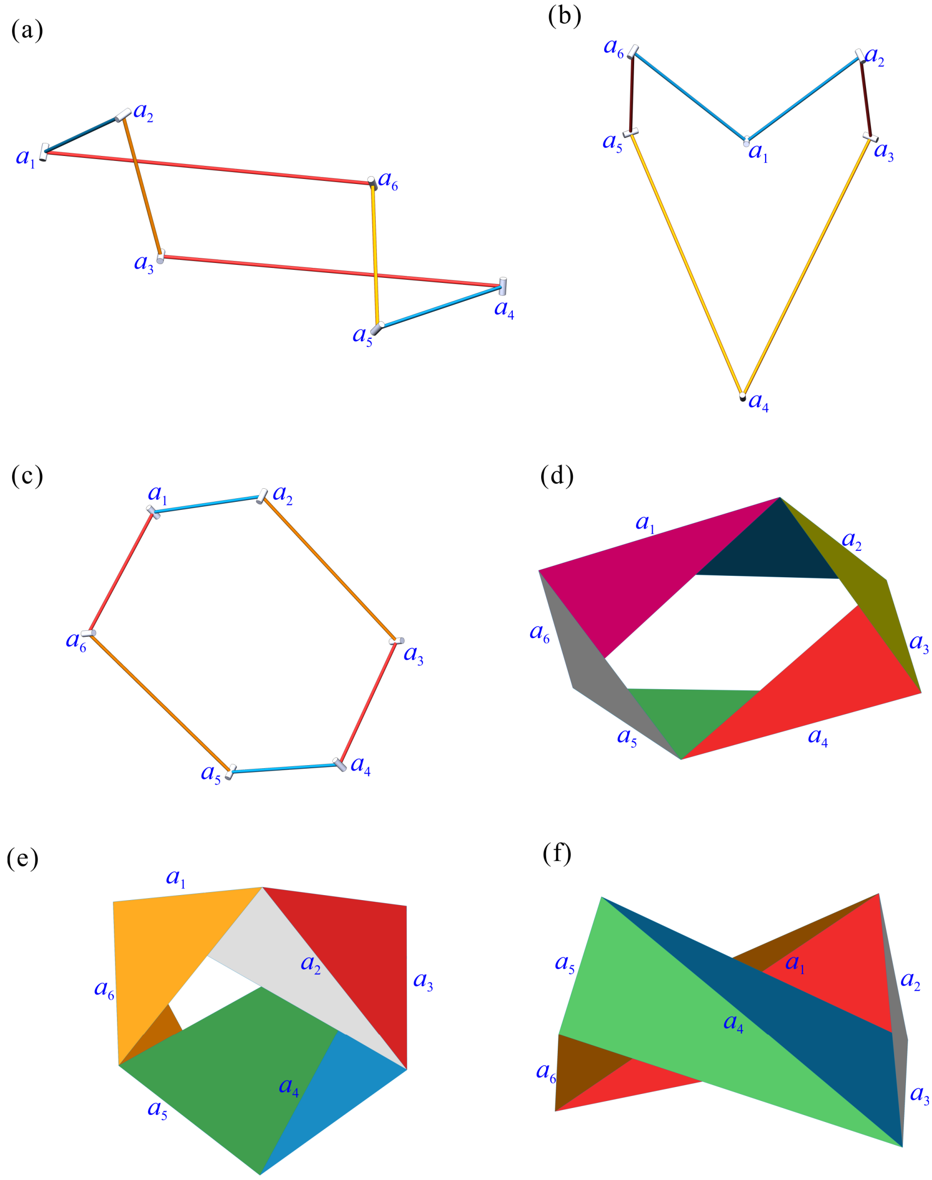

Fig. 1-6 Bricard 6*R* linkages: (a) the general line-symmetric case, (b) the general plane-symmetric case, (c) the trihedral case, (d) the line-symmetric octahedral case, (e) the plane-symmetric octahedral case, and (f) the doubly collapsible octahedral case.

For the general plane-symmetric case,

$$a_{12} = a_{61}, \; a_{23} = a_{56}, \; a_{34} = a_{45}, \tag{1-16a}$$

$$\alpha_{12} + \alpha_{61} = \pi, \; \alpha_{23} + \alpha_{56} = \pi, \; \alpha_{34} + \alpha_{45} = \pi, \tag{1-16b}$$

$$R_1 = R_4 = 0, \; R_2 = R_6, \; R_3 = R_5. \tag{1-16c}$$

For the trihedral case,

$$a_{12}^2 + a_{34}^2 + a_{56}^2 = a_{23}^2 + a_{45}^2 + a_{61}^2, \tag{1-17a}$$

$$\alpha_{12}=\alpha_{34}=\alpha_{56}=\frac{\pi}{2},\ \alpha_{23}=\alpha_{45}=\alpha_{61}=\frac{3\pi}{2}, \tag{1-17b}$$

$$R_i=0\ \ (i=1,2,\cdots,6). \tag{1-17c}$$

For the line-symmetric octahedral case,

$$a_{12}=a_{23}=a_{34}=a_{45}=a_{56}=a_{61}=0, \tag{1-18a}$$

$$R_1+R_4=R_2+R_5=R_3+R_6=0. \tag{1-18b}$$

For the plane-symmetric octahedral case,

$$a_{12}=a_{23}=a_{34}=a_{45}=a_{56}=a_{61}=0, \tag{1-19a}$$

$$R_4=-R_1,\ R_2=-R_1\frac{\sin\alpha_{34}}{\sin(\alpha_{12}+\alpha_{34})},\ R_3=-R_1\frac{\sin\alpha_{12}}{\sin(\alpha_{12}+\alpha_{34})}, \tag{1-19b}$$

$$R_5=-R_1\frac{\sin\alpha_{61}}{\sin(\alpha_{45}+\alpha_{61})},\ R_3=-R_1\frac{\sin\alpha_{45}}{\sin(\alpha_{45}+\alpha_{61})}. \tag{1-19c}$$

For the doubly collapsible octahedral case,

$$a_{12}=a_{23}=a_{34}=a_{45}=a_{56}=a_{61}=0, \tag{1-20a}$$

$$R_1R_3R_5+R_2R_4R_6=0. \tag{1-20b}$$

A systematic analysis of all the six Bricard linkages was done by Baker [56]. Appropriate sets of independent closure equations were constructed to delineate them. Phillips [68] reviewed the Bricard linkages and showed their relationship with the other overconstrained linkages. Wohlhart [69] concentrated on the orthogonal Bricard linkage and found two distinct types of this linkage. Chai and Chen [70] focused on the line-symmetric octahedral case of Bricard linkage and generated its kinematic paths and structural closure by analysing its closure equation with the matrix method. In addition, they discussed the bifurcation of a line and plane symmetric Bricard linkage and provided the solution to avoid bifurcation by analysing its closure equations [71]. Song and Chen [72] carried out the kinematic study of the original and revised general line-symmetric Bricard 6*R* linkages. Recently, Feng and Chen [73] derived the explicit solutions from closure equations of the plane-symmetric Bricard linkage. They indicated that the plane-symmetric Bricard linkage can bifurcate to the Bennett linkage, which expresses a comprehensive understanding of plane-symmetric Bricard linkage.

Some other special linkages are also studied, such as Altmann linkage, Schatz linkage, Wohlhart 6*R* linkage and threefold-symmetric Bricard linkage. Altmann linkage [74, 75] is a special case of the line-symmetric Bricard linkage with the geometric conditions as follows.

$$a_{12}=a_{45}=a,\ a_{23}=a_{56}=0,\ a_{34}=a_{61}=b, \tag{1-21a}$$

$$\alpha_{12}=\alpha_{45}=\frac{\pi}{2},\ \alpha_{23}=\alpha_{56}=\frac{\pi}{2},\ \alpha_{34}=\alpha_{61}=\frac{3\pi}{2}, \tag{1-21b}$$

$$R_1 = R_2 = R_3 = R_4 = R_5 = R_6 = 0. \tag{1-21c}$$

Schatz linkage [68] was discovered by Schatz which is derived from a special case of the trihedral Bricard linkage with the geometric conditions, as expressed in Eqs. (1-22a) to (1-22c). This linkage has special engineering applications whose name is Turbula machine for mixing fluids and powders.

$$a_{12} = a_{56} = 0,\ a_{23} = a_{34} = a_{45} = a,\ a_{61} = \sqrt{3}a, \tag{1-22a}$$

$$\alpha_{12} = \alpha_{23} = \alpha_{34} = \alpha_{45} = \alpha_{56} = \frac{\pi}{2},\ \alpha_{61} = 0, \tag{1-22b}$$

$$R_1 = -R_6,\ R_2 = R_3 = R_4 = R_5 = 0. \tag{1-22c}$$

Wohlhart 6*R* linkage [76] can be regarded as a generalisation of trihedral Bricard 6*R* linkage whose parameters satisfy

$$a_{12} = a_{23},\ a_{34} = a_{45},\ a_{56} = a_{61}, \tag{1-23a}$$

$$\alpha_{12} = 2\pi - \alpha_{23},\ \alpha_{34} = 2\pi - \alpha_{45},\ \alpha_{56} = 2\pi - \alpha_{61}, \tag{1-23b}$$

$$R_6 = -R_2 - R_4,\ R_1 = R_3 = R_5 = 0. \tag{1-23c}$$

Threefold-symmetric Bricard linkage [77] is derived from combining the general plane-symmetric and trihedral Bricard linkages, whose geometric parameters satisfy

$$a_{12} = a_{23} = a_{34} = a_{45} = a_{56} = a_{61} = a, \tag{1-24a}$$

$$\alpha_{12} = \alpha_{34} = \alpha_{56} = \alpha,\ \alpha_{23} = \alpha_{45} = \alpha_{61} = 2\pi - \alpha, \tag{1-24b}$$

$$R_i = 0\ \ (i = 1, 2, \cdots, 6). \tag{1-24c}$$

1.2.2.2 Mobile Assemblies of Spatial Overconstrained Linkages

Although the engineering application of spatial overconstrained linkages is limited, mobile assembly of spatial overconstrained linkages has been of a great research interest. The reasons are not only the kinematic challenge, but also the application potential for a deployable structure with high expansion to package ratio. The construction with tessellation method [29] and the mobile connections [78], provide effective ways for the design of large-scale mobile assemblies, such as Bennett-linkage assemblies [79-82], Myard-linkage assemblies [83, 84] and Bricard-linkage assemblies [85], which promote the development of deployable structures for engineering application.

Tilling is also called tessellation. A plane tiling is a plane covered by a countable family of closed sets without gaps and overlaps, such as the honeycomb of bees. Chen [29] indicated three ways to cover the plane with identical units: tilings (3^6), (4^4) and (6^3) which make the units spread in three, four and six directions, respectively, as shown in Fig. 1-7. Here, for instance, tiling (6^3) represents each of the points is surrounded by three hexagons, where 6 is the number of hexagonal sides and it also represents the number of spreading directions. The superscript 3 is the number of hexagons. The unit named tessellation unit can be a repeatable pattern or motif, which can be constructed by the basic linkage, e.g., Bennett linkage and Myard linkage, or the assembly of a set of linkages. The tessellation method for mobile assembly including three steps: construction of units, selection of spreading ways from three tilings and validation of compatibility.

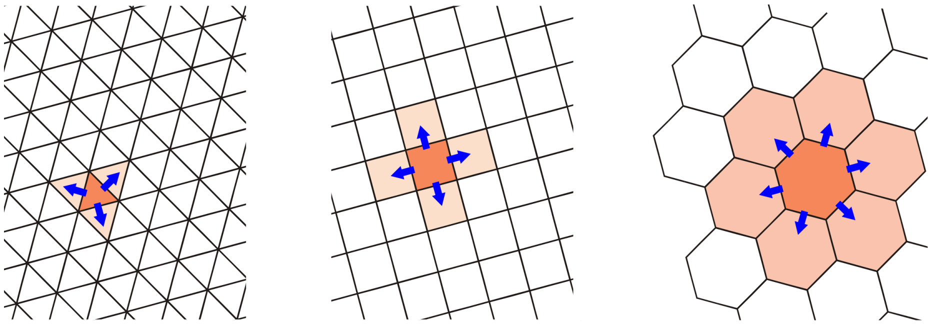

(3^6) (4^4) (6^3)

Fig. 1-7 Three types of tilings with identical units summarized by Chen [29].

Chen and You [79] have constructed unit motif of Bennett linkages with overlapping based on the tiling (4^4). They further designed a basic mobile assembly which can be deployed into flat or arch surfaces with different parameters, other three mobile assemblies of Bennett linkages [80] are derived from considering the links with negative lengths. The schematic diagrams of the four distinct mobile assemblies of Bennett linkages are shown in Fig. 1-8 and Fig. 1-9, where the black circles and black lines show the constructions of their corresponding mobile assemblies, while gray circles and gray lines show the tessellation of mobile assemblies. Their twists α_{K} and β_{K} of each link should satisfy the conditions in Eqs. (1-25) to (1-29).

Twists of case 1 Bennett linkage mobile assembly with type I and type II guidelines satisfy

$$\begin{aligned}&\alpha^{\mathrm{A}}=-\alpha^{\mathrm{B}}=\alpha^{\mathrm{E}}=\alpha_{i-1},\ \beta^{\mathrm{A}}=-\beta^{\mathrm{B}}=\beta^{\mathrm{E}}=\beta_{i-1},\\&\alpha^{\mathrm{D}}=\alpha^{\mathrm{C}}=\alpha^{\mathrm{F}}=\alpha_{i},\ \beta^{\mathrm{D}}=\beta^{\mathrm{C}}=\beta^{\mathrm{F}}=\beta_{i},\\&\alpha^{\mathrm{L}}=-\alpha^{\mathrm{H}}=\alpha^{\mathrm{G}}=\alpha_{i+1},\ \beta^{\mathrm{L}}=-\beta^{\mathrm{H}}=\beta^{\mathrm{G}}=\beta_{i+1}.\end{aligned}\tag{1-25}$$

Twists of case 2 Bennett linkage mobile assembly with type II guidelines satisfy

$$\begin{aligned}&\alpha^{\mathrm{A}}=-\alpha^{\mathrm{B}}=\alpha^{\mathrm{E}}=\alpha_{i-1},\ \beta^{\mathrm{A}}=-\beta^{\mathrm{B}}=\beta^{\mathrm{E}}=\beta_{i-1},\\&-\alpha^{\mathrm{D}}=\alpha^{\mathrm{C}}=-\alpha^{\mathrm{F}}=\alpha_{i},\ -\beta^{\mathrm{D}}=\beta^{\mathrm{C}}=-\beta^{\mathrm{F}}=\beta_{i},\\&\alpha^{\mathrm{L}}=-\alpha^{\mathrm{H}}=\alpha^{\mathrm{G}}=\alpha_{i+1},\ \beta^{\mathrm{L}}=-\beta^{\mathrm{H}}=\beta^{\mathrm{G}}=\beta_{i+1}.\end{aligned} \tag{1-26}$$

Twists of case 3 Bennett linkage mobile assembly with type I guidelines satisfy

$$\begin{aligned}&\alpha^{\mathrm{A}}=\alpha^{\mathrm{B}}=\alpha^{\mathrm{E}}=\alpha_{i-1},\ \beta^{\mathrm{A}}=\beta^{\mathrm{B}}=\beta^{\mathrm{E}}=\beta_{i-1},\\&\alpha^{\mathrm{D}}=\alpha^{\mathrm{C}}=\alpha^{\mathrm{F}}=\alpha_{i},\ \beta^{\mathrm{D}}=\beta^{\mathrm{C}}=\beta^{\mathrm{F}}=\beta_{i},\\&\alpha^{\mathrm{L}}=\alpha^{\mathrm{H}}=\alpha^{\mathrm{G}}=\alpha_{i+1},\ \beta^{\mathrm{L}}=\beta^{\mathrm{H}}=\beta^{\mathrm{G}}=\beta_{i+1}.\end{aligned} \tag{1-27}$$

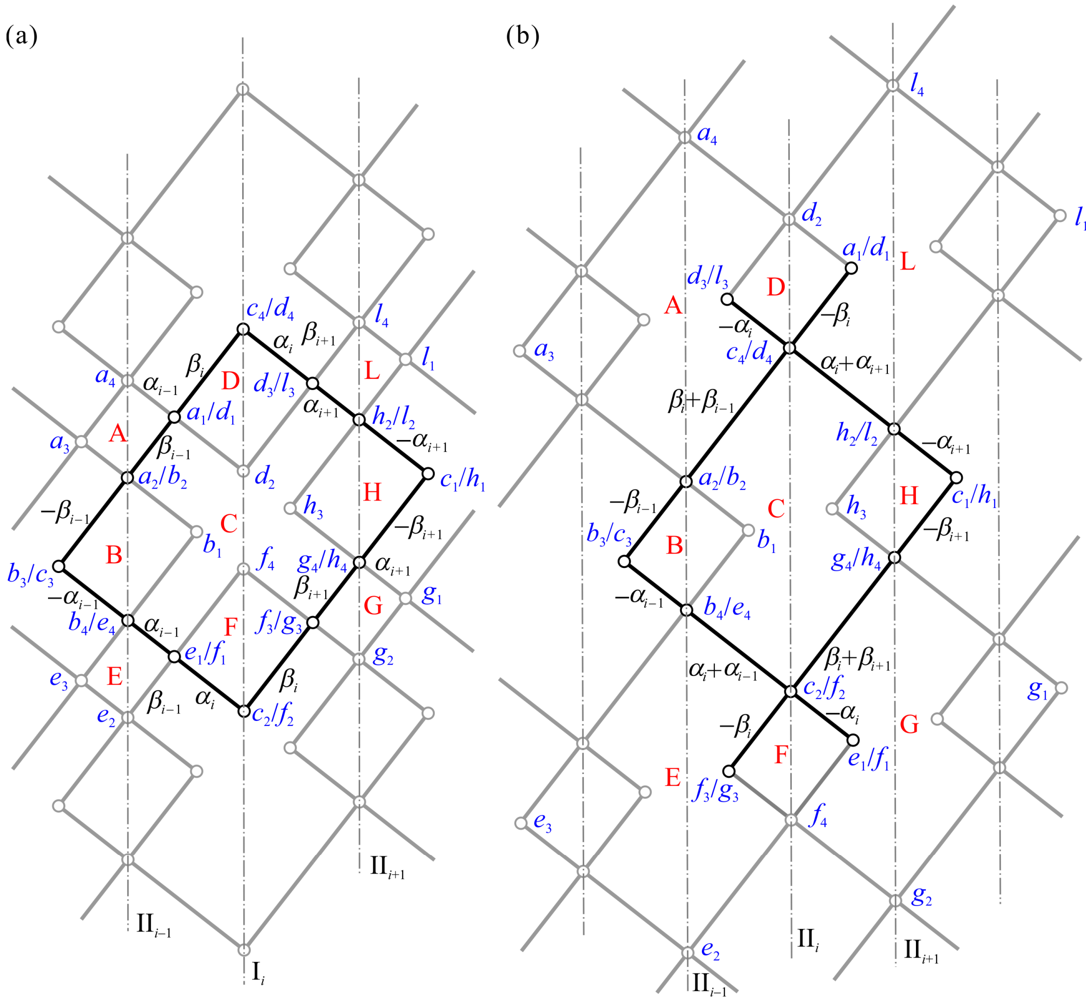

Fig. 1-8 Four cases of mobile assemblies of Bennett linkage. (a) Case 1, (b) case 2 mobile assemblies.

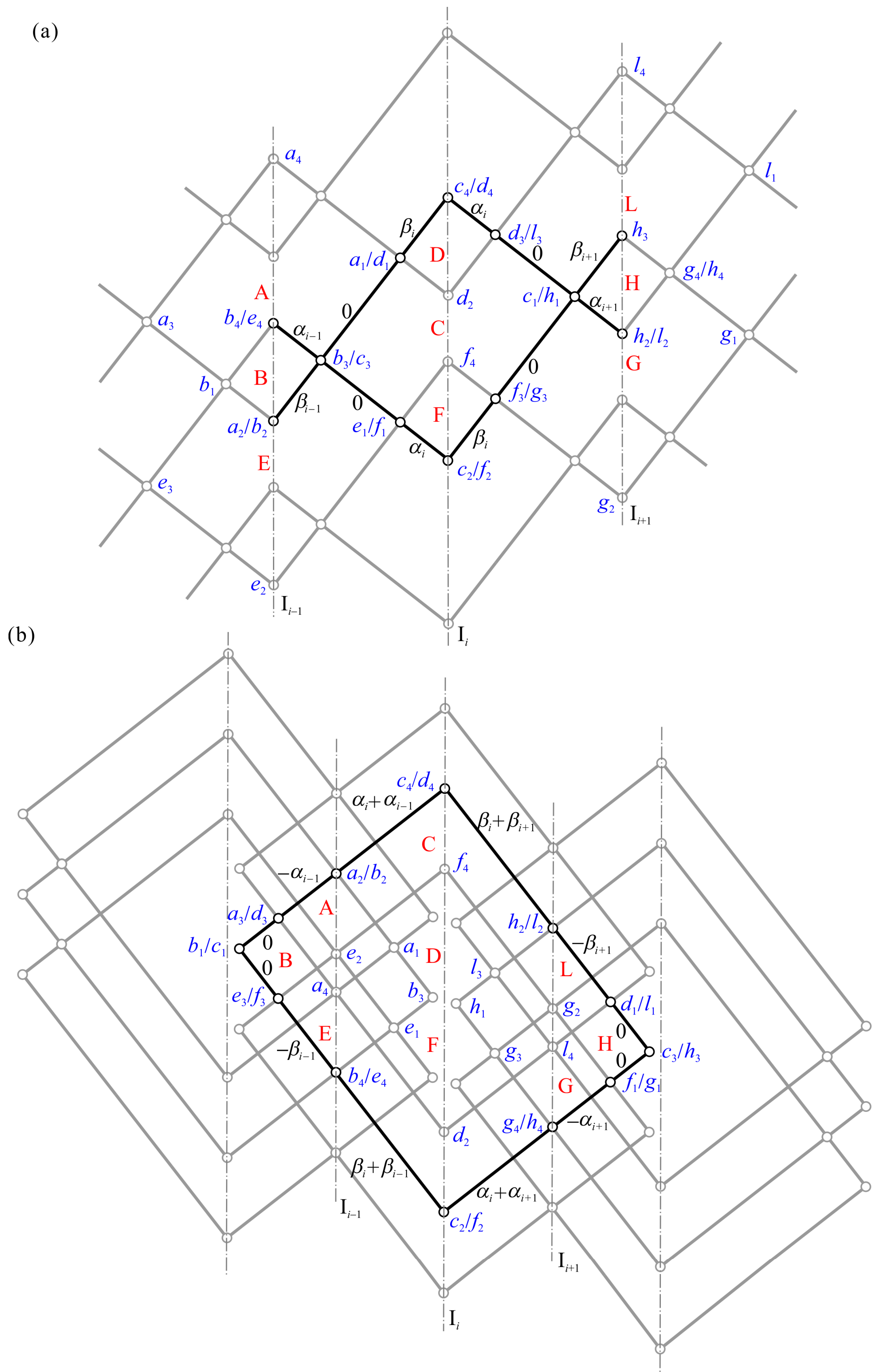

Fig. 1-9 Four cases of mobile assemblies of Bennett linkage. (a) Case 3, (b) case 4 mobile assemblies.

Twists of case 4 Bennett linkage mobile assembly with type I guidelines satisfy

$$\begin{aligned}&\alpha^{\mathrm{A}}=\alpha^{\mathrm{B}}=\alpha^{\mathrm{E}}=-\alpha_{i-1},\ \beta^{\mathrm{A}}=\beta^{\mathrm{B}}=\beta^{\mathrm{E}}=-\beta_{i-1},\\&\alpha^{\mathrm{D}}=\alpha^{\mathrm{C}}=\alpha^{\mathrm{F}}=\alpha_{i},\ \beta^{\mathrm{D}}=\beta^{\mathrm{C}}=\beta^{\mathrm{F}}=\beta_{i},\\&\alpha^{\mathrm{L}}=\alpha^{\mathrm{H}}=\alpha^{\mathrm{G}}=-\alpha_{i+1},\ \beta^{\mathrm{L}}=\beta^{\mathrm{H}}=\beta^{\mathrm{G}}=-\beta_{i+1}.\end{aligned} \tag{1-28}$$

Bennett linkages on the ith guideline should satisfy

$$\frac{\sin\alpha_i}{\sin\beta_i}=k, \tag{1-29}$$

where k is a constant throughout the whole assembly. The twists of Bennett linkages in an assembly satisfy the twist conditions along guidelines: i.e. the adjacent Bennett linkages on a type I guideline are connected with Bennett linkages and all the Bennett linkages have the same twists with α_i and β_i. The adjacent Bennett linkages on a type II guideline are connected with the scissor connection and the twists of adjacent Bennett linkages satisfy that one has α_i, β_i and its adjacent one has $-\alpha_i$, $-\beta_i$ which are same as $\pi-\alpha_i$, $\pi-\beta_i$, where subscript i represents the ith guideline. On different guidelines, the twists α_i and β_i can be different.

For the generation of high expansion to package ratio and demand of different profile for engineering, parameter analysis of the mobile assemblies of Bennett linkages are studied, such as the alternative form of Bennett linkage proposed by Chen and You [67] and it is used to construct network of alternative form of Bennett linkage, as shown in Fig. 1-10(a). Lu [82] proposed an assembly of the alternative form of Bennett linkage to approximate cylindrical surface. In addition, the mobile assembly of Bennett linkages can be designed in saddle surface [86] and polyhedrons [87]. Song [88] designed a parabolic cylindrical antenna with one-DOF. They are shown in Fig. 1-10.

A family of mobile assemblies of Myard linkages with one-DOF has been developed according to the three tiling ways by Liu and Chen [83], one of which is shown in Fig. 1-11(a). Qi and Deng [84] developed two types of large spatial assembly of Myard linkages with different twist angles, one of which is shown in Fig. 1-11(b). In addition, Chen and You [89] designed a unit with overlapping motif of Myard 6*R* linkage, where the linkage with two zero-length links is derived from combining two extended Myard linkages.

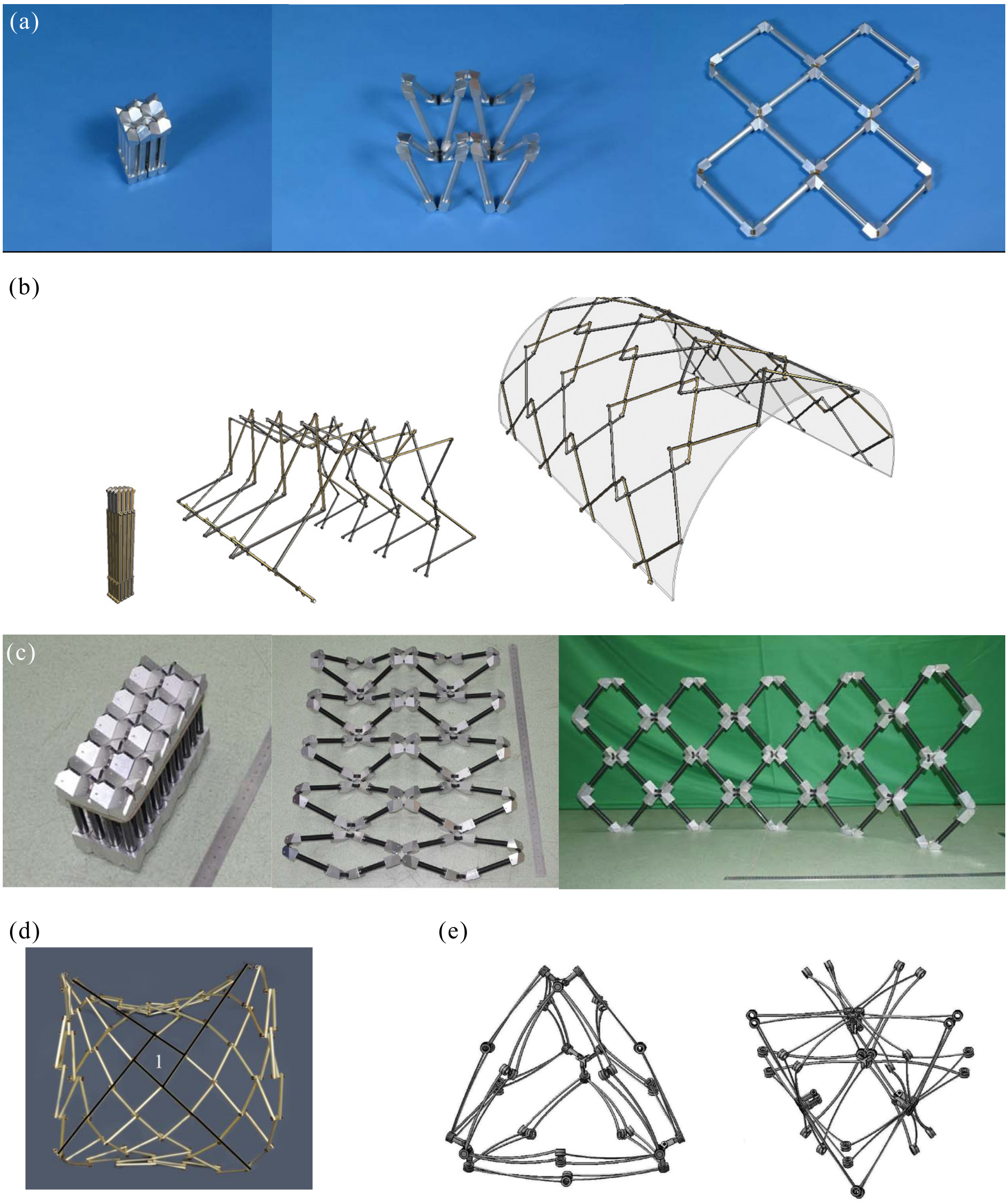

Fig. 1-10 Mobile assemblies of alternative form of Bennett linkage. (a) Assembly with flat-deployed configuration constructed by Chen and You [67]; (b) assembly approximating cylindrical surface constructed by Lu et al. [82]; (c) mobile assembly for deployable parabolic cylindrical antenna constructed by Song et al. [88]; (d) assembly approximating saddle surface constructed by Yang et al. [86]; (e) A tetrahedral linkage constructed by Kiper and Söylemez [87].

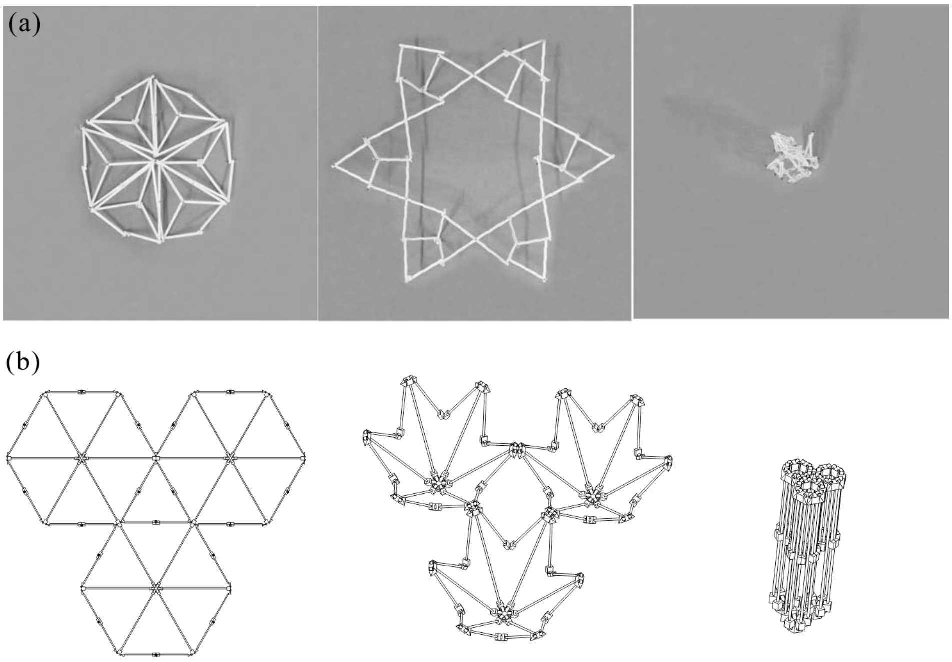

Fig. 1-11 Two mobile assemblies of Myard linkages. (a) assembly constructed by Liu and Chen [83]; (b) assembly constructed by Qi et al. [84].

For the Bricard linkages, Chen and You [67] developed a mobile assembly of threefold-symmetric Bricard linkages by connecting each pair of linkages with a scissor, which can be folded to a handle and deployed to a flat surface, as shown in Fig. 1-12(a). They also discussed the alternative form of this linkage. Based on the alternative form, Huang and Yan [85] carried out the deployed profile synthesis; Huang and Li [90] proposed a new family of one-DOF assemblies by replacing three alternate revolute joints by a class of one-DOF deployable mechanisms, which can be regarded as the unit for tessellation. Huang, Deng and Li [78] formed a deployable structure based on Bricard linkage with scissor-like connection, as shown in Fig. 1-12(b). Song and Guo [91] proposed a large deployable structure (Fig. 1-12(c)) constructed by assembling Altmann linkages and proved its mobility by screw theory. Atarer and Korkmaz [92] designed one-DOF assemblies of Altmann linkages (Fig. 1-12(d)) by assembling linkages with common links and joints or overlapping with extra R or $2R$ joints.

In summary, mobile assemblies of overconstrained spatial linkages have been constructed with different deployable configurations, e.g., flat, arch, saddle surfaces and polyhedrons. The mobile assemblies of Bennett linkages and Myard linkages have been studied thoroughly in the past. It is not easy to construct a new one. The number of mobile assemblies of Bricard linkage is limited, due to the motion complexity of both line-symmetric and plane-symmetric Bricard linkages, which makes it extremely difficult to find the compatibility condition in forming their mobile assemblies.

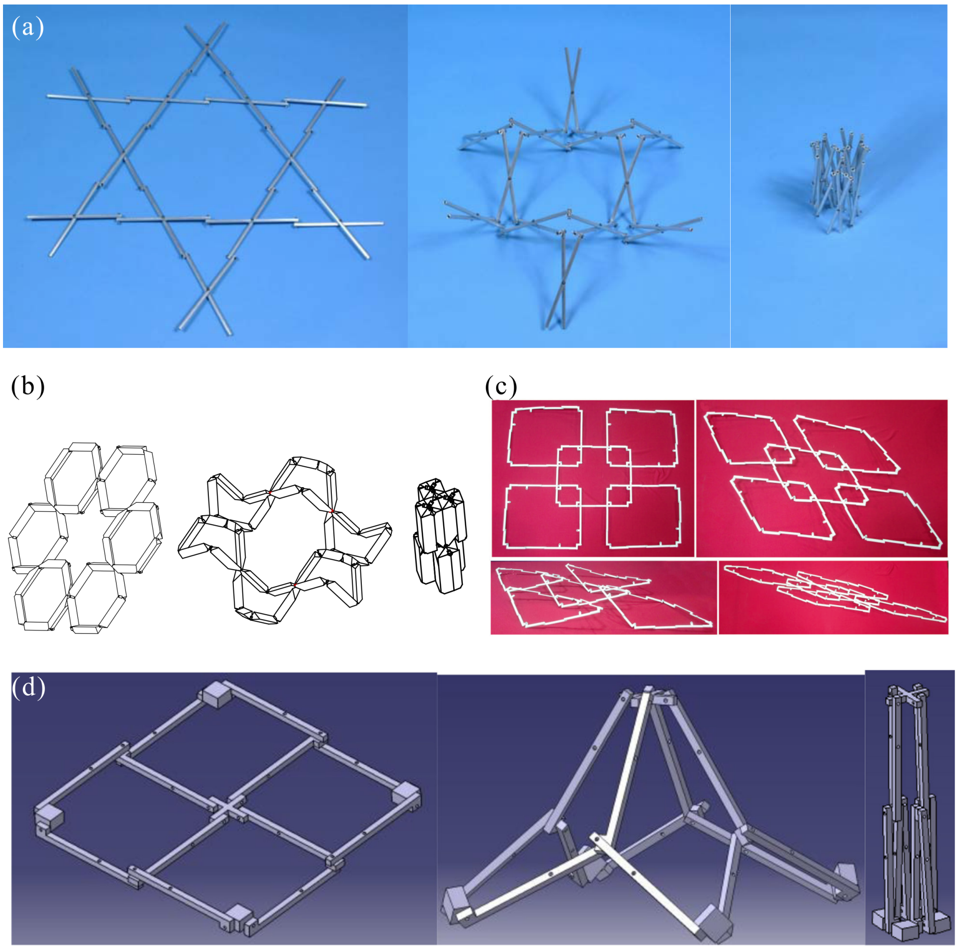

Fig. 1-12 Mobile assemblies of Bricard linkages. (a) Assembly of threefold-symmetric Bricard linkage constructed by Chen and You [67]; (b) assembly formed by scissor-like connection hexagon Bricard modules constructed by Huang, Deng and Li [78]; (c) the assembly of Altmann linkages constructed by Song et al. [91]; (d) the assembly of Altmann linkages constructed by Atarer, Korkmaz and Kiper [92].

1.2.3 Rigid Origami

Origami is a paper folding art. Each origami pattern contains creases which go into two types: mountain creases and valley creases. Several creases can meet at a single point called vertex, as shown in Fig. 1-13. There are a lot of origami patterns which can be folded to form various shapes. Most of them are derived from nature and designed by artists. Since some of them have a superior efficiency of packaging, they have been paid huge attention by the engineers and scientists. They have great potential in engineering applications in different areas, such as solar array [8, 93] in aerospace, shelters [11] in civil engineering, medicines [15, 94] and robotics [95-98]. Some applications are shown in Fig. 1-14.

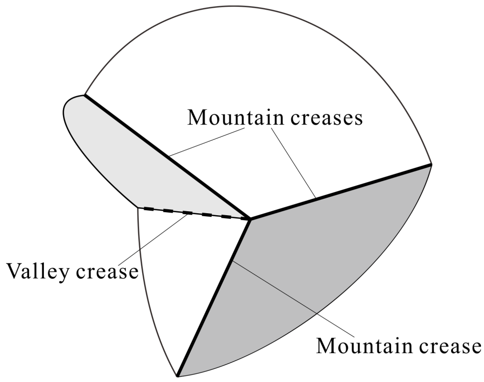

Fig. 1-13 A rigid origami vertex with four creases.

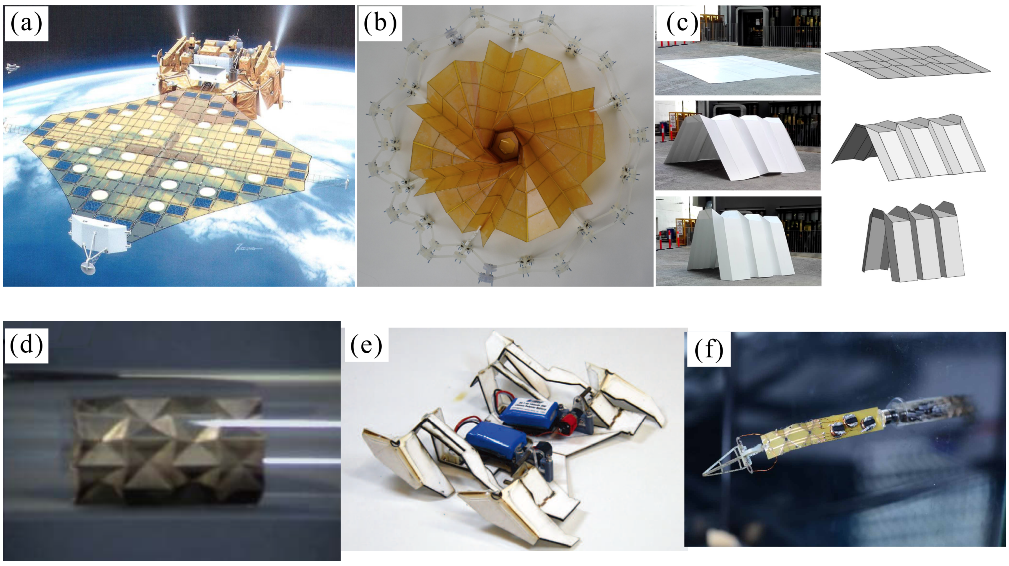

Fig. 1-14 Engineering applications of origami in different areas. (a) Solar panel designed by Miura [8]; (b) solar array constructed by Zirbel et al. [93]; (c) origami shelter proposed by Lee and Gattas [11]; (d) origami stent graft designed by Kuribayashi et al. [15]; (e) a self-folding robot designed by Felton et al. [95]; (f) a microorigami robotic arm designed by Boyvat et al. [97].

1.2.3.1 Rigid-Foldability

Rigid origami has the property of rigid-foldability which ensures the panels of one origami pattern do not stretch or bend during the folding process. It makes possible to use rigid materials for designing deployable structures. To achieve rigid-foldability, the motion of panels in an origami vertex should be compatible with the adjacent ones. Several methods have been proposed to judge rigid-foldability. Watanabe and Kawaguchi proposed the diagram method and the numerical method for judging rigid foldability [99]. Tachi generalized the geometric condition of rigid-foldable origami with quadrilateral mesh [100] and considered geometry to obtain the rigid variations [101]. Wu and You employed quaternions and dual quaternions to study rigid foldability of origami [102]. Cai et al. [103] combined the quaternion rotation sequence method and the dual quaternion method to check the rigid-foldability of cylindrical foldable origami. The compatible analysis of mechanism theory based on D-H notation is also an effective method to judge and design rigid origami pattern by regarding the origami vertex as the spherical linkage [39]. Based on the mechanism theory, new rigid origami patterns [104] and origami tubes [105, 106] were invented.

1.2.3.2 Flat-Foldability

Flat-foldability is another property for an origami to realize compact folding. Some researches have been done on this property. Mathematical study of flat origami was carried out by Hull. He gave necessary and sufficient conditions for an origami to locally fold flat [107, 108]. Lang [109] made a survey of conditions for flat-foldability of single vertex.

The first condition is the *Kawasaki-Justin Theorem*. Let v be a vertex with $2n$ creases and let α_1, $\alpha_2,\cdots\alpha_{2n}$ be the sector angles between the creases. Then v is a flat vertex if and only if

$$\alpha_1-\alpha_2+\alpha_3-\cdots-\alpha_{2n}=0. \tag{1-30}$$

For a developable origami, the sector angles around every vertex sum to 360, that is $\alpha_1+\alpha_2+\alpha_3+\cdots+\alpha_{2n}=2\pi.$ Then, a useful variation of this theory is that the vertex can fold flat if and only if

$$\alpha_1+\alpha_3+\cdots+\alpha_n=\alpha_2+\alpha_4+\cdots+\alpha_{2n}=\pi. \tag{1-31}$$

The second condition is *Big-Little-Big Angle (BLBA) Theorem*. At any vertex, the creases on either side of any sector whose angle is smaller than those of its neighbors must have opposite crease assignment.

The third condition is *Maekawa-Justin Theorem*. For any flat-foldable vertex, let *M* be the number of mountain folds at the vertex and *V* be the number of valley creases. Then

$$M-V=\pm 2. \tag{1-32}$$

1.2.3.3 The Degree of Freedom of Rigid Origami

As one rigid origami vertex can be regarded as spherical linkage, one origami can be regarded as the mechanism. According to the mobility of the vertex, rigid origami patterns with multiple vertices can be generally classified into two groups, one-DOF origami and multi-DOF origami.

One-DOF origami is generally composed of four-crease vertices. As the one-DOF origami pattern is typical and simple, patterns consisted of multiply four-crease origami vertices has been widely studied and new one-DOF origami patterns are constructed from the existing origamis or from quadrilateral meshes. The well-known one-DOF origami pattern, Miura-ori, was proposed by Miura, it has been applied to the packaging of deployable solar panels in space and the folding of maps [8, 36]. Based on the Miura-ori, five alterable characteristics are studied by Gattas, Wu and You to construct Miura-base rigid origamis, such as arc-Miura pattern and tapered Miura pattern [110]. By studying Miura-ori as a wallpaper pattern, Sareh and Guest [111, 112] constructed the family of isomorphic and non-isomorphic variations. Based on Miura-ori and Arc-Miura, graded origami structures are constructed by changing geometric parameters [113]. By introducing rigidly foldable origami gadgets, new tessellations are created [114]. One-DOF cylindrical deployable origami is constructed based on the origami vertex with four congruent parallelograms and its mirror image [115] and cellular structures are constructed from these cylinders [116]. Foldable Miura-based closed-loop origami units are designed by considering the mathematical expressions [117]. Lang and Howell started from direction angles and fold angles along the arrays and designed rigidly foldable quadrilateral meshes with one-DOF [118]. One-DOF rigid origami with multiple states which were derived from superimposing rigid-foldable crease patterns gives a new idea for designing one-DOF origami [119]. Even though a number of one-DOF origami patterns have been constructed, the overconstrained nature of a four-crease origami pattern limits its variation of sector angles. Constructing the origami pattern only with four-crease origami vertices also limits the new design of one-DOF origami.

When a vertex has more than four creases, it might have multi-DOF, such as the six-crease origami vertex and the five-crease origami vertex. These vertices can form multi-DOF origami patterns, such as diamond origami pattern (Yoshimura pattern) [109, 120], waterbomb origami pattern [121] and Resch origami patterns [122, 123]. As multi-DOF origami patterns can be deployed to variable configurations, they have been widely used in robotics [124-128]. However, sometimes one motion characteristic is needed, it is a challenge to accurately control a multi-DOF origami system, such as diamond origami pattern with multiple configurations [109] to get the desirable symmetric motion, as shown in Fig. 1-15.

For the multi-DOF vertex of origami, its DOF can be derived by $n-3$, where the n represents the number of creases meeting at the vertex [129, 130]. However, for the multi-vertex origami pattern, its DOF can be influenced by many factors [129, 130], such as the number of creases meeting at a vertex, the number of vertices, the connection relationships among the vertices, the sector angles of each vertex. They increase the difficulty of calculating the number of DOF of multi-DOF origami is difficult to calculate, which further affects the control of the origami system. Hence, reducing the number of DOF in origami is an emerge and practical research request. Several methods have been proposed to do this. Offsetting the creases at one vertex is used to maintain the symmetric folding of diamond origami pattern and to design a foldable mobile shelter system [131]. Adding extra constraints is used to reduce the DOF of an origami [132-134] to analyse the common motion of the origami pattern. Chen, Peng, and You [40] replaced multi-DOF spherical linkages at origami vertices by one-DOF spatial linkages by thick-panel origami method to reduce the DOF of diamond origami and waterbomb origami pattern to be one. Tachi reduced the DOF by transforming the multi-DOF vertex into an assembly of four-crease vertices with doubled crease lines [135]. However, there is no systematic study on how to reduce the DOF of origami patterns while maintaining their kinematic motion characteristics.

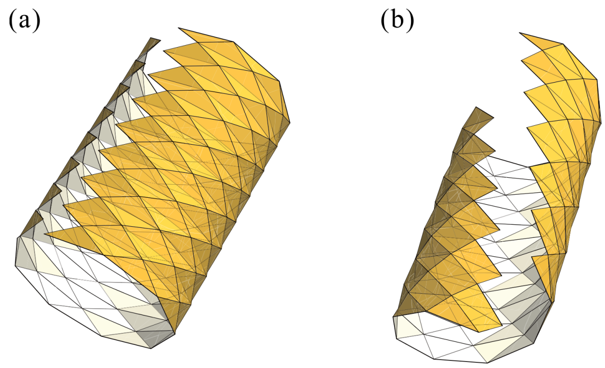

Fig. 1-15 Two configurations of diamond origami pattern proposed by Lang [107]. (a) the symmetric configuration and (b) the asymmetric configuration.

1.2.3.4 Thick-Panel Origami

One rigid origami pattern is commonly regarded as ideal zero-thickness for analysis. However, it is no longer true, when stiffness panels are used to deployable structures, especially for aerospace to endure the loads or to insulate heat. So it is necessary to consider the accommodation of thickness for panels. Various methods [136] have been proposed to accommodate thickness, as shown in Fig. 1-16. Tapered panels technique [137] is adding the thickness to the panel, then trimming intersecting material between the panels without changing the mechanical behavior of ideal zero-thickness rigid origami or losing the flat-foldability. Membrane technique [138] was proposed to accommodate thickness in origami based deployable arrays by applying a membrane backing with the widening creases with flexible material. Offset panel technique was proposed by Edmondson et al. [139] who offset the panels away from the ideal zero-thickness surface to give space to fold flat. This technique was also applied to design origami products by Morgan et al. [140]. Offset hinge technique [40, 141] was proposed by offsetting revolute joints on the surfaces of thick panels so that thickness can be accommodated. Doubled hinge technique was proposed by modifying the crease pattern that separates faces in the folded form to make room for thick panels, where the faces are accommodated thickness [142-144]. Besides, using synchronized offset rolling contact elements [145] and compliant mechanisms [146-147] can also accommodate thickness to origami panels. Recently, kirigami was used to design thick-panel patterns with flat deployed configurations [148].

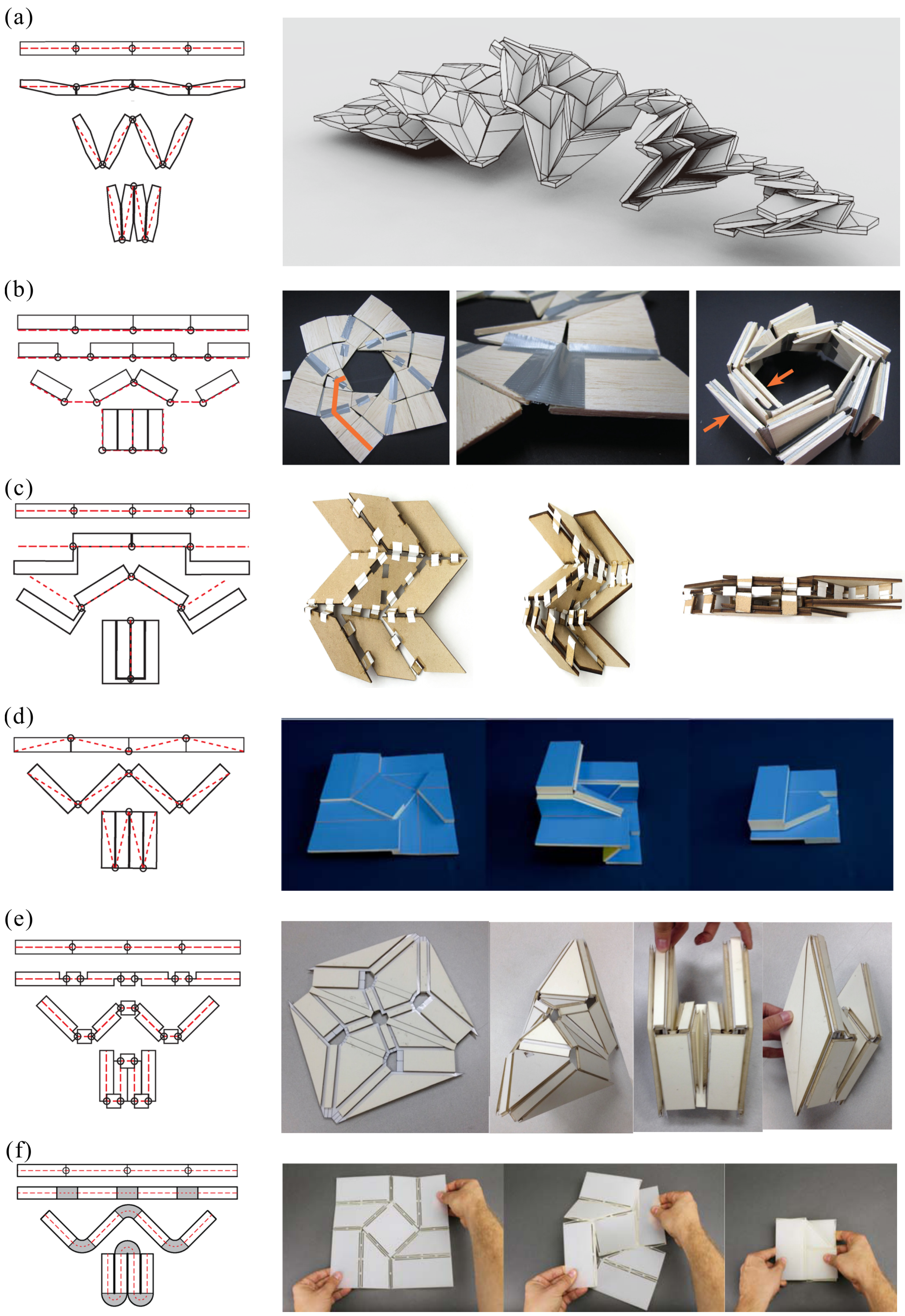

Fig. 1-16 Methods for thickness accommodation. (a) Model constructed by Tachi with tapered panels technique [137], (b) membrane technique used to a rigid-foldable six-sided flasher by Zirbel et al. [138], (c) offset panel technique used to Miura-ori by Edmondson et al. [139], (d) offset hinge technique used to a six-crease vertex by Chen, Peng and You [40], (e) doubled hinge technique used to a six-crease vertex by Ku and Demaine [143], (f) Square-twist with compliant mechanisms constructed by Pehrson et al. [146].

1.2.4 Spatial Linkages and Rigid Origami

1.2.4.1 Analysis and design of rigid origami based on spatial linkages

Motion behavior of rigid origami is an important aspect to understand and design origami patterns. It is an important property to be studied for engineering applications. Dai and Jones firstly constructed the kinematic models of carton folds by regarding creases and rigid panels as revolute joints and links, respectively [37]. Hence, the equivalent mechanisms can be used in kinematic analysis of origami with mechanism theory [149] and in the modeling of origami-type cartons with the stiffness of creases and panels [150-152]. Besides, the equivalence was also used in the analysis of pop-up paper [153] and kirigami [148]. As multi-creases meeting at a vertex in a rigid origami can be modeled as spherical linkage [38], a rigid origami pattern with a lot of vertices can be treated as a mobile assembly of spherical linkages. Hence, the rigid-foldable condition of one origami can be derived from the analysis of the compatibility condition of the equivalent mechanisms. Wang and Chen [39] modeled origami patterns as an assembly of spherical 4R linkages, and designed patterns to form the closed patterned cylinders. Liu and Chen [104] analysed the four-crease origami based on its equivalent mechanism (Fig. 1-17) and obtained four types of flat rigid origami patterns, which are planer-symmetric-type, supplementary-type, identical linkage-type and orthogonal type origami patterns, whose compatibility conditions are expressed in Eqs. (1-33) to (1-36). Feng et al. analysed the waterbomb origami pattern based on the equivalent mechanisms and found its twist motion [134].

The planar-symmetric type

$$\begin{gathered}\alpha^{\mathrm{A}}=\delta^{\mathrm{D}},\ \alpha^{\mathrm{B}}=\delta^{\mathrm{C}},\ \beta^{\mathrm{A}}=\gamma^{\mathrm{D}},\ \beta^{\mathrm{B}}=\gamma^{\mathrm{C}},\\ \gamma^{\mathrm{A}}=\beta^{\mathrm{D}},\ \gamma^{\mathrm{B}}=\beta^{\mathrm{C}},\ \delta^{\mathrm{A}}=\alpha^{\mathrm{D}},\ \delta^{\mathrm{B}}=\alpha^{\mathrm{C}},\\ |AB|=|CD|,\ |BC|+2|CD|\cos\delta^{\mathrm{D}}=|DA|;\end{gathered}\tag{1-33}$$

The supplementary-type

$$\begin{gathered}\alpha^{\mathrm{A}}+\delta^{\mathrm{D}}=\pi,\ \alpha^{\mathrm{B}}+\delta^{\mathrm{C}}=\pi,\ \beta^{\mathrm{A}}+\gamma^{\mathrm{D}}=\pi,\ \beta^{\mathrm{B}}+\gamma^{\mathrm{C}}=\pi,\\ \gamma^{\mathrm{A}}+\beta^{\mathrm{D}}=\pi,\ \gamma^{\mathrm{B}}+\beta^{\mathrm{C}}=\pi,\ \delta^{\mathrm{A}}+\alpha^{\mathrm{D}}=\pi,\ \delta^{\mathrm{B}}+\alpha^{\mathrm{C}}=\pi,\\ |AB|=|DA|\cos\alpha^{\mathrm{A}}+|BC|\cos\beta^{\mathrm{B}}+|CD|;\end{gathered}\tag{1-34}$$

The identical linkage-type

$$\begin{gathered}\alpha^{\mathrm{A}}=\alpha^{\mathrm{B}}=\alpha^{\mathrm{C}}=\alpha^{\mathrm{D}},\ \beta^{\mathrm{A}}=\beta^{\mathrm{B}}=\beta^{\mathrm{C}}=\beta^{\mathrm{D}},\\ \gamma^{\mathrm{A}}=\gamma^{\mathrm{B}}=\gamma^{\mathrm{C}}=\gamma^{\mathrm{D}},\ \delta^{\mathrm{A}}=\delta^{\mathrm{B}}=\delta^{\mathrm{C}}=\delta^{\mathrm{D}},\\ |DA|-|AB|\cos\delta^{\mathrm{A}}=|CD|\cos\delta^{\mathrm{D}}-|BC|\cos\left(\delta^{\mathrm{D}}+\gamma^{\mathrm{C}}\right);\end{gathered}\tag{1-35}$$

The orthogonal type

$$\alpha^{A}-\delta^{D}=0,\ \delta^{A}-\alpha^{D}=0,\ \beta^{B}-\gamma^{C}=0,\ \gamma^{B}-\beta^{C}=0,$$
$$\gamma^{D}+\delta^{C}=\pi,\ \beta^{A}+\alpha^{B}=\pi,\ \cos\alpha/\cos\delta=\cos\beta/\cos\gamma, \tag{1-36}$$
$$|AB|=|CD|,\ |BC|+2|CD|\cos\delta^{D}=|DA|.$$

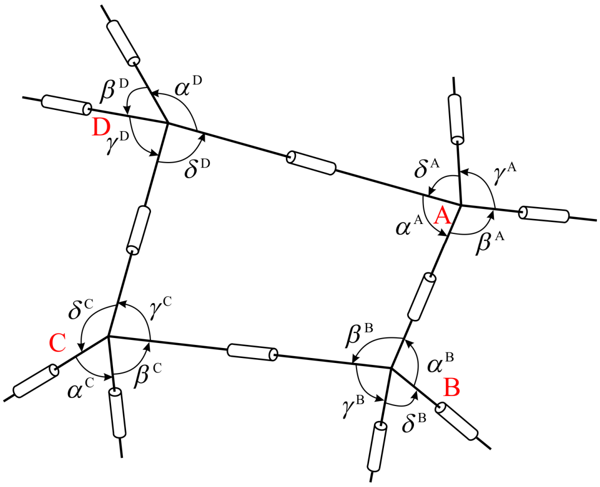

Fig. 1-17 An assembly of four spherical 4*R* linkages modeled by Liu and Chen [104].

As the thick-panel origami derived from offset hinge technique was proposed by Chen, Peng and You [40], the four-crease, five-crease and six-crease vertices in the thick-panel form are modelled as Bennett 4*R* linkage, Myard 5*R* linkage and Bricard 6*R* linkage, respectively. Their folding kinematic behaviors are kept the same as that of zero-thickness origami. Here, we focus on the thick-panel form of four-crease vertices and six-crease vertices. The relationship between the zero-thickness origami and their corresponding thick-panel origami forms are shown in Fig. 1-18 and their corresponding geometric conditions are expressed in Eqs. (1-37) and (1-38).

The geometric conditions of the four-crease origami vertex are

$$\begin{gathered}\alpha_{12}+\alpha_{34}=\alpha_{23}+\alpha_{41}=\pi,\\ \alpha_{12}^{Be}=\alpha_{12},\ \alpha_{23}^{Be}=\alpha_{23},\ \pi-\alpha_{34}^{Be}=\alpha_{34},\ \pi-\alpha_{41}^{Be}=\alpha_{41},\\ \alpha_{12}^{Be}=\alpha_{34}^{Be},\ \alpha_{23}^{Be}=\alpha_{41}^{Be},\ a_{12}^{Be}=a_{34}^{Be},\ a_{23}^{Be}=a_{41}^{Be},\\ \frac{a_{12}^{Be}}{a_{23}^{Be}}=\frac{\sin\alpha_{12}^{Be}}{\sin\alpha_{23}^{Be}}.\end{gathered}\tag{1-37}$$

The geometric conditions of the six-crease origami vertex are

$$\begin{gathered}\alpha_{12}=\alpha_{34}=\alpha_{45}=\alpha_{61},\ \alpha_{23}=\alpha_{56}=\pi-2\alpha_{12},\\ 2\pi-\alpha_{12}^{Br}=\alpha_{12},\ \alpha_{23}^{Br}=\alpha_{23},\ \alpha_{34}^{Br}=\alpha_{34},\\ 2\pi-\alpha_{45}^{Br}=\alpha_{45},\ 2\pi-\alpha_{56}^{Br}=\alpha_{56},\ \alpha_{61}^{Br}=\alpha_{61},\\ a_{12}^{Br}=a_{61}^{Br},\ a_{23}^{Br}=a_{56}^{Br},\ a_{34}^{Br}=a_{45}^{Br},\ a_{12}^{Br}+a_{23}^{Br}=a_{34}^{Br},\end{gathered}\tag{1-38}$$

in which $0 < \alpha_{12} \le \dfrac{\pi}{4}$ to ensure that the pattern has flat foldability.

For the multi-vertex thick-panel origami patterns derived from the offset hinge technique, they can be considered as mobile assemblies of spatial linkages. Compatibility conditions for the mobility and flat-foldability of waterbomb thick-panel origami pattern have been derived, whose folding process is also kinematically equivalent to the origami of zero-thickness sheets under the symmetric folding [133].

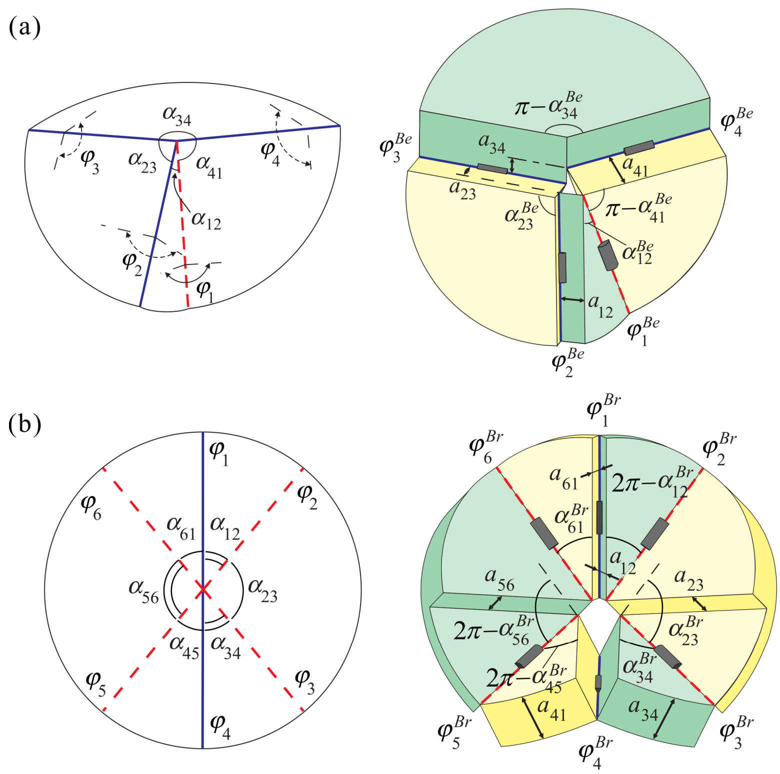

Fig. 1-18 Single vertex rigid origami patterns and the corresponding thick-panel forms. (a) Four-crease origami vertex and (b) six-crease origami vertex proposed by Chen, Peng and You [40].

1.2.4.2 Linkages inspired from rigid origami

Based on the equivalence between mechanism and rigid origami, novel mechanisms are derived, such as the metamorphic mechanisms [38]. Leal and Dai [154] designed a new class of centralixes 3-DOF parallel mechanism from origami pentagonal pattern. Wei and Dai [155] constructed a novel mechanism including one planar four-bar linkage and two spherical 4*R* linkages from an origami fold. Based on the waterbomb base, Zhang et al. designed a parallel mechanism with three-spherical kinematic chain and carried out the geometry and constraint analysis [156]. Two integrated planar-spherical overconstrained linkages were derived from origami cartons by modifying the linkages in the diagonal corners [157]. A novel overconstrained 6*R* linkage was inspired from triangle twist origami pattern by removing central triangle [42].

As the multi-vertex thick-panel origami patterns derived from the offset hinge technique [40] can be considered as mobile assemblies of the corresponding spatial linkages, a four-crease thick-panel origami pattern can inspire a mobile assembly of Bennett linkages. Six-crease thick-panel origami patterns with plane symmetry [40, 133] could lead to the discovery of mobile assemblies of plane-symmetric Bricard linkages. Therefore, the thick-panel origami can be considered as the intermediate bridge between a zero-thickness origami and a mobile assembly of spatial linkages. Study of the relationship between mobile assemblies of spatial linkages and rigid origamis with their corresponding thick-panel forms as the intermedium bridges can construct new mobile assemblies of spatial linkages. At the same time, generalisation of the compatibility conditions on the mobile assembly of spatial linkages, in turn, will improve the construct condition for the corresponding thick-panel origami patterns.

1.3 Aim and Scope

The aim of this dissertation is to study the relationship between spatial linkages and rigid origamis based on their thick-panel origami forms to design new mobile assemblies of spatial linkages. By analysing the general cases of the mobile assemblies of the linkages derived from rigid origami, new origami pattern or thick-panel form will be discovered with wide application potential. Alternatively, the origami pattern will inspire new mobile assemblies of spatial linkages with the compatibility condition from the thick-panel counterpart.

In this process, a transition technique is proposed and realizes the transition from four-crease origami pattern to mobile assemblies of Bennett linkage. By applying this technique, diamond thick-panel origami pattern is transited into new mobile assemblies of plane-symmetric Bricard linkages which are further studied for the design of variation of diamond thick-panel origami pattern. Finally, vertex-splitting is proposed to reduce the DOF of multi-DOF origami pattern and hinge-removing is derived to design thick-panel origami with flat unfolded profiles.

1.4 Outline of Dissertation

This dissertation consists of five chapters, which are outlined as follows.

Chapter 2 focus on constructing mobile assemblies of Bennett linkages from four-crease origami patterns. Firstly, a transition technique is proposed from the four-crease origami vertex to Bennett linkage. Then, the technique is applied to Miura-ori pattern, graded Miura-ori pattern, supplementary-type origami patterns and identical linkage-type origami pattern to design mobile assemblies of Bennett linkages. This chapter ends with the conclusions.

Chapter 3 devotes to the relationship between diamond thick-panel origami pattern and mobile assemblies of plane-symmetric Bricard linkages. First of all, a mobile assembly of plane-symmetric Bricard linkages is derived from the diamond thick-panel origami pattern. This is followed by the derivation of compatibility conditions for constructing the mobile assembly, which lead to the discovery of two general cases of mobile assemblies. The general assembly then inspires variations of diamond thick-panel pattern which can be with flat unfolded profiles and/or spirally folded configuration. Conclusions are drawn in the end.

Chapter 4 is to design one-DOF origami pattern from multi-DOF origami patterns and construct one-DOF thick-panel origami pattern with flat unfolded profiles by removing hinges. Based on the diamond origami vertex, the vertex-splitting technique is proposed to generate three types of unit patterns. Then it is applied to the multi-vertex diamond origami pattern and generates one-DOF basic assemblies and one-DOF origami patterns. Moreover, based on the construction of Waldron's hybrid 6*R* linkage from Bennett linkages by removing shared hinge, the transformation from the thick-panel origami pattern with two four-crease vertices to the thick-panel origami pattern with six creases is studied, which inspires the hinge-removing for the thick-panel origami pattern. After that, thick-panel origami patterns with flat unfolded profiles are derived from three thick-panel origami patterns by removing some hinges.

The main achievements of the research are summarized in Chapter 5, together with suggestions for future works, which conclude this dissertation.

Chapter 2 Mobile Assemblies of Bennett Linkages from Four-Crease Origami Patterns

2.1 Introduction

As the thick-panel origami proposed by offset hinge technique is kinematically equivalent to a mobile assembly of spatial linkages, the thick-panel origami can be considered as the intermediate bridge between a zero-thickness origami and a mobile assembly of spatial linkages. Therefore, the four distinct types of four-crease origami patterns may be used to generate the mobile assemblies of Bennett linkages by taking the corresponding thick-panel forms as the intermediate bridge.

This chapter is arranged with the following sections. Section 2.2 sets up the transition technique from single-vertex four-crease origami to Bennett linkage, which is further developed in section 2.3 for the transition from Miura-ori, graded Miura-ori and three distinct cases of supplementary-type origami patterns to different types of Bennett linkage assemblies. Especially, a new mobile assembly of Bennett linkages is derived from the identical linkage-type origami pattern in section 2.4. Conclusions are drawn in section 2.5.

2.2 Transition from Single-Vertex Four-Crease Origami to Bennett Linkages

A general single-vertex four-crease zero-thickness origami pattern is shown in Fig. 2-1(a), where z_i ($i=1, 2, 3, 4$) are axes of the four creases. Here solid lines are for mountain folds, and dashed lines are for valley folds. α, β, $\pi-\alpha$, $\pi-\beta$ are sector angles to make sure this pattern is flat-foldable. From the viewpoint of rigid origami, this four-crease pattern is rigid and kinematically can be considered as a spherical 4*R* linkage by taking the crease lines as revolute joints and the rigid panels as the rigid links, see Fig. 2-1(b), with zero link lengths. For the single-vertex four-crease thick-panel origami in Fig. 2-1(c), the sector angles are kept as same as the previous ones, but the crease lines or revolute joints z_i are moved to top or bottom surfaces of the thick panels. In order to accommodate the panel thickness in the folded configuration, two panels, P_{23} and P_{34}, with larger sector angles ($\beta>\alpha$, $\pi-\alpha>\pi-\beta$) have steps, and there are two thickness on each panel, e.g., $t_{23}\,\&\,t'_{23}$ for panel P_{23} and $t_{34}\,\&\,t'_{34}$ for panel P_{34}, where $t_{23}+t_{34}=t_{12}+t'_{23}+t'_{34}+t_{41}$. Obviously, the linkage in Fig. 2-1(c) is no longer a spherical 4*R* linkage, because the four axes do not intersect at a single point. Instead, it is a Bennett linkage as it is the only 4*R* spatial linkage. And its link lengths are related to the panel thickness,

$$a_{12}^{Be} = t_{12}, \quad a_{23}^{Be} = t_{23} - t'_{23}, \quad a_{34}^{Be} = t_{34} - t'_{34}, \; a_{41}^{Be} = t_{41}. \tag{2-1}$$

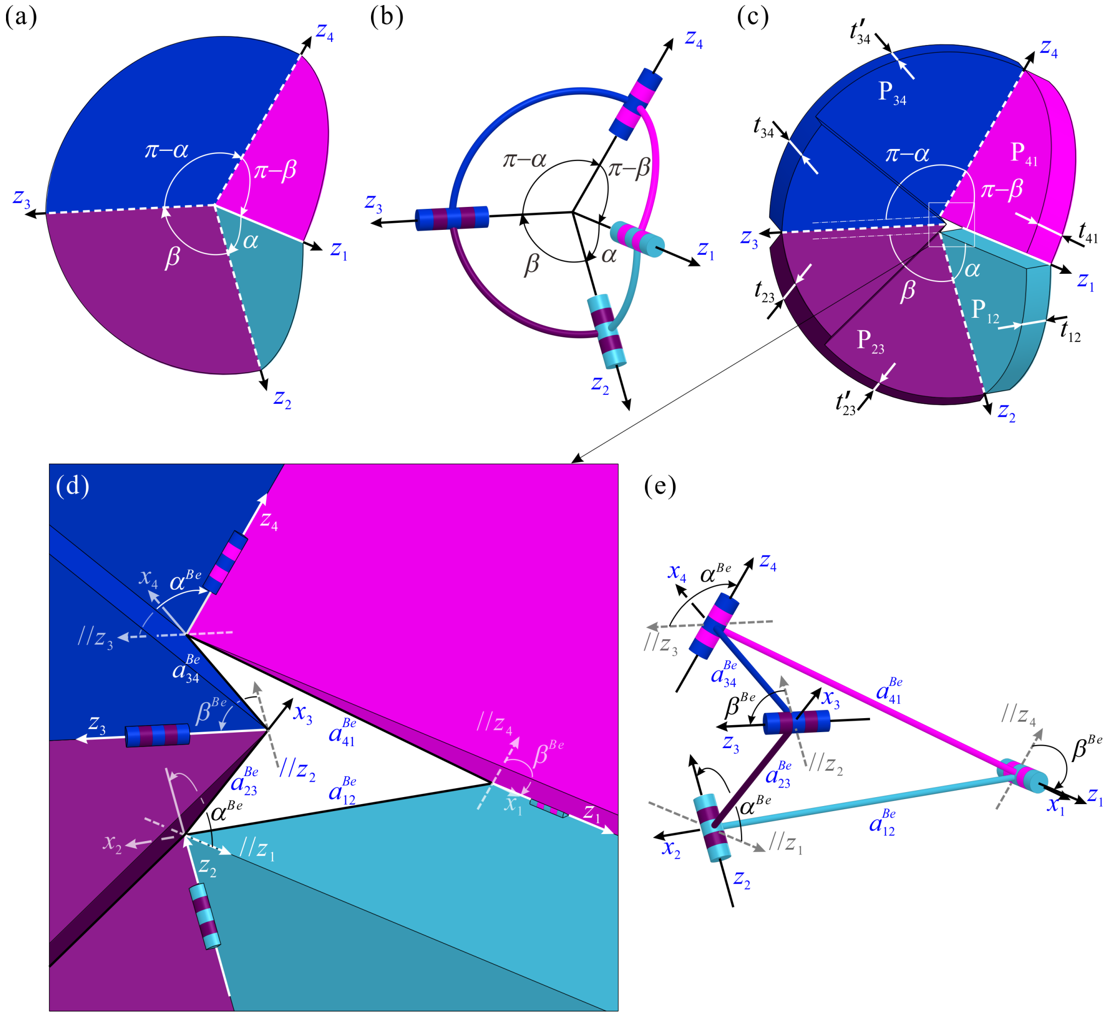

Fig. 2-1 The correspondence among the four-crease zero-thickness origami, spherical 4R linkage, four-crease thick-panel origami and Bennett linkage at one vertex. (a) A partially folded single-vertex four-crease origami with zero-thickness sheets; (b) the spherical 4R linkage; (c) the single-vertex four-crease thick-panel origami; (d) the Bennett linkage at an enlarged vertex; (e) the Bennett linkage in the traditional link form.

Due to the overconstrained condition of Bennett linkage, $a_{12}^{Be} = a_{34}^{Be} = a^{Be}$, $a_{23}^{Be} = a_{41}^{Be} = b^{Be}$ must be satisfied, i.e., $t_{12} = t_{34} - t'_{34}$, $t_{41} = t_{23} - t'_{23}$. Normally the spatial linkages are analysed with D-H notation and the matrix method. The D-H coordinates are set up in Fig. 2-1(d), which is the enlarged vertex of Fig. 2-1(c). To make the twists of the Bennett linkages align with this traditional set-up,

$$\alpha_{12}^{Be} = \alpha_{34}^{Be} = \alpha^{Be}, \quad \alpha_{23}^{Be} = \alpha_{41}^{Be} = \beta^{Be}, \quad \frac{\sin\alpha^{Be}}{a^{Be}} = \frac{\sin\beta^{Be}}{b^{Be}}. \tag{2-2}$$

We have to rearrange the directions of the revolute axes z_i by keeping z_1, z_3,

z_4 the same as the setup in the spherical 4R linkage, pointing away from the vertex, and reversing z_2 pointing to the vertex. And axes x_i are set up accordingly, thus the twists of the Bennett linkage are

$$\alpha_{12}^{Be} = \alpha_{34}^{Be} = \alpha^{Be} = \pi - \alpha \,,\ \ \alpha_{23}^{Be} = \alpha_{41}^{Be} = \beta^{Be} = \pi - \beta \,. \tag{2-3}$$

By replacing the thick panels with the straight links connecting the adjacent revolute joints in the shortest distance, a Bennett linkage in traditional link form is represented in Fig. 2-1(e).

Since the zero-thickness rigid origami (or its corresponding spherical linkage) and the thick-panel origami counterpart (or its corresponding Bennett linkage) are of the identical topology, the linkage topological graph can be applied to link them up in a later analysis of multi-vertex origami patterns and the mobile assemblies of linkages. As shown in Fig. 2-2, (b) is the topological graph of the rigid origami in Fig. 2-2(a), and Fig. 2-2(c) is the one for the Bennett linkage whose schematic diagram is given in Fig. 2-2(d). We can tell Fig. 2-2(b) and (c) is of the same topology but with different linkage twists due to the different setup of the joint axes.

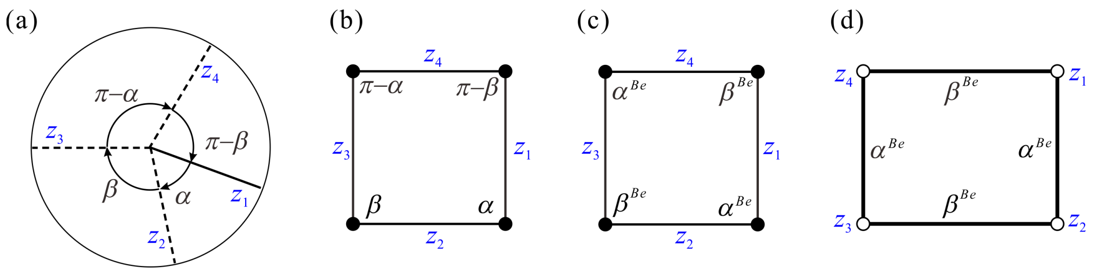

Fig. 2-2 Transition from a single-vertex four-crease origami to Bennett linkage with a topological graph. (a) Single-vertex four-crease origami; (b) the corresponding topological graph of (a) with sector angles, where each line represents a crease or revolute joint and a black solid dot represents a panel of origami; (c) topological graph with twists for the corresponding Bennett linkage; (d) schematic diagram of the Bennett linkage, where each line represents a link and a circle represents a joint without showing any direction of the joint axis, which is used to present the spatial linkage in the mobile assembly for simplicity. Here $\alpha^{Be} = \pi - \alpha$, $\beta^{Be} = \pi - \beta$.

2.3 Transition from Multi-Vertex Origami Patterns to Mobile Assemblies of Bennett Linkages

2.3.1 Mobile Assemblies Derived from a Miura-ori Pattern

Miura-ori is one of well-known traditional origami patterns formed with a number of identical parallelogram panels connected by mountain and valley creases, as shown in Fig. 2-3(a). This pattern consists of only four crease vertices with sector angles α and $\pi-\alpha$. For the vertices A, B, C, D in Fig. 2-3(a), their creases are a_i, b_i, c_i, d_i

($i=1$, 2, 3, 4). So the topological graph of this pattern in Fig. 2-3(a) is shown in Fig. 2-3(b). Because each vertex with sector angle α and $\pi-\alpha$ can be transited into the thick-panel form with equilateral Bennett linkage, the pattern with four vertices should form a mobile assembly of four such Bennett linkages. The problem is at the central panel surrounded by the creases a_2/b_2, b_3/c_3, c_4/d_4, d_1/a_1. There are four revolute joints connecting this rigid link with others to form the four Bennett linkages, A, B, C, D (Fig. 2-3(b)), so how can the joint positions on the straight link be arranged once the assembly adopts the original linkage form?

Let's take a close look at the thick-panel Miura-ori pattern in Fig. 2-4(a). Panel P is connected to panels $\mathrm{P}_{12}^{\mathrm{A}}$, $\mathrm{P}_{23}^{\mathrm{B}}$, $\mathrm{P}_{34}^{\mathrm{C}}$, $\mathrm{P}_{41}^{\mathrm{D}}$, and it appears in linkages A, B, C, D in the thick-panel form with link lengths a_{12}^{Be}, b_{23}^{Be}, c_{34}^{Be} and d_{41}^{Be}, respectively. An enlarged panel P is shown in Fig. 2-4(b). In thick-panel pattern, creases or revolute joints shared by two adjacent Bennett linkages are combined into a single one, e.g., joint a_1 of linkage A and d_1 of linkage D are combined into one. In other words, the Bennett linages attached panel P form a closed loop starting from joint a_1/d_1 to a_2/b_2 via link a_{12}^{Be}, to joint b_3/c_3 via link b_{23}^{Be}, then to joint c_4/d_4 via link c_{34}^{Be}, and finally back to joint a_1/d_1 via link d_{41}^{Be}. Hence, along the total thickness t_{P} of panel P, $a_{12}^{Be}+b_{23}^{Be}=c_{34}^{Be}+d_{41}^{Be}=t_{\mathrm{P}}$ with b_3/c_3 on the top surface, a_1/d_1 on the bottom surface, and a_2/b_2, c_4/d_4 on the medium surfaces. To maintain the physical size t_p of panel P in the central area, $a_{12}^{Be}<d_{41}^{Be}$ and $c_{34}^{Be}<b_{23}^{Be}$ or $a_{12}^{Be}=d_{41}^{Be}$ and $c_{34}^{Be}=b_{23}^{Be}$ or $a_{12}^{Be}>d_{41}^{Be}$ and $c_{34}^{Be}>b_{23}^{Be}$ can be chosen.

When $a_{12}^{Be}<d_{41}^{Be}$ and $c_{34}^{Be}<b_{23}^{Be}$, the order of joints is b_3/c_3, c_4/d_4, a_2/b_2, a_1/d_1 along the thickness direction of panel P from top to bottom, as shown in Fig. 2-4(b). The same order applies to the straight link form, as shown in Fig. 2-4(c). It should be noted that each shared revolute joint in Fig. 2-4(c) has two axis directions; however, a revolute joint has to have only one axis direction for further confirmation of the angles in one link of the mobile assembly. Hence, to maintain the relationships about twists and sector angles in Eqs. (2-2) and (2-3), all joint axes in linkages A and C are kept, while all joint axes in linkages B and D are reversed; then we can obtain the mobile assembly shown in Fig. 2-4(d). Its schematic diagram is shown in Fig. 2-3(c), where twists can be obtained by Eqs. (2-2) and (2-3) using their corresponding sector angles in Fig. 2-3(b) and some angles are from the difference in twists, e.g. the angle between a_4 and d_2 in Fig. 2-3(c) is obtained from twists of linkages A and D as $\alpha_{12}^{\mathrm{D}}-\alpha_{41}^{\mathrm{A}}=\alpha-\alpha=0$.

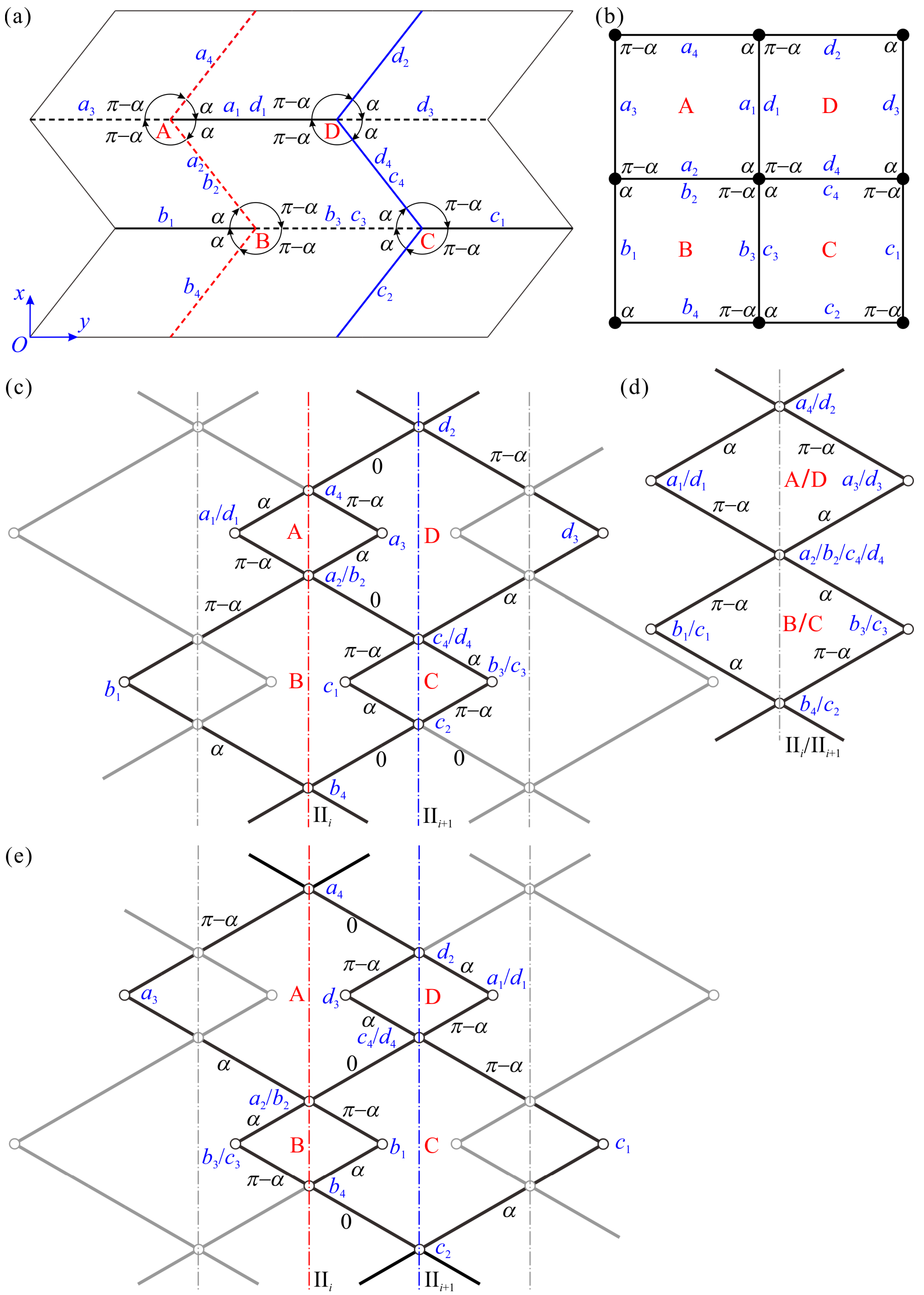

Fig. 2-3 Transition from a Miura-ori pattern to Bennett mobile assemblies. (a) Crease pattern with four vertices; (b) topological graph of a Miura-ori pattern; (c) the schematic diagrams of the corresponding mobile assembly with $a_{12}^{Be} < d_{41}^{Be}$ and $c_{34}^{Be} < b_{23}^{Be}$; (d) the assembly with $a_{12}^{Be} = d_{41}^{Be}$ and $c_{34}^{Be} = b_{23}^{Be}$; (e) the assembly with $a_{12}^{Be} > d_{41}^{Be}$ and $c_{34}^{Be} > b_{23}^{Be}$. Here each rhombus represents a Bennett linkage, gray circles and gray lines show the tessellation of the mobile assembly, dashed-dot lines represent the guidelines and II_i is the ith type II guideline.

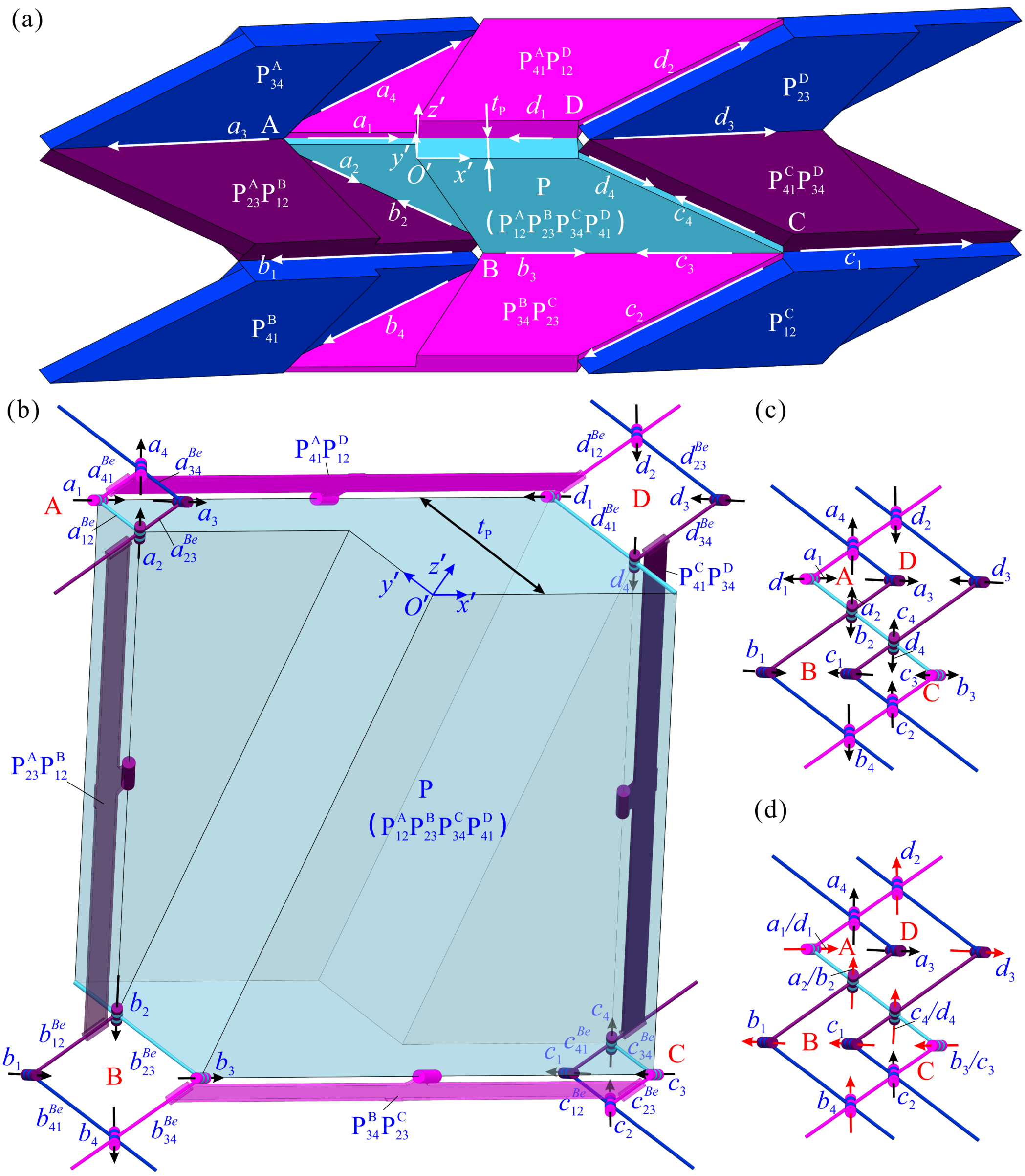

Fig. 2-4 Miura-ori thick-panel pattern and its mobile assembly. (a) Miura-ori thick-panel pattern with four vertices; (b) the enlarged panel P with four attached Bennett linkages; (c) the mobile assembly of Bennett linkages with original joint axes; (d) the mobile assembly with reversed joint axes of Bennett linkages B and D.

The case with $a_{12}^{Be} = d_{41}^{Be}$ and $c_{34}^{Be} = b_{23}^{Be}$ is an assembly of Bennett linkages (Fig. 2-3(d)), with order of joints b_3/c_3, $a_2/b_2/c_4/d_4$, a_1/d_1 along the thickness direction of panel P. Owing to linkages A and D, B and C coincide, this assembly cannot be tessellated along the horizontal direction, which is a special case of assembly in Fig. 2-3(c) consisted of all Bennett linkages with the same link lengths. The case with $a_{12}^{Be} > d_{41}^{Be}$ and $c_{34}^{Be} > b_{23}^{Be}$ is that linkages A and C become the bigger ones and linkages B and D become the smaller ones with the order of joints b_3/c_3, a_2/b_2, c_4/d_4, a_1/d_1 along the thickness direction of panel P, as shown in Fig. 2-3(e), which is of the same type as that in Fig. 2-3(c).

As the twists of the mobile assembly in Fig. 2-3(c) satisfy the type II guidelines, the Miura-ori thick-panel origami corresponds to a special case of the case 2 mobile assembly consisting of equilateral Bennett linkages. The prototypes of Miura-ori zero-thickness form, thick-panel form and the corresponding mobile assembly are shown in Fig. 2-5.

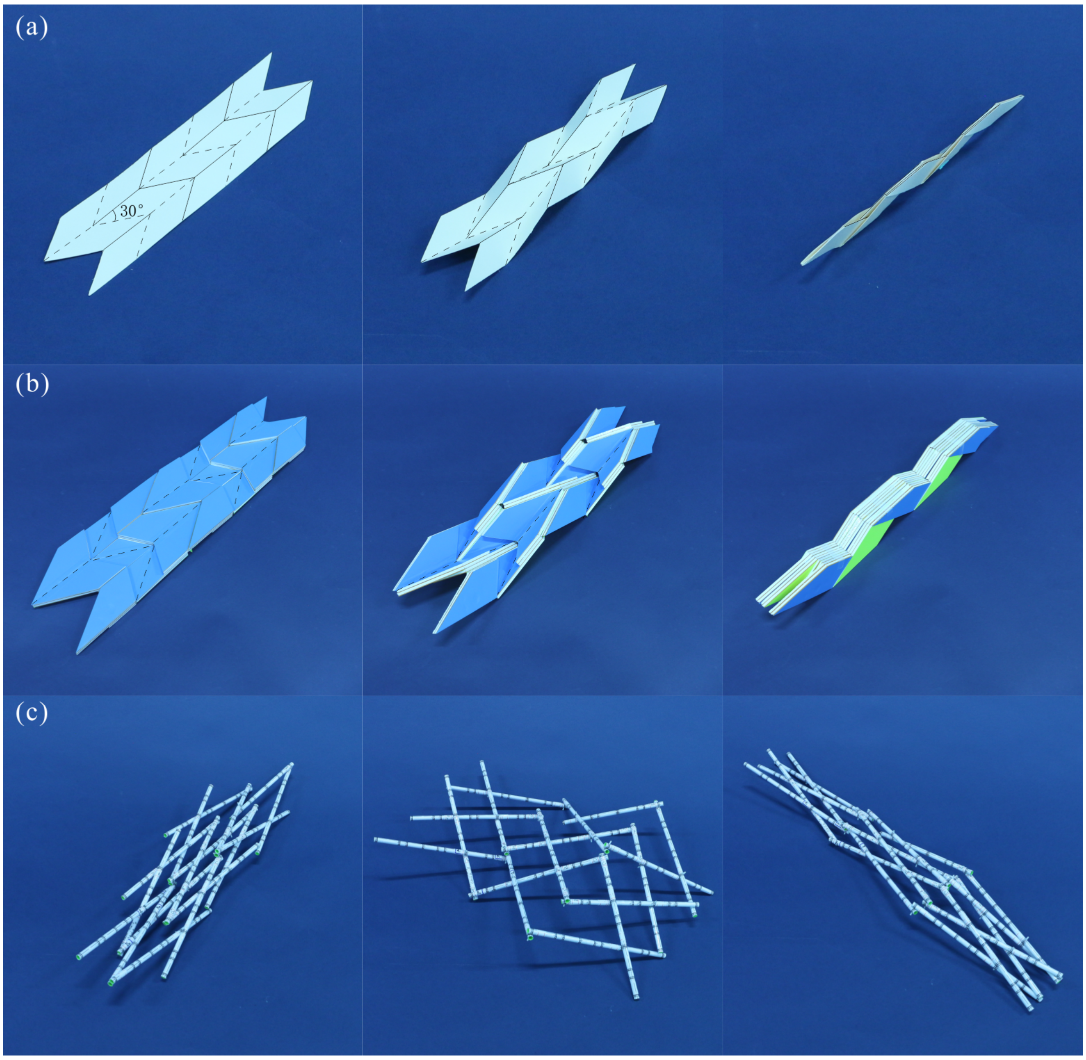

Fig. 2-5 Deployment sequences of prototypes. (a) Miura-ori pattern, (b) Miura-ori thick-panel pattern and (c) Bennett linkage mobile assembly with $\alpha = 30°$.

For the general case 2 assembly of Bennett linkages, the twists on the different guidelines can be different, as shown in Fig. 2-6(c), in which the twists on guideline II_i are α and $\pi-\alpha$ and those on guideline II_{i+1} are β and $\pi-\beta$. So correspondingly in the Miura-ori, along the different columns of vertices, the sector angles should also be different, as shown in Fig. 2-6(a) and (b), which is called *the graded Miura-ori* and their prototypes are shown in Fig. 2-7.

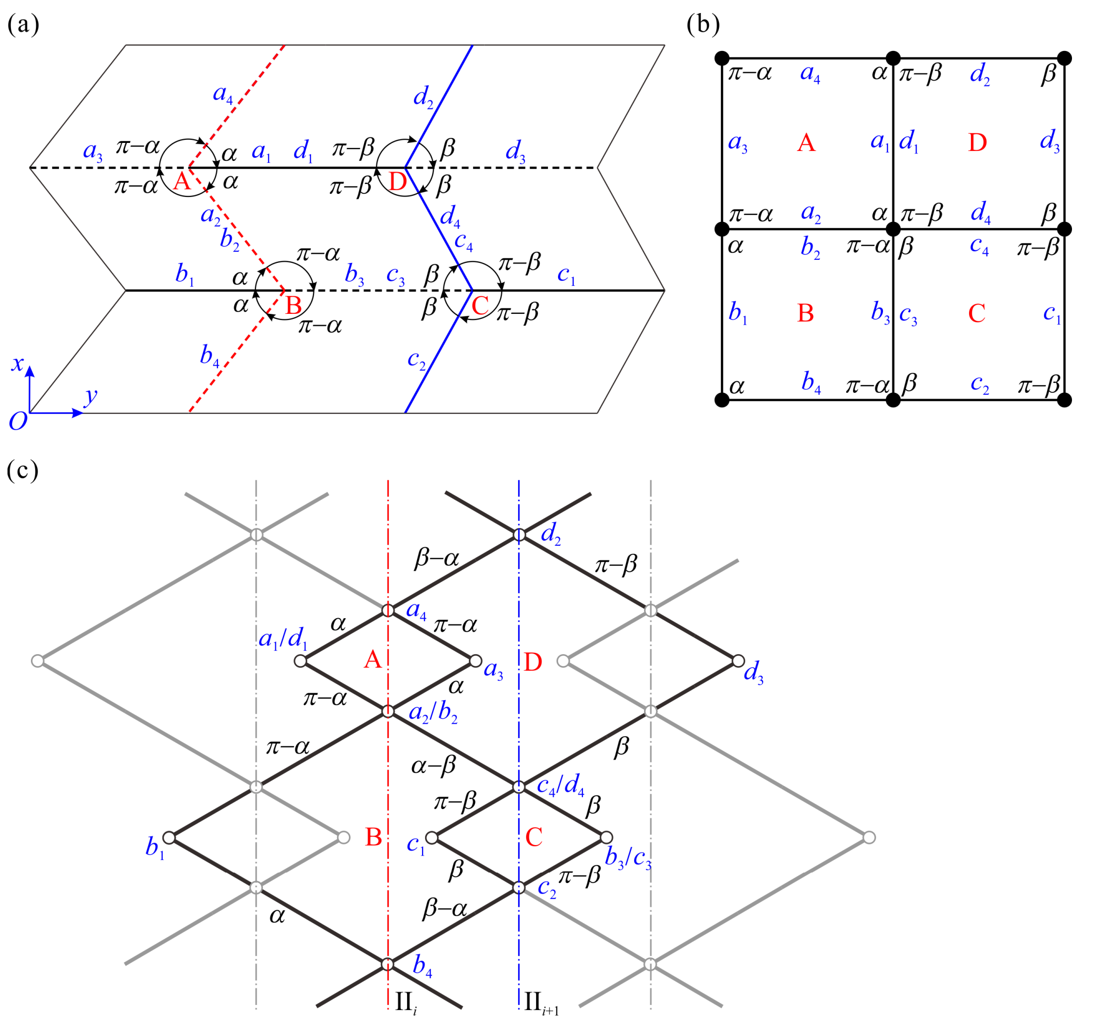

Fig. 2-6 Transition of graded Miura-ori pattern. (a) Crease pattern with four vertices of graded Miura-ori pattern; (b) topological graph of graded Miura-ori pattern; (c) the schematic diagram of corresponding mobile assembly of Bennett linkages.

2.3.2 Mobile Assemblies Derived from Supplementary-Type Origami Patterns

As Miura-ori and graded Miura-ori patterns are special cases of supplementary type origami patterns, mobile assembly consisting of general Bennett linkages can be derived from supplementary type origami patterns where the sector angles are shown schematically in Fig. 2-8(a). Three different mountain-valley crease assignments of supplementary type origami patterns with four vertices, named MVI, MVII, MVIII, are shown in Fig. 2-8(b) to (d). They are of identical topology to that shown in Fig. 2-8(e). Yet, different mountain-valley crease assignments cause the corresponding Bennett linkage assemblies to be different. With the analysed method introduced in section 2.3.1, we have found that MVI corresponds to the case 2 assembly in Fig. 2-8(f) similar as Miura-ori, while MVII and MVIII refer to the case 3 assembly and case 4 assembly respectively; see Fig. 2-8(g) and (h). It should be pointed out that some patterns could consist of different MVI, MVII, MVIII vertices, which will mean the corresponding Bennett linkage assembly is a mixture of cases 1-4 [80]. For example, the isomorphic symmetric descendant and non-isomorphic symmetric descendant of the Miura-ori are form with MVI and MVIII vertices, which was called a flat-foldable $pgg_{6,2}$ pattern and a flat-foldable $pmg^{+}_{6,2}$ pattern in [111, 112].

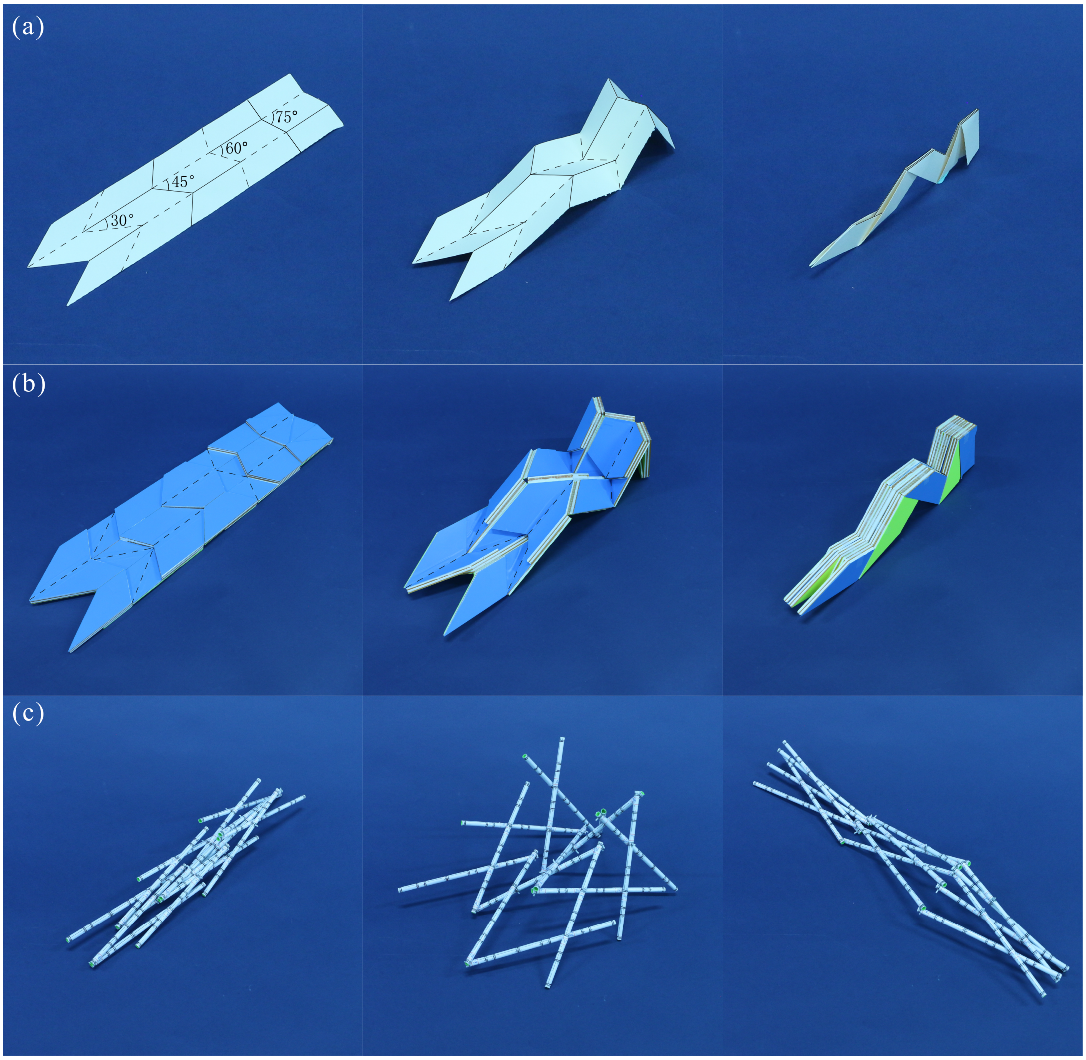

Fig. 2-7 Deployment sequences of the prototypes. (a) Graded Miura-ori pattern, (b) graded Miura-ori thick-panel pattern and (c) its corresponding mobile assembly with sector angles in each column being $30°$, $45°$, $60°$ and $75°$.

Moreover, the twists of Bennett linkages in different guidelines have no extra constraints when derived from the sector angles of origami patterns, i.e., the extra condition in [80], $\sin\alpha_i / \sin\beta_i = k$ is unnecessary, which widens the condition for constructing the assemblies of Bennett linkages. As the result, the guidelines cannot always be kept parallel to each other during the motion.

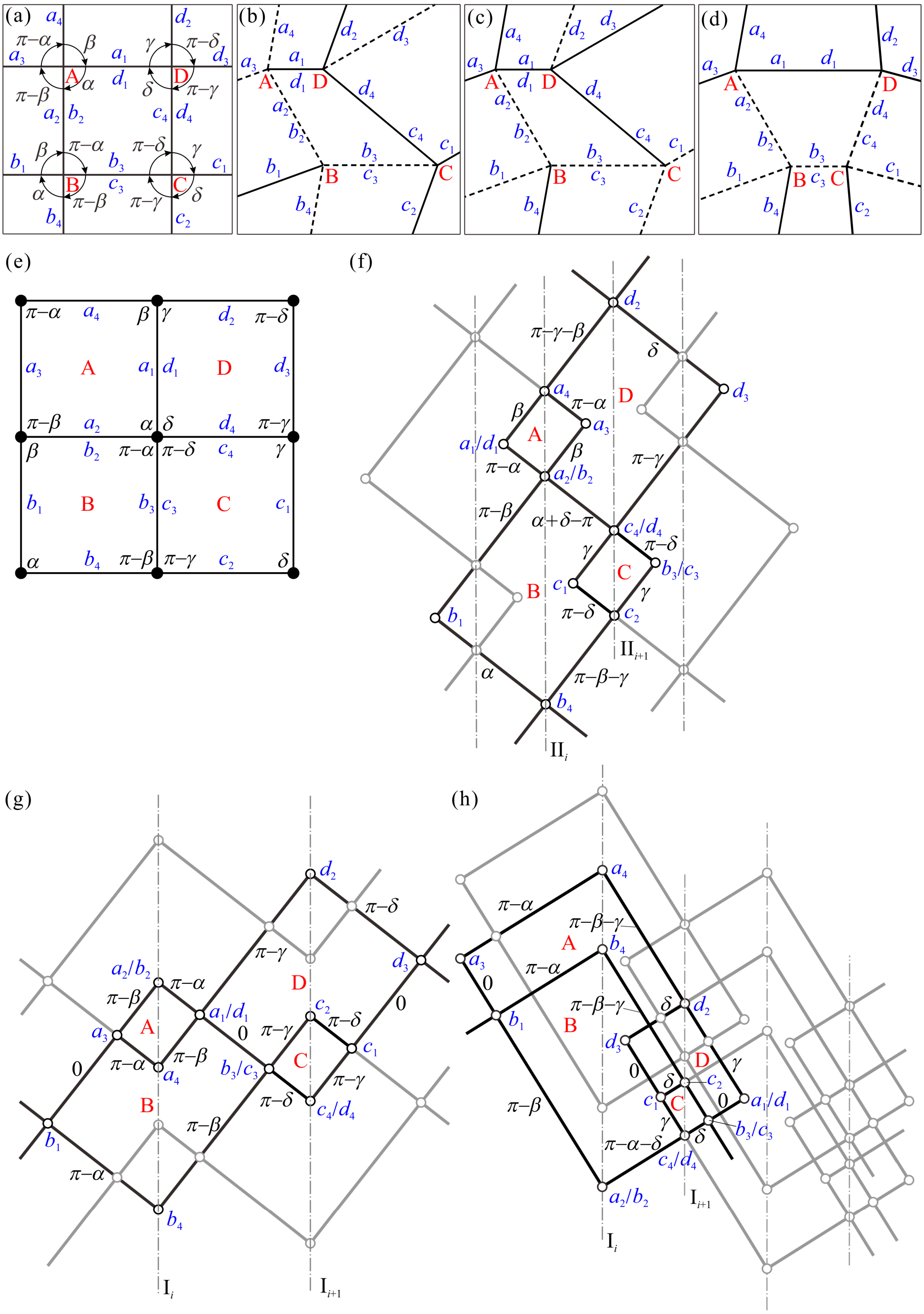

Fig. 2-8 Three mountain-valley crease assignments of supplementary type origami patterns. (a) Sector angle relationships and three cases, (b) MVI, (c) MVII, (d) MVIII, of supplementary type origami patterns with four vertices according to mountain-valley crease assignments; (e) the topological graph; (f)-(h) the schematic diagrams of mobile assemblies corresponding to (b) MVI, (c) MVII, (d) MVIII. I_i and II_i are the *i*th type I and type II guidelines, respectively.

2.4 The New Mobile Assembly of Bennett Linkages Derived from the Identical Linkage-Type Origami Pattern

An identical linkage-type origami pattern is a special four-crease origami pattern consisting of identical convex quadrilateral panels with the sector angles noted in Fig. 2-9(a). With the analysed method introduced in section 2.3.1, its topological graph and its corresponding mobile assembly of Bennett linkages are shown in Fig. 2-9(b) and (c). The Bennett mobile assembly is new as its twists satisfy the condition

$$\alpha^{\mathrm{A/C}} = \beta^{\mathrm{B/D}} = \alpha, \ \ \beta^{\mathrm{A/C}} = \alpha^{\mathrm{B/D}} = \beta. \tag{2-4}$$

Here, α and β are the same for any Bennett linkage throughout the whole assembly, which apparently does not fit any twist condition along the guidelines in cases 1-4 of [80]. Hence, we can tell it is a new assembly.

To confirm its kinematic mobility, we carry out an analysis for its compatible conditions with nine Bennett linkages from A to L (Fig. 2-9(d)), whose twists are α^{K}, β^{K} and the corresponding link lengths are a^{K}, b^{K}. Set $\alpha^{\mathrm{K}} = \alpha_{12}^{\mathrm{K}} = \alpha_{34}^{\mathrm{K}}$ and $\beta^{\mathrm{K}} = \alpha_{23}^{\mathrm{K}} = \alpha_{41}^{\mathrm{K}}$ for linkages B, D, F, H, while $\beta^{\mathrm{K}} = \alpha_{12}^{\mathrm{K}} = \alpha_{34}^{\mathrm{K}}$ and $\alpha^{\mathrm{K}} = \alpha_{23}^{\mathrm{K}} = \alpha_{41}^{\mathrm{K}}$ for A, C, E, G, L. Considering the links in red in Fig. 2-9(d), there are

$$\begin{gathered} \beta^{\mathrm{B}} + \beta^{\mathrm{A}} = \beta^{\mathrm{D}} + \beta^{\mathrm{C}}, \ \ \alpha^{\mathrm{E}} + \alpha^{\mathrm{B}} = \alpha^{\mathrm{C}} + \alpha^{\mathrm{F}}, \\ \beta^{\mathrm{F}} + \beta^{\mathrm{C}} = \beta^{\mathrm{H}} + \beta^{\mathrm{G}}, \ \ \alpha^{\mathrm{C}} + \alpha^{\mathrm{D}} = \alpha^{\mathrm{H}} + \alpha^{\mathrm{L}}, \end{gathered} \tag{2-5}$$

$$\begin{gathered} b^{\mathrm{B}} + b^{\mathrm{A}} = b^{\mathrm{D}} + b^{\mathrm{C}}, \ \ a^{\mathrm{E}} + a^{\mathrm{B}} = a^{\mathrm{C}} + a^{\mathrm{F}}, \\ b^{\mathrm{F}} + b^{\mathrm{C}} = b^{\mathrm{H}} + b^{\mathrm{G}}, \ \ a^{\mathrm{C}} + a^{\mathrm{D}} = a^{\mathrm{H}} + a^{\mathrm{L}}. \end{gathered} \tag{2-6}$$

We define σ, τ, ρ and ν as revolute variables in Fig. 2-9(d); for linkage A, the kinematic equation is

$$\tan\frac{\pi-\tau}{2}\tan\frac{\pi-\nu}{2} = \frac{\sin\frac{1}{2}\left(\alpha^{\mathrm{A}}+\beta^{\mathrm{A}}\right)}{\sin\frac{1}{2}\left(\alpha^{\mathrm{A}}-\beta^{\mathrm{A}}\right)}. \tag{2-7}$$

Similarly, for linkages B, C, D, we have

$$\tan\frac{\pi-\sigma}{2}\tan\frac{\pi-\tau}{2} = \frac{\sin\frac{1}{2}\left(\alpha^{\mathrm{B}}+\beta^{\mathrm{B}}\right)}{\sin\frac{1}{2}\left(\alpha^{\mathrm{B}}-\beta^{\mathrm{B}}\right)}, \tag{2-8}$$

$$\tan\frac{\pi-\sigma}{2}\tan\frac{\pi-\rho}{2} = \frac{\sin\frac{1}{2}\left(\alpha^{\mathrm{C}}+\beta^{\mathrm{C}}\right)}{\sin\frac{1}{2}\left(\alpha^{\mathrm{C}}-\beta^{\mathrm{C}}\right)}, \tag{2-9}$$

$$\tan\frac{\pi-\rho}{2}\tan\frac{\pi-\nu}{2}=\frac{\sin\frac{1}{2}\left(\alpha^{\mathrm{D}}+\beta^{\mathrm{D}}\right)}{\sin\frac{1}{2}\left(\alpha^{\mathrm{D}}-\beta^{\mathrm{D}}\right)}. \tag{2-10}$$

Combining Eqs. (2-7) to (2-10) gives

$$\frac{\sin\frac{1}{2}\left(\alpha^{\mathrm{A}}+\beta^{\mathrm{A}}\right)}{\sin\frac{1}{2}\left(\alpha^{\mathrm{A}}-\beta^{\mathrm{A}}\right)}\frac{\sin\frac{1}{2}\left(\alpha^{\mathrm{C}}+\beta^{\mathrm{C}}\right)}{\sin\frac{1}{2}\left(\alpha^{\mathrm{C}}-\beta^{\mathrm{C}}\right)}=\frac{\sin\frac{1}{2}\left(\alpha^{\mathrm{B}}+\beta^{\mathrm{B}}\right)}{\sin\frac{1}{2}\left(\alpha^{\mathrm{B}}-\beta^{\mathrm{B}}\right)}\frac{\sin\frac{1}{2}\left(\alpha^{\mathrm{D}}+\beta^{\mathrm{D}}\right)}{\sin\frac{1}{2}\left(\alpha^{\mathrm{D}}-\beta^{\mathrm{D}}\right)}. \tag{2-11}$$

Many solutions may exist in this nonlinear equation. By observation, three solutions can be easily obtained, which are

$$\begin{aligned}&\alpha^{\mathrm{A}}=\alpha^{\mathrm{D}},\ \beta^{\mathrm{A}}=\beta^{\mathrm{D}},\ \alpha^{\mathrm{B}}=\alpha^{\mathrm{C}},\ \beta^{\mathrm{B}}=\beta^{\mathrm{C}},\\&\alpha^{\mathrm{A}}=\beta^{\mathrm{B}}=\alpha^{\mathrm{C}}=\beta^{\mathrm{D}},\ \beta^{\mathrm{A}}=\alpha^{\mathrm{B}}=\beta^{\mathrm{C}}=\alpha^{\mathrm{D}},\\&\alpha^{\mathrm{A}}=-\alpha^{\mathrm{B}},\ \beta^{\mathrm{A}}=-\beta^{\mathrm{B}},\ \alpha^{\mathrm{C}}=-\alpha^{\mathrm{D}},\ \beta^{\mathrm{C}}=-\beta^{\mathrm{D}}.\end{aligned} \tag{2-12}$$

Similar analysis can be applied to Bennett linkages around the other three red links in Fig. 2-9. For Bennett linkages B, C, E, F, we can conclude twists should satisfy

$$\begin{aligned}&\alpha^{\mathrm{B}}=\alpha^{\mathrm{C}},\ \beta^{\mathrm{B}}=\beta^{\mathrm{C}},\ \alpha^{\mathrm{E}}=\alpha^{\mathrm{F}},\ \beta^{\mathrm{E}}=\beta^{\mathrm{F}},\\&\alpha^{\mathrm{B}}=\beta^{\mathrm{C}}=\alpha^{\mathrm{E}}=\beta^{\mathrm{F}},\ \beta^{\mathrm{B}}=\alpha^{\mathrm{C}}=\beta^{\mathrm{E}}=\alpha^{\mathrm{F}},\\&\alpha^{\mathrm{B}}=-\alpha^{\mathrm{E}},\ \beta^{\mathrm{B}}=-\beta^{\mathrm{E}},\ \alpha^{\mathrm{C}}=-\alpha^{\mathrm{F}},\ \beta^{\mathrm{C}}=-\beta^{\mathrm{F}}.\end{aligned} \tag{2-13}$$

Twists of Bennett linkages C, F, G, H should satisfy

$$\begin{aligned}&\alpha^{\mathrm{C}}=\alpha^{\mathrm{H}},\ \beta^{\mathrm{C}}=\beta^{\mathrm{H}},\ \alpha^{\mathrm{F}}=\alpha^{\mathrm{G}},\ \beta^{\mathrm{F}}=\beta^{\mathrm{G}},\\&\alpha^{\mathrm{C}}=\beta^{\mathrm{F}}=\alpha^{\mathrm{G}}=\beta^{\mathrm{H}},\ \beta^{\mathrm{C}}=\alpha^{\mathrm{F}}=\beta^{\mathrm{G}}=\alpha^{\mathrm{H}},\\&\alpha^{\mathrm{C}}=-\alpha^{\mathrm{F}},\ \beta^{\mathrm{C}}=-\beta^{\mathrm{F}},\ \alpha^{\mathrm{G}}=-\alpha^{\mathrm{H}},\ \beta^{\mathrm{G}}=-\beta^{\mathrm{H}}.\end{aligned} \tag{2-14}$$

Twists of Bennett linkages C, D, H, L should satisfy

$$\begin{aligned}&\alpha^{\mathrm{C}}=\alpha^{\mathrm{H}},\ \beta^{\mathrm{C}}=\beta^{\mathrm{H}},\ \alpha^{\mathrm{D}}=\alpha^{\mathrm{L}},\ \beta^{\mathrm{D}}=\beta^{\mathrm{L}},\\&\alpha^{\mathrm{C}}=\beta^{\mathrm{D}}=\alpha^{\mathrm{H}}=\beta^{\mathrm{L}},\ \beta^{\mathrm{C}}=\alpha^{\mathrm{D}}=\beta^{\mathrm{H}}=\alpha^{\mathrm{L}},\\&\alpha^{\mathrm{C}}=-\alpha^{\mathrm{D}},\ \beta^{\mathrm{C}}=-\beta^{\mathrm{D}},\ \alpha^{\mathrm{H}}=-\alpha^{\mathrm{L}},\ \beta^{\mathrm{H}}=-\beta^{\mathrm{L}}.\end{aligned} \tag{2-15}$$

Combing Eqs. (2-12) to (2-15), three solutions can be obtained to enable the assembly in Fig. 2-9(d) to become mobile, as follows:

$$\begin{aligned}&\alpha^{\mathrm{A}}=\alpha^{\mathrm{D}}=\alpha^{\mathrm{L}}=\beta_{i-1},\ \beta^{\mathrm{A}}=\beta^{\mathrm{D}}=\beta^{\mathrm{L}}=\alpha_{i-1},\\&\alpha^{\mathrm{B}}=\alpha^{\mathrm{C}}=\alpha^{\mathrm{H}}=\beta_{i},\ \beta^{\mathrm{B}}=\beta^{\mathrm{C}}=\beta^{\mathrm{H}}=\alpha_{i},\\&\alpha^{\mathrm{E}}=\alpha^{\mathrm{F}}=\alpha^{\mathrm{G}}=\beta_{i+1},\ \beta^{\mathrm{E}}=\beta^{\mathrm{F}}=\beta^{\mathrm{G}}=\alpha_{i+1},\end{aligned} \tag{2-16}$$

$$\begin{aligned}&\alpha^{\mathrm{A}}=\beta^{\mathrm{B}}=\alpha^{\mathrm{C}}=\beta^{\mathrm{D}}=\alpha^{\mathrm{E}}=\beta^{\mathrm{F}}=\alpha^{\mathrm{G}}=\beta^{\mathrm{H}}=\alpha^{\mathrm{L}}=\alpha,\\&\beta^{\mathrm{A}}=\alpha^{\mathrm{B}}=\beta^{\mathrm{C}}=\alpha^{\mathrm{D}}=\beta^{\mathrm{E}}=\alpha^{\mathrm{F}}=\beta^{\mathrm{G}}=\alpha^{\mathrm{H}}=\beta^{\mathrm{L}}=\beta,\end{aligned} \tag{2-17}$$

$$
\begin{aligned}
&\alpha^{\mathrm{A}} = -\alpha^{\mathrm{B}} = \alpha^{\mathrm{E}} = \alpha_{i-1},\ \ \beta^{\mathrm{A}} = -\beta^{\mathrm{B}} = \beta^{\mathrm{E}} = \beta_{i-1},\\
&\alpha^{\mathrm{D}} = -\alpha^{\mathrm{C}} = \alpha^{\mathrm{F}} = -\alpha_{i},\ \ \beta^{\mathrm{D}} = -\beta^{\mathrm{C}} = \beta^{\mathrm{F}} = -\beta_{i},\\
&\alpha^{\mathrm{L}} = -\alpha^{\mathrm{H}} = \alpha^{\mathrm{G}} = \alpha_{i+1},\ \ \beta^{\mathrm{L}} = -\beta^{\mathrm{H}} = \beta^{\mathrm{G}} = \beta_{i+1}.
\end{aligned}
\tag{2-18}
$$

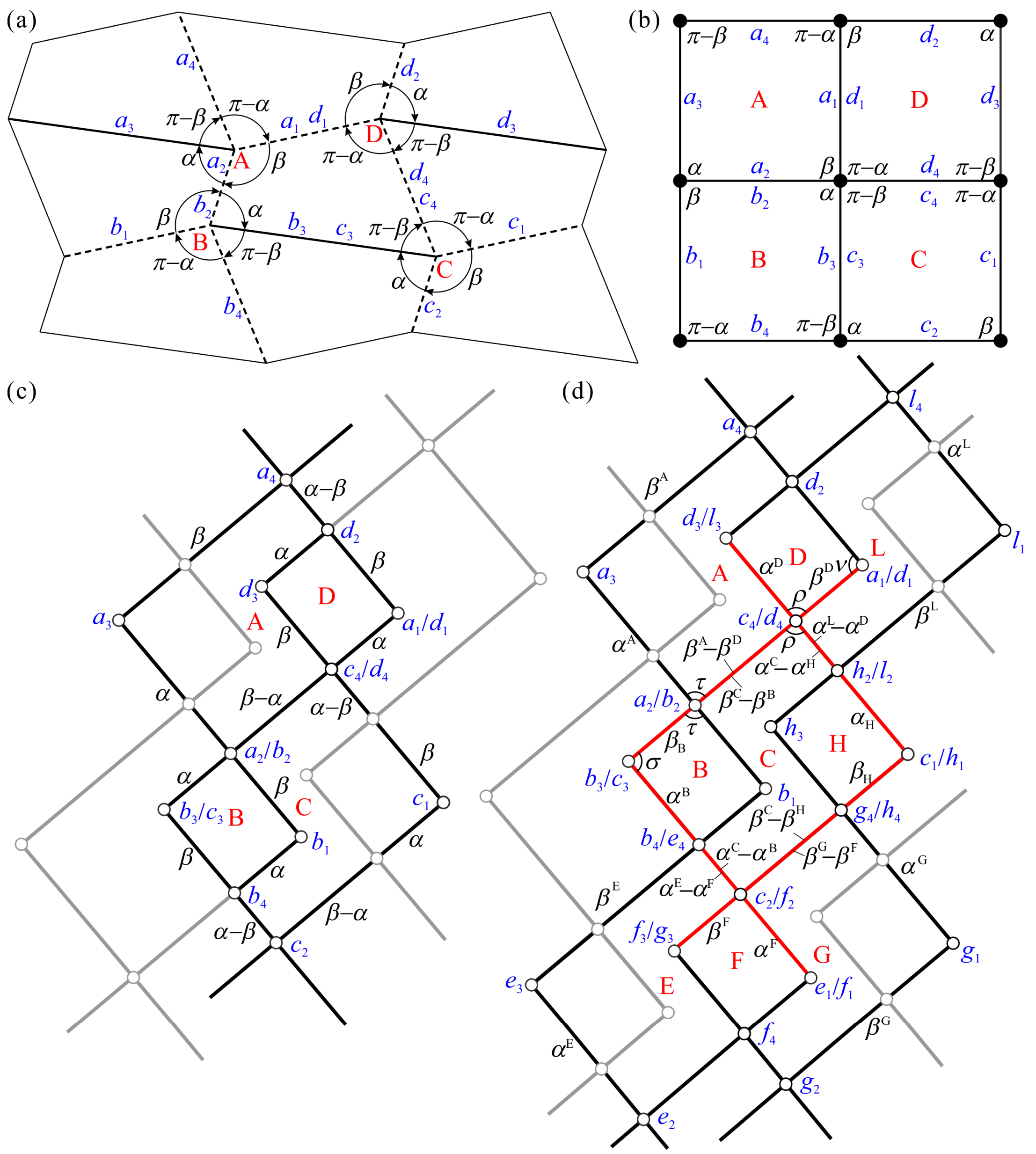

Fig. 2-9 Transition of identical linkage-type origami patterns. (a) Crease pattern with four vertices; (b) topological graph; (c) schematic diagram of the mobile assembly of Bennett linkages; (d) schematic diagram of the mobile assembly with nine linkages.

From the three solutions in Eqs. (2-16) to (2-18), we find the Eq. (2-16) corresponds to the case 3 assembly and Eq. (2-18) corresponds to the case 2 assembly. Meanwhile Eq. (2-17) corresponding to the new mobile assembly derived from the identical linkage-type origami pattern in Fig. 2-9(c). Its prototypes of zero-thickness origami pattern, thick-panel form and the corresponding mobile assembly are shown in Fig. 2-10. Here, twists in the whole assembly are identical for any Bennett linkage and its twist condition (2-17) is different from that in cases 1-4 in section 1.2.2.2. Moreover, this new assembly does not have guidelines shown as dashed-dot lines in Fig. 1-8 and Fig. 1-9.

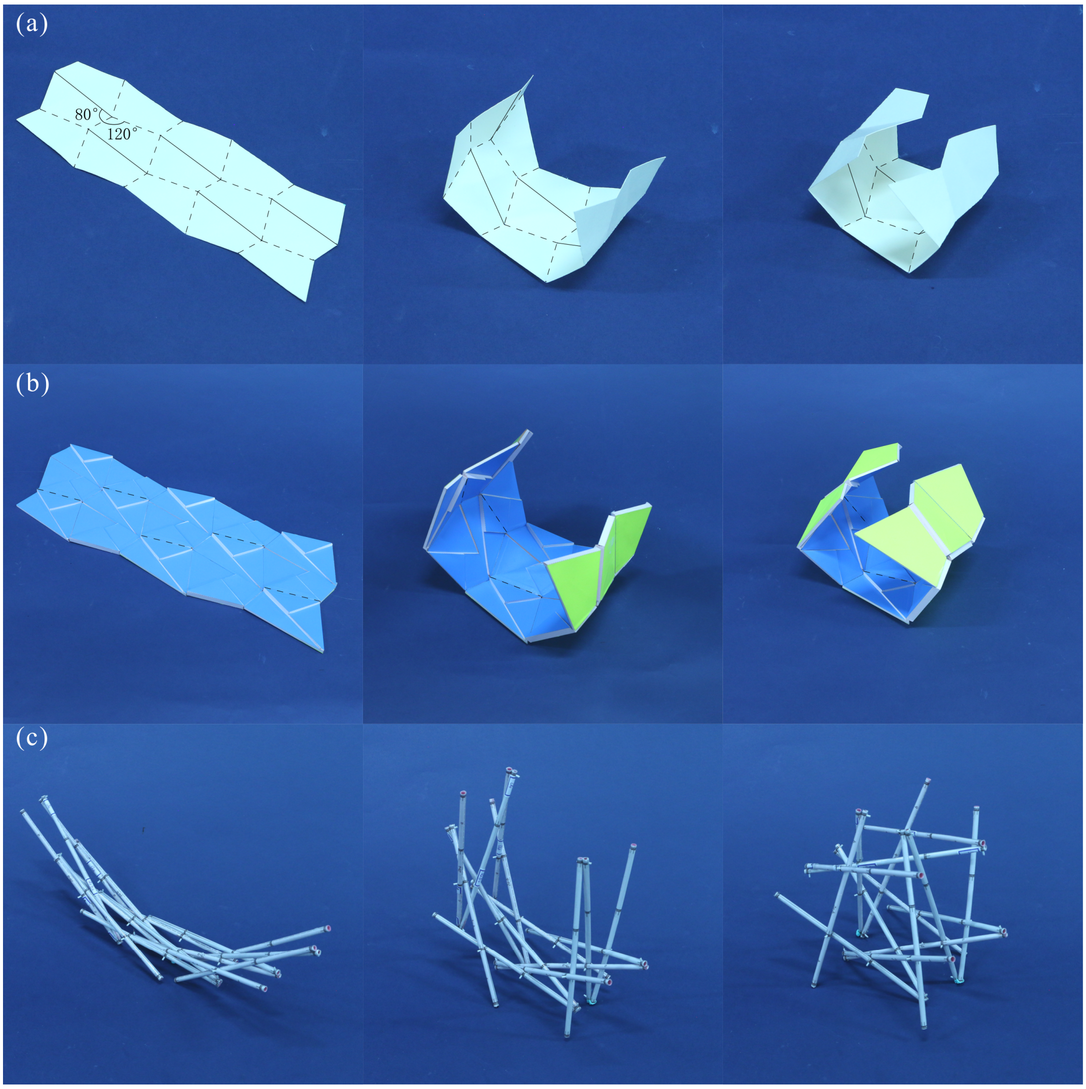

Fig. 2-10 Deployment sequences of prototypes. (a) Identical linkage-type origami pattern, (b) its thick-panel form and (c) mobile assembly of Bennett linkages with $\alpha = 80°$ and $\beta = 120°$.

2.5 Conclusions

In this chapter, we have proposed a transition technique for constructing the mobile assemblies of Bennett linkages from four-crease origami patterns with their thick-panel form as the intermediate bridge. Topological graphs are introduced to extract the connection information from the zero-thickness rigid origami patterns (or their corresponding mobile assemblies of spherical linkages) and their thick-panel forms (or the corresponding mobile assemblies of Bennett linkages). By considering the distribution orders of joints in each panel, the mobile assembly of the Bennett linkages can be obtained from the topological graph of the origami pattern. Applying the transition technique to several typical four-crease origami patterns, we found that Miura-ori and graded Miura-ori patterns lead to mobile assemblies of equilateral Bennett linkages; different mountain-valley crease assignments of the supplementary-type origami patterns correspond to case 2, case 3 and case 4 assemblies of Bennett linkages with more general construction conditions. Moreover, using the identical linkage-type origami pattern produces a new Bennett linkage mobile assembly. It should be noted that only supplementary-type origami patterns and the identical linkage-type origami pattern are discussed in this chapter, as the orthogonal type and planer-symmetric-type origami patterns for constructing tessellated thick-panel origami patterns are special cases of supplementary-type origami patterns.

Chapter 3 The Diamond Thick-Panel Origami and the Corresponding Mobile Assemblies of Bricard Linkages

3.1 Introduction

As a four-crease pattern is related to a mobile assembly of Bennett linkages, which has been studied in Chapter 2, six-crease thick-panel origami patterns with plane symmetry, such as diamond and waterbomb thick-panel origami patterns, could lead to the discovery of mobile assemblies of plane-symmetric Bricard linkages. At the same time, generalisation of the compatibility conditions on the mobile assembly of such spatial linkages, in turn, will enhance the construct condition for the corresponding thick-panel origami patterns. Therefore, in this chapter, we are studying the diamond thick-panel origami and the corresponding mobile assemblies of plane-symmetric Bricard linkages.

The layout of this chapter is listed as follows. Section 3.2 presents a kinematically equivalent assembly of plane-symmetric Bricard linkages derived from diamond thick-panel origami. In section 3.3, compatibility analysis based on diamond assembly generates two general cases of mobile assemblies. The general mobile assembly inspires the variation of diamond thick-panel pattern, leading to new patterns with flat unfolded profiles and/or spirally folded configuration, reported in section 3.4. Conclusions in section 3.5 end the chapter.

3.2 Assembly of Plane-Symmetric Bricard Linkages Derived from the Diamond Thick-Panel Origami

3.2.1 A Diamond Thick-Panel Origami Vertex and a Plane-Symmetric Bricard Linkage

A single-vertex of diamond origami pattern is shown in Fig. 3-1(a), where solid lines are mountain creases and dashed lines are valley creases. Here axes of six creases are noted by z_i (i = 1, 2,…, 6) and sector angles are marked by $\alpha_{i(i+1)}$ with the geometric condition [73]

$$\begin{aligned}&\alpha_{12}=\alpha_{61}=\alpha,\\&\alpha_{23}=\alpha_{56}=\pi-2\alpha,\\&\alpha_{34}=\alpha_{45}=\alpha,\end{aligned} \tag{3-1}$$

where $0<\alpha\le\pi/4$, to ensure flat foldability. Its thick-panel form is presented in Fig. 3-1(b) with the plane-symmetric property, which corresponds to a plane-symmetric Bricard linkage [73]. Hence, the panel thickness should satisfy

$$t_{12}=t_{61},\ t_{23}=t_{56},\ t'_{23}=t'_{56},\ t_{34}=t_{45}. \tag{3-2}$$

To achieve the compact folding without interference, the panel thickness should also satisfy

$$t_{12}+t_{23}=t'_{23}+t_{34},\ t_{56}+t_{61}=t_{45}+t'_{56}. \tag{3-3}$$

The enlarged vertex is shown in Fig. 3-1(c) with the D-H notation. And the link lengths and twists are marked along panel thickness. Next, replacing the panels with links which connect the adjacent revolute joints in the shortest distance, the corresponding plane-symmetric Bricard linkage is revealed as Fig. 3-1(d). Therefore, the thick-panel vertex in Fig. 3-1(b) and the plane-symmetric Bricard linkage in Fig. 3-1(d) are kinematically equivalent.

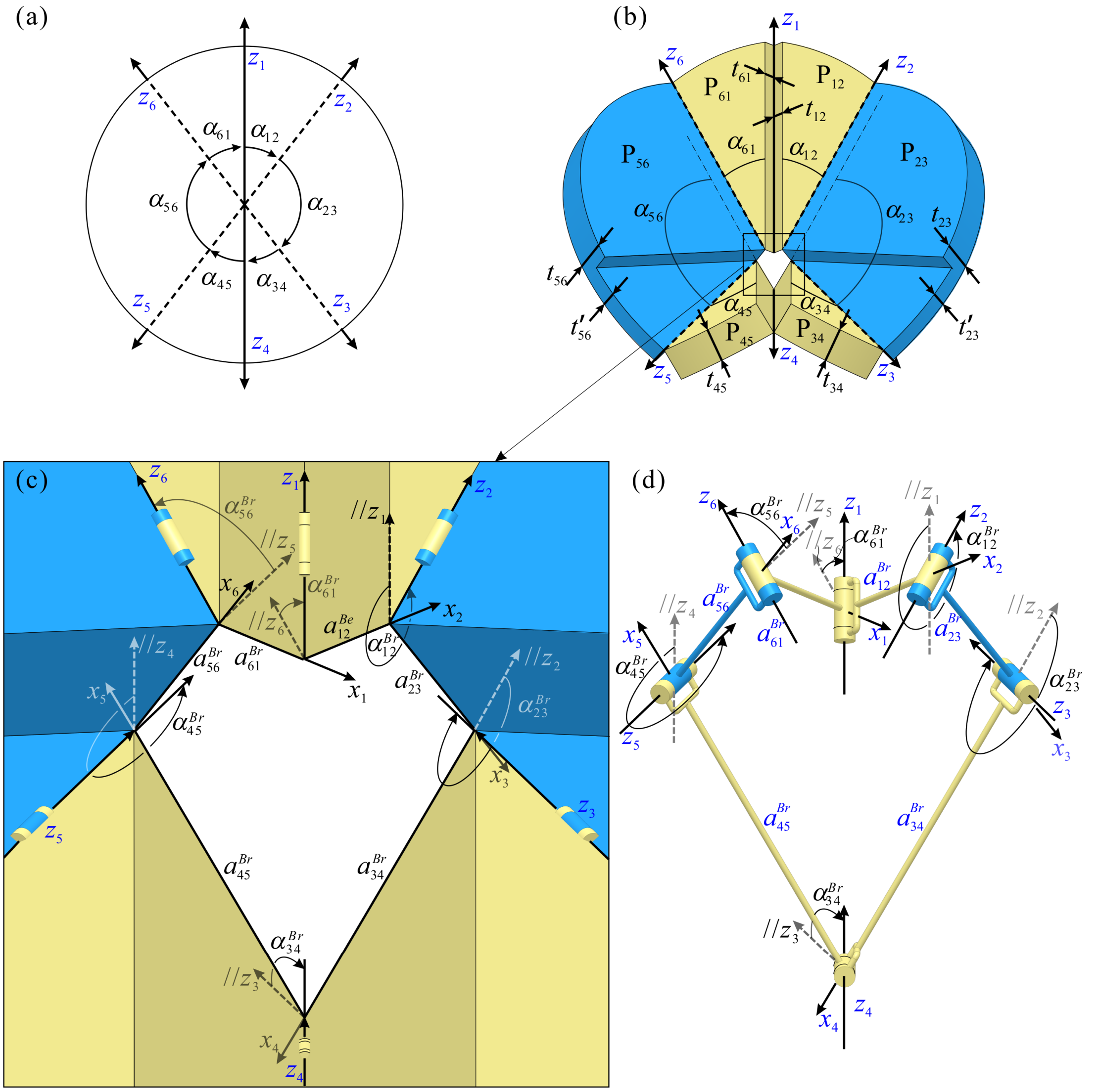

Fig. 3-1 The correspondence among the origami vertex, thick-panel origami vertex and plane-symmetric Bricard linkage. (a) The crease pattern of the diamond thick-panel origami vertex; (b) diamond thick-panel origami vertex; (c) the Bricard linkage at enlarged vertex of the thick-panel origami; (d) the plane-symmetric Bricard linkage.

In general, the geometric condition of a plane-symmetric Bricard linkage [73] is

$$\begin{aligned} &\alpha_{12}^{Br}=-\alpha_{61}^{Br}=\alpha^{Br},\ \alpha_{23}^{Br}=-\alpha_{56}^{Br}=\beta^{Br},\ \alpha_{34}^{Br}=-\alpha_{45}^{Br}=\gamma^{Br},\\ &a_{12}^{Br}=a_{61}^{Br}=u^{Br},\ a_{23}^{Br}=a_{56}^{Br}=v^{Br},\ a_{34}^{Br}=a_{45}^{Br}=w^{Br}, \end{aligned} \tag{3-4}$$

under the D-H coordinates in Fig. 3-1(d). Here, α^{Br}, β^{Br}, γ^{Br}, u^{Br}, v^{Br}, w^{Br} are taken as the geometrical parameters of the linkage. Noted in the multi-vertex pattern, if the crease axes are set pointing away from its own vertex as Fig. 3-1(a), one crease between two vertices is shared by two axes in opposite directions. To keep the axis of each joint with single direction in the later analysis of its assembly, we have to rearrange the directions of revolute axes z_i by keeping z_1, z_2, z_6 pointing away from the vertex, and reversing z_3, z_4, z_5 pointing to the vertex, as shown in Fig. 3-1(c) and (d). Meanwhile, the axes x_i can be obtained, accordingly. Then we can obtain the relationships between the twists of linkage and sector angles of origami pattern as

$$\begin{aligned} &\alpha_{12}^{Br}=-\alpha_{61}^{Br}=\alpha^{Br}=-\alpha,\\ &\alpha_{23}^{Br}=-\alpha_{56}^{Br}=\beta^{Br}=-2\alpha,\\ &\alpha_{34}^{Br}=-\alpha_{45}^{Br}=\gamma^{Br}=\alpha, \end{aligned} \tag{3-5}$$

and that between link length and panel thickness as

$$\begin{aligned} &a_{12}^{Br}=a_{61}^{Br}=u^{Br}=t_{12}=t_{61},\\ &a_{23}^{Br}=a_{56}^{Br}=v^{Br}=t_{23}-t'_{23}=t_{56}-t'_{56},\\ &a_{34}^{Br}=a_{45}^{Br}=w^{Br}=t_{34}=t_{45},\\ &u^{Br}+v^{Br}=w^{Br}. \end{aligned} \tag{3-6}$$

3.2.2 Transition from Diamond Thick-Panel Origami Pattern to a Mobile Assembly

In Fig. 3-2(a), the creases of the diamond origami pattern with four vertices A, B, C, D, are noted by a_i, b_i, c_i, d_i ($i=1$, 2,…, 6) and its sector angles are α, $\pi-2\alpha$. The corresponding thick-panel form is shown in Fig. 3-2(b). Since each thick-panel vertex corresponds to a plane-symmetric Bricard linkage, this thick-panel form of the multi-vertex pattern should be a mobile assembly of plane-symmetric Bricard linkages, which is derived next. Noted that the superscript ‘*Br*’ of the twist or the link length of Bricard linkage is omitted in the later analysis of mobile assemblies. α^{K}, β^{K}, γ^{K} and u^{K}, v^{K}, w^{K} represent twists and the corresponding link lengths of Bricard linkage K in the mobile assembly, respectively, where K can be A, B, C, D, E, F, G.

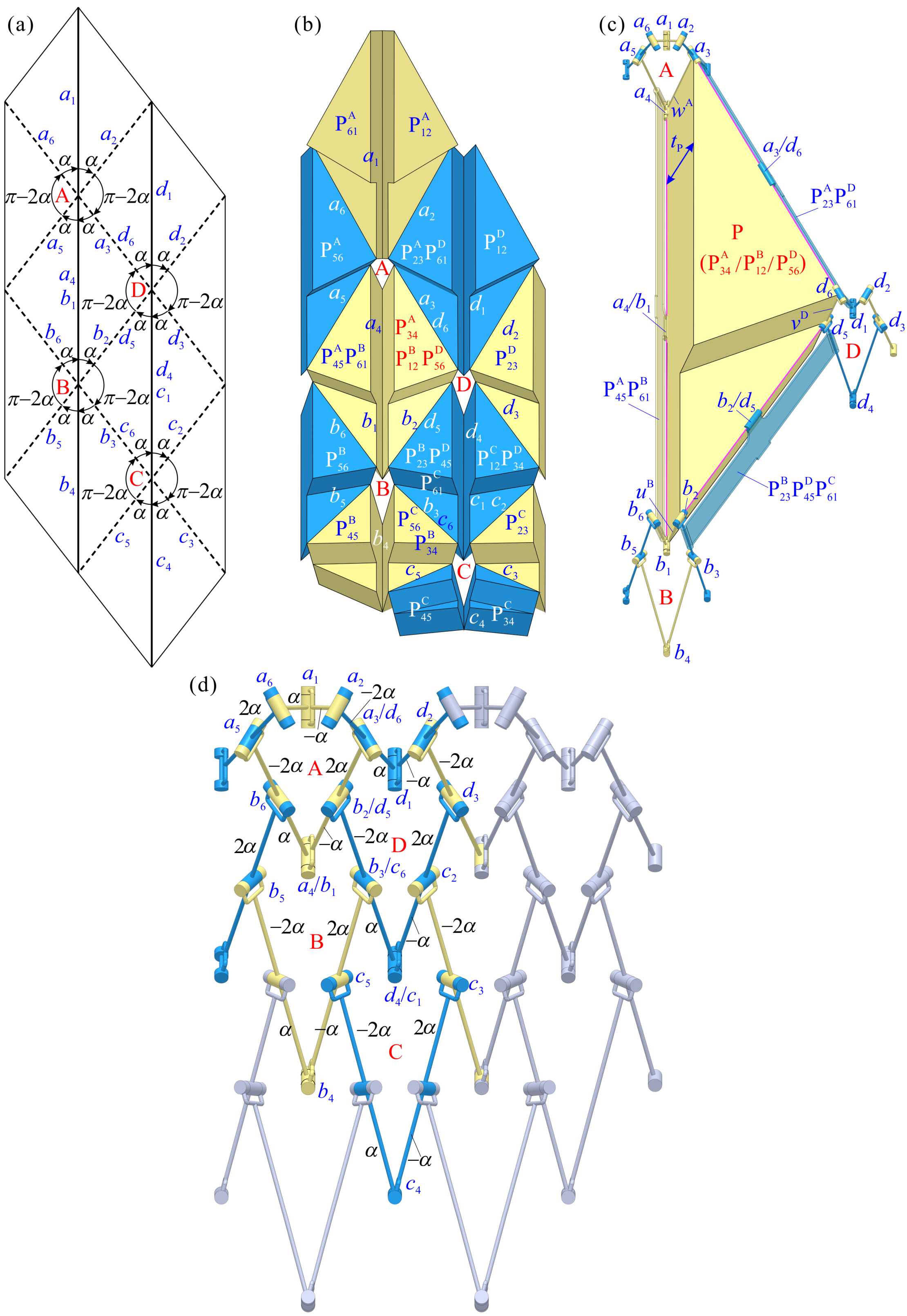

Fig. 3-2 Transition from the diamond thick-panel origami pattern to a mobile assembly of plane-symmetric Bricard linkages. (a) The crease pattern with four vertices; (b) the corresponding thick-panel form; (c) the enlarged central panel attached with three plane-symmetric Bricard linkages; (d) the mobile assembly, where gray links and joints show the tessellation.

In the thick-panel pattern (Fig. 3-2(b)), the central panel P ($\mathrm{P}_{34}^{\mathrm{A}}/\mathrm{P}_{12}^{\mathrm{B}}/\mathrm{P}_{56}^{\mathrm{D}}$) is connected to three linkages A, B, D with links a_{34}, b_{12}, d_{56}, as shown in Fig. 3-2(c). Creases or revolute joints shared by the adjacent two linkages are combined into one, i.e., the joint a_3/d_6 shared by linkages A and D, the joint b_2/d_5 shared by linkages B and D and the joint a_4/b_1 shared by linkages A and B. The links and joints are formed of a loop, i.e., from joint a_3/d_6 to a_4/b_1 via link a_{34}, to joint b_2/d_5 via link b_{12}, and then back to a_3/d_6 via link d_{56}. Hence, along thickness direction of panel P, there are three joints, joint a_4/b_1 in the bottom, joint b_2/d_5 in the middle and joint a_3/d_6 on the top. Furthermore, its total thickness t_{P} and link lengths have a relationship as

$$t_{\mathrm{P}} = w^{\mathrm{A}} = u^{\mathrm{B}} + v^{\mathrm{D}}. \tag{3-7}$$

Hence, the order of joints a_4/b_1, b_2/d_5, a_3/d_6 in panel P is obtained. Similarly, the order of joints in the panel $\mathrm{P}_{23}^{\mathrm{B}}/\mathrm{P}_{61}^{\mathrm{C}}/\mathrm{P}_{45}^{\mathrm{D}}$ can be obtained as c_1/d_4, b_3/c_6, b_2/d_5. Applying the orders of joints to the straight link forms, an assembly of plane-symmetric Bricard linkages is constructed, as shown in Fig. 3-2(d). From Eqs. (3-5) to (3-7), we can obtain the construct condition of the new mobile assembly of plane-symmetric Bricard linkages as

$$\begin{aligned}&\alpha^{\mathrm{A}} = \alpha^{\mathrm{B}} = \alpha^{\mathrm{C}} = \alpha^{\mathrm{D}} = -\alpha,\ \beta^{\mathrm{A}} = \beta^{\mathrm{B}} = \beta^{\mathrm{C}} = \beta^{\mathrm{D}} = -2\alpha,\\ &\gamma^{\mathrm{A}} = \gamma^{\mathrm{B}} = \gamma^{\mathrm{C}} = \gamma^{\mathrm{D}} = \alpha,\ u^{\mathrm{K}} + v^{\mathrm{K}} = w^{\mathrm{K}},\ u^{\mathrm{B}} + v^{\mathrm{D}} = w^{\mathrm{A}},\ u^{\mathrm{C}} + v^{\mathrm{B}} = w^{\mathrm{D}}.\end{aligned} \tag{3-8}$$

Prototypes of diamond thick-panel origami pattern and its corresponding mobile assembly which is called *diamond assembly*, are shown in Fig. 3-3.

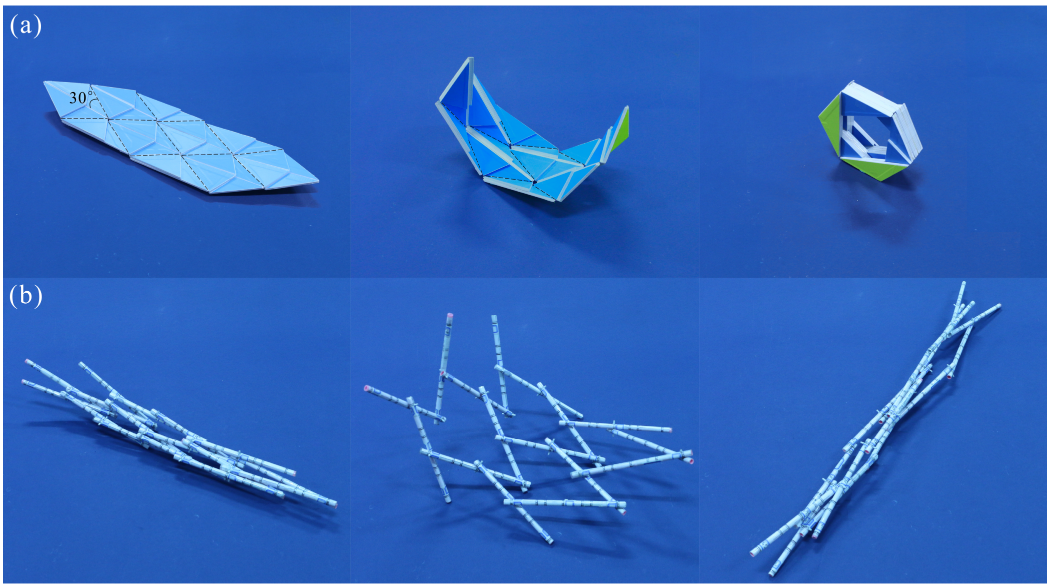

Fig. 3-3 Motion sequences of (a) a diamond thick-panel origami pattern and (b) its corresponding mobile assembly of plane-symmetric Bricard linkages with $\alpha = 30°$.

3.3 The Analysis of Compatibility Condition for the Mobile Assembly

The above mobile assembly consists of identical plane-symmetric Bricard linkages with $\alpha^{\mathrm{K}} = \beta^{\mathrm{K}} / 2 = -\gamma^{\mathrm{K}} = -\alpha$, which is a very special case of plane-symmetric Bricard linkage, compared to the general geometric condition in Eq. (3-4). To obtain more general condition for constructing the mobile assembly with plane-symmetric Bricard linkage, the compatibility condition with seven general plane-symmetric Bricard linkages A to G in Fig. 3-4 will be studied here.

The closure equations of the general plane-symmetric Bricard linkage [73] are

$$\begin{aligned}&\frac{\mathrm{s}\gamma(\mathrm{c}\theta_2\mathrm{s}\theta_3+\mathrm{c}\beta\mathrm{s}\theta_2\mathrm{c}\theta_3)+\mathrm{s}\beta\mathrm{c}\gamma\mathrm{s}\theta_2}{(\mathrm{c}\alpha\mathrm{s}\gamma\mathrm{s}\theta_2\mathrm{s}\theta_3-\mathrm{c}\alpha\mathrm{c}\beta\mathrm{s}\gamma\mathrm{c}\theta_2\mathrm{c}\theta_3+\mathrm{s}\alpha\mathrm{s}\beta\mathrm{s}\gamma\mathrm{c}\theta_3-\mathrm{c}\alpha\mathrm{s}\beta\mathrm{c}\gamma\mathrm{c}\theta_2-\mathrm{s}\alpha\mathrm{c}\beta\mathrm{c}\gamma)}\\&=\frac{w(\mathrm{c}\theta_2\mathrm{c}\theta_3-\mathrm{c}\beta\mathrm{s}\theta_2\mathrm{s}\theta_3)+v\mathrm{c}\theta_2+u}{(w(\mathrm{c}\alpha\mathrm{s}\theta_2\mathrm{c}\theta_3+\mathrm{c}\alpha\mathrm{c}\beta\mathrm{c}\theta_2\mathrm{s}\theta_3-\mathrm{s}\alpha\mathrm{s}\beta\mathrm{s}\theta_3)+v\mathrm{c}\alpha\mathrm{s}\theta_2)}\end{aligned}, \tag{3-9a}$$

$$\mathrm{t}\frac{\theta_1}{2}=\frac{\mathrm{s}\gamma(\mathrm{c}\theta_2\mathrm{s}\theta_3+\mathrm{c}\beta\mathrm{s}\theta_2\mathrm{c}\theta_3)+\mathrm{s}\beta\mathrm{c}\gamma\mathrm{s}\theta_2}{(\mathrm{c}\alpha\mathrm{s}\gamma\mathrm{s}\theta_2\mathrm{s}\theta_3-\mathrm{c}\alpha\mathrm{c}\beta\mathrm{s}\gamma\mathrm{c}\theta_2\mathrm{c}\theta_3+\mathrm{s}\alpha\mathrm{s}\beta\mathrm{s}\gamma\mathrm{c}\theta_3-\mathrm{c}\alpha\mathrm{s}\beta\mathrm{c}\gamma\mathrm{c}\theta_2-\mathrm{s}\alpha\mathrm{c}\beta\mathrm{c}\gamma)}, \tag{3-9b}$$

$$\mathrm{t}\frac{\theta_4}{2}=\frac{\mathrm{s}\alpha(\mathrm{s}\theta_2\mathrm{c}\theta_3+\mathrm{c}\beta\mathrm{c}\theta_2\mathrm{s}\theta_3)+\mathrm{c}\alpha\mathrm{s}\beta\mathrm{s}\theta_3}{(\mathrm{s}\alpha\mathrm{c}\gamma\mathrm{s}\theta_2\mathrm{s}\theta_3-\mathrm{s}\alpha\mathrm{c}\beta\mathrm{c}\gamma\mathrm{c}\theta_2\mathrm{c}\theta_3+\mathrm{s}\alpha\mathrm{s}\beta\mathrm{s}\gamma\mathrm{c}\theta_2-\mathrm{c}\alpha\mathrm{s}\beta\mathrm{c}\gamma\mathrm{c}\theta_3-\mathrm{c}\alpha\mathrm{c}\beta\mathrm{s}\gamma)}, \tag{3-9c}$$

$$\theta_5=\theta_3,\ \theta_6=\theta_2, \tag{3-9d}$$

where t, s and c denote tangent, sine and cosine in the equations.

To make the whole assembly with the topology of assembly in Fig. 3-4 mobile, the compatibility on each link commonly shared by three linkages should be satisfied throughout the assembly. Taking the red link shared by linkages A, B, D as an example, its twists and link lengths satisfy

$$\alpha^{\mathrm{B}}-\beta^{\mathrm{D}}=\gamma^{\mathrm{A}},\ u^{\mathrm{B}}+v^{\mathrm{D}}=w^{\mathrm{A}}. \tag{3-10}$$

First, the revolution on joint a_3 is transmitted to joint a_4 through linkage A, which can be derived from the relationships among kinematic variables θ_2^{A}, θ_3^{A} and θ_4^{A},

$$\mathrm{t}\frac{\theta_4^{\mathrm{A}}}{2}=\frac{\left(2\mathrm{s}(\beta^{\mathrm{A}}-\alpha^{\mathrm{A}})\mathrm{t}^2\frac{\theta_2^{\mathrm{A}}}{2}\mathrm{t}\frac{\theta_3^{\mathrm{A}}}{2}-2\mathrm{s}\alpha^{\mathrm{A}}\mathrm{t}\frac{\theta_2^{\mathrm{A}}}{2}\mathrm{t}^2\frac{\theta_3^{\mathrm{A}}}{2}+2\mathrm{s}(\beta^{\mathrm{A}}+\alpha^{\mathrm{A}})\mathrm{t}\frac{\theta_3^{\mathrm{A}}}{2}+2\mathrm{s}\alpha^{\mathrm{A}}\mathrm{t}\frac{\theta_2^{\mathrm{A}}}{2}\right)}{\left(\begin{aligned}&-\mathrm{s}(\alpha^{\mathrm{A}}-\beta^{\mathrm{A}}+\gamma^{\mathrm{A}})\mathrm{t}^2\frac{\theta_2^{\mathrm{A}}}{2}\mathrm{t}^2\frac{\theta_3^{\mathrm{A}}}{2}+\mathrm{s}(\alpha^{\mathrm{A}}-\beta^{\mathrm{A}}-\gamma^{\mathrm{A}})\mathrm{t}^2\frac{\theta_2^{\mathrm{A}}}{2}\\&+\mathrm{s}(\alpha^{\mathrm{A}}+\beta^{\mathrm{A}}-\gamma^{\mathrm{A}})\mathrm{t}^2\frac{\theta_3^{\mathrm{A}}}{2}+4\mathrm{c}\gamma^{\mathrm{A}}\mathrm{s}\alpha^{\mathrm{A}}\mathrm{t}\frac{\theta_2^{\mathrm{A}}}{2}\mathrm{t}\frac{\theta_3^{\mathrm{A}}}{2}-\mathrm{s}(\alpha^{\mathrm{A}}+\beta^{\mathrm{A}}+\gamma^{\mathrm{A}})\end{aligned}\right)}, \tag{3-11a}$$

and

$$\left(u^{\mathrm{A}}-v^{\mathrm{A}}+w^{\mathrm{A}}\right)\mathrm{s}\left(\alpha^{\mathrm{A}}-\beta^{\mathrm{A}}+\gamma^{\mathrm{A}}\right)\mathrm{t}^{2}\frac{\theta_{2}^{\mathrm{A}}}{2}\mathrm{t}^{2}\frac{\theta_{3}^{\mathrm{A}}}{2}+\left(u^{\mathrm{A}}+v^{\mathrm{A}}-w^{\mathrm{A}}\right)\mathrm{s}\left(\alpha^{\mathrm{A}}+\beta^{\mathrm{A}}-\gamma^{\mathrm{A}}\right)\mathrm{t}^{2}\frac{\theta_{3}^{\mathrm{A}}}{2}$$
$$+\left(u^{\mathrm{A}}-v^{\mathrm{A}}-w^{\mathrm{A}}\right)\mathrm{s}\left(\alpha^{\mathrm{A}}-\beta^{\mathrm{A}}-\gamma^{\mathrm{A}}\right)\mathrm{t}^{2}\frac{\theta_{2}^{\mathrm{A}}}{2}+\left(u^{\mathrm{A}}+v^{\mathrm{A}}+w^{\mathrm{A}}\right)\mathrm{s}\left(\alpha^{\mathrm{A}}+\beta^{\mathrm{A}}+\gamma^{\mathrm{A}}\right)$$
$$+2\left(\left(u^{\mathrm{A}}-w^{\mathrm{A}}\right)\mathrm{s}\left(\alpha^{\mathrm{A}}-\gamma^{\mathrm{A}}\right)-\left(u^{\mathrm{A}}+w^{\mathrm{A}}\right)\mathrm{s}\left(\alpha^{\mathrm{A}}+\gamma^{\mathrm{A}}\right)\right)\mathrm{t}\frac{\theta_{2}^{\mathrm{A}}}{2}\mathrm{t}\frac{\theta_{3}^{\mathrm{A}}}{2}=0. \tag{3-11b}$$

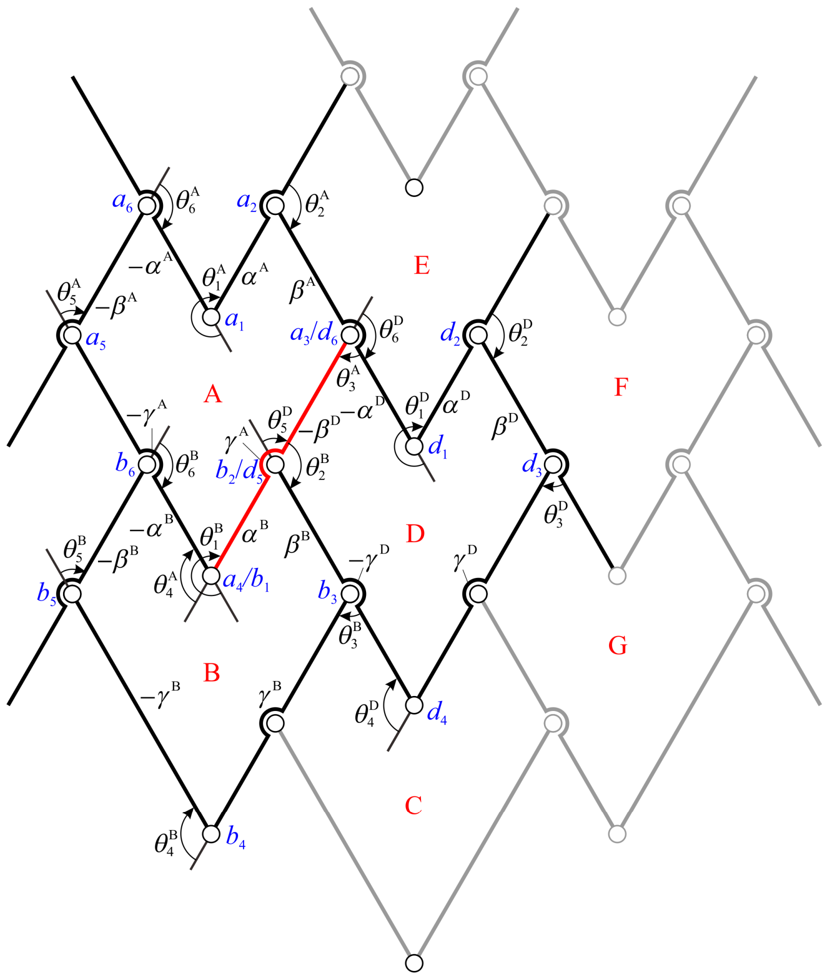

Fig. 3-4 The schematic diagram of mobile assembly with seven plane-symmetric Bricard linkages, where the gray links and joints show the tessellation.

Second, the relationship between θ_1^{B} and θ_2^{B} can be setup in linkage B as

$$\mathrm{t}\frac{\theta_1^{\mathrm{B}}}{2}=\frac{\left(2\mathrm{s}\left(\beta^{\mathrm{B}}-\gamma^{\mathrm{B}}\right)\mathrm{t}\frac{\theta_2^{\mathrm{B}}}{2}\mathrm{t}^2\frac{\theta_3^{\mathrm{B}}}{2}-2\mathrm{s}\gamma^{\mathrm{B}}\mathrm{t}^2\frac{\theta_2^{\mathrm{B}}}{2}\mathrm{t}\frac{\theta_3^{\mathrm{B}}}{2}+2\mathrm{s}\left(\beta^{\mathrm{B}}+\gamma^{\mathrm{B}}\right)\mathrm{t}\frac{\theta_2^{\mathrm{B}}}{2}+2\mathrm{s}\gamma^{\mathrm{B}}\mathrm{t}\frac{\theta_3^{\mathrm{B}}}{2}\right)}{\left(\begin{array}{l}-\mathrm{s}\left(\alpha^{\mathrm{B}}-\beta^{\mathrm{B}}+\gamma^{\mathrm{B}}\right)\mathrm{t}^2\frac{\theta_2^{\mathrm{B}}}{2}\mathrm{t}^2\frac{\theta_3^{\mathrm{B}}}{2}-\mathrm{s}\left(\alpha^{\mathrm{B}}-\beta^{\mathrm{B}}-\gamma^{\mathrm{B}}\right)\mathrm{t}^2\frac{\theta_2^{\mathrm{B}}}{2}\\-\mathrm{s}\left(\alpha^{\mathrm{B}}+\beta^{\mathrm{B}}-\gamma^{\mathrm{B}}\right)\mathrm{t}^2\frac{\theta_3^{\mathrm{B}}}{2}+4\mathrm{c}\alpha^{\mathrm{B}}\mathrm{s}\gamma^{\mathrm{B}}\mathrm{t}\frac{\theta_2^{\mathrm{B}}}{2}\mathrm{t}\frac{\theta_3^{\mathrm{B}}}{2}-\mathrm{s}\left(\alpha^{\mathrm{B}}+\beta^{\mathrm{B}}+\gamma^{\mathrm{B}}\right)\end{array}\right)},$$

(3-12a)

where θ_2^{B} and θ_3^{B} satisfy

$$\begin{aligned}&\left(u^{\mathrm{B}}-v^{\mathrm{B}}+w^{\mathrm{B}}\right)\mathrm{s}\left(\alpha^{\mathrm{B}}-\beta^{\mathrm{B}}+\gamma^{\mathrm{B}}\right)\mathrm{t}^2\frac{\theta_2^{\mathrm{B}}}{2}\mathrm{t}^2\frac{\theta_3^{\mathrm{B}}}{2}+\left(u^{\mathrm{B}}+v^{\mathrm{B}}-w^{\mathrm{B}}\right)\mathrm{s}\left(\alpha^{\mathrm{B}}+\beta^{\mathrm{B}}-\gamma^{\mathrm{B}}\right)\mathrm{t}^2\frac{\theta_3^{\mathrm{B}}}{2}\\&+\left(u^{\mathrm{B}}-v^{\mathrm{B}}-w^{\mathrm{B}}\right)\mathrm{s}\left(\alpha^{\mathrm{B}}-\beta^{\mathrm{B}}-\gamma^{\mathrm{B}}\right)\mathrm{t}^2\frac{\theta_2^{\mathrm{B}}}{2}+\left(u^{\mathrm{B}}+v^{\mathrm{B}}+w^{\mathrm{B}}\right)\mathrm{s}\left(\alpha^{\mathrm{B}}+\beta^{\mathrm{B}}+\gamma^{\mathrm{B}}\right)\\&+2\left(\left(u^{\mathrm{B}}-w^{\mathrm{B}}\right)\mathrm{s}\left(\alpha^{\mathrm{B}}-\gamma^{\mathrm{B}}\right)-\left(u^{\mathrm{B}}+w^{\mathrm{B}}\right)\mathrm{s}\left(\alpha^{\mathrm{B}}+\gamma^{\mathrm{B}}\right)\right)\mathrm{t}\frac{\theta_2^{\mathrm{B}}}{2}\mathrm{t}\frac{\theta_3^{\mathrm{B}}}{2}=0.\end{aligned}$$

(3-12b)

Third, for linkage D, the revolution between θ_5^{D} and θ_6^{D} is related as

$$\begin{aligned}&\left(u^{\mathrm{D}}-v^{\mathrm{D}}+w^{\mathrm{D}}\right)\mathrm{s}\left(\alpha^{\mathrm{D}}-\beta^{\mathrm{D}}+\gamma^{\mathrm{D}}\right)\mathrm{t}^2\frac{\theta_5^{\mathrm{D}}}{2}\mathrm{t}^2\frac{\theta_6^{\mathrm{D}}}{2}+\left(u^{\mathrm{D}}+v^{\mathrm{D}}-w^{\mathrm{D}}\right)\mathrm{s}\left(\alpha^{\mathrm{D}}+\beta^{\mathrm{D}}-\gamma^{\mathrm{D}}\right)\mathrm{t}^2\frac{\theta_5^{\mathrm{D}}}{2}\\&+\left(u^{\mathrm{D}}-v^{\mathrm{D}}-w^{\mathrm{D}}\right)\mathrm{s}\left(\alpha^{\mathrm{D}}-\beta^{\mathrm{D}}-\gamma^{\mathrm{D}}\right)\mathrm{t}^2\frac{\theta_6^{\mathrm{D}}}{2}+\left(u^{\mathrm{D}}+v^{\mathrm{D}}+w^{\mathrm{D}}\right)\mathrm{s}\left(\alpha^{\mathrm{D}}+\beta^{\mathrm{D}}+\gamma^{\mathrm{D}}\right)\\&+2\left(\left(u^{\mathrm{D}}-w^{\mathrm{D}}\right)\mathrm{s}\left(\alpha^{\mathrm{D}}-\gamma^{\mathrm{D}}\right)-\left(u^{\mathrm{D}}+w^{\mathrm{D}}\right)\mathrm{s}\left(\alpha^{\mathrm{D}}+\gamma^{\mathrm{D}}\right)\right)\mathrm{t}\frac{\theta_5^{\mathrm{D}}}{2}\mathrm{t}\frac{\theta_6^{\mathrm{D}}}{2}=0.\end{aligned}$$

(3-13)

Moreover, from the shared joints on the red link, we find joints a_3 and d_6, joints b_2 and d_5, joints a_4 and b_1 are the same joints, respectively, with relationships

$$\theta_3^{\mathrm{A}}+\theta_6^{\mathrm{D}}=\pi, \tag{3-14a}$$

$$\theta_2^{\mathrm{B}}+\theta_5^{\mathrm{D}}=\pi, \tag{3-14b}$$

and

$$\theta_4^{\mathrm{A}}+\theta_1^{\mathrm{B}}=2\pi. \tag{3-14c}$$

Considering the symmetric property of each linkage with $\theta_6^{\mathrm{K}}=\theta_2^{\mathrm{K}}$ and $\theta_5^{\mathrm{K}}=\theta_3^{\mathrm{K}}$, Eqs. (3-13), (3-14a) to (3-14c) become

$$
\begin{aligned}
&\left(u^{\mathrm{D}}-v^{\mathrm{D}}+w^{\mathrm{D}}\right)\mathrm{s}\left(\alpha^{\mathrm{D}}-\beta^{\mathrm{D}}+\gamma^{\mathrm{D}}\right)\mathrm{t}^{2}\frac{\theta_{2}^{\mathrm{D}}}{2}\mathrm{t}^{2}\frac{\theta_{3}^{\mathrm{D}}}{2}+\left(u^{\mathrm{D}}+v^{\mathrm{D}}-w^{\mathrm{D}}\right)\mathrm{s}\left(\alpha^{\mathrm{D}}+\beta^{\mathrm{D}}-\gamma^{\mathrm{D}}\right)\mathrm{t}^{2}\frac{\theta_{3}^{\mathrm{D}}}{2}\\
&+\left(u^{\mathrm{D}}-v^{\mathrm{D}}-w^{\mathrm{D}}\right)\mathrm{s}\left(\alpha^{\mathrm{D}}-\beta^{\mathrm{D}}-\gamma^{\mathrm{D}}\right)\mathrm{t}^{2}\frac{\theta_{2}^{\mathrm{D}}}{2}+\left(u^{\mathrm{D}}+v^{\mathrm{D}}+w^{\mathrm{D}}\right)\mathrm{s}\left(\alpha^{\mathrm{D}}+\beta^{\mathrm{D}}+\gamma^{\mathrm{D}}\right)\\
&+2\left(\left(u^{\mathrm{D}}-w^{\mathrm{D}}\right)\mathrm{s}\left(\alpha^{\mathrm{D}}-\gamma^{\mathrm{D}}\right)-\left(u^{\mathrm{D}}+w^{\mathrm{D}}\right)\mathrm{s}\left(\alpha^{\mathrm{D}}+\gamma^{\mathrm{D}}\right)\right)\mathrm{t}\frac{\theta_{2}^{\mathrm{D}}}{2}\mathrm{t}\frac{\theta_{3}^{\mathrm{D}}}{2}=0,
\end{aligned}
\tag{3-15}
$$

and

$$\theta_3^{\mathrm{A}}+\theta_2^{\mathrm{D}}=\pi\,, \tag{3-16a}$$

$$\theta_2^{\mathrm{B}}+\theta_3^{\mathrm{D}}=\pi\,, \tag{3-16b}$$

$$\theta_4^{\mathrm{A}}+\theta_1^{\mathrm{B}}=2\pi\,. \tag{3-16c}$$

For obtaining the compatibility condition on the red link, we should solve Eqs. (3-11a), (3-11b), (3-12a), (3-12b), (3-15), (3-16a) to (3-16c) by eliminating the revolute variables θ_i^{K}, considering Eq. (3-10). As they compose systems of nonlinear multivariable equations, there could be many solutions, which is difficult to be solved directly. So here we introduce the extra conditions in thick panel origami, and the obtained assembly will be transferred back to generating new thick-panel origami structures. One hand, for the flat-developability, $\alpha_{12}+\alpha_{23}+\alpha_{34}=\pi$, considering

$$
\begin{aligned}
\alpha_{12}^{Br}&=-\alpha_{61}^{Br}=\alpha^{\mathrm{K}}=-\alpha_{12},\\
\alpha_{23}^{Br}&=-\alpha_{56}^{Br}=\beta^{\mathrm{K}}=\alpha_{23}-\pi,\\
\alpha_{34}^{Br}&=-\alpha_{45}^{Br}=\gamma^{\mathrm{K}}=\alpha_{34},
\end{aligned}
\tag{3-17}
$$

we have

$$\alpha^{\mathrm{K}}=\beta^{\mathrm{K}}+\gamma^{\mathrm{K}}\,. \tag{3-18}$$

On the other hand, for the compact flat-foldability, we have $t_{12}+t_{23}-t_{23}'=t_{34}$ according to Eq. (3-3), i.e., for a plane-symmetric linkage

$$u^{\mathrm{K}}+v^{\mathrm{K}}=w^{\mathrm{K}}\,. \tag{3-19}$$

Substitute Eqs. (3-18) and (3-19) into Eqs. (3-11b), (3-12b) and (3-15), we get

$$\left(u^{\mathrm{A}}\mathrm{s}\gamma^{\mathrm{A}}\mathrm{t}\frac{\theta_2^{\mathrm{A}}}{2}\mathrm{t}\frac{\theta_3^{\mathrm{A}}}{2}-w^{\mathrm{A}}\mathrm{s}\alpha^{\mathrm{A}}\right)\left(\mathrm{c}\gamma^{\mathrm{A}}\mathrm{t}\frac{\theta_2^{\mathrm{A}}}{2}\mathrm{t}\frac{\theta_3^{\mathrm{A}}}{2}-\mathrm{c}\alpha^{\mathrm{A}}\right)=0\,, \tag{3-20a}$$

$$\left(u^{\mathrm{B}}\mathrm{s}\gamma^{\mathrm{B}}\mathrm{t}\frac{\theta_2^{\mathrm{B}}}{2}\mathrm{t}\frac{\theta_3^{\mathrm{B}}}{2}-w^{\mathrm{B}}\mathrm{s}\alpha^{\mathrm{B}}\right)\left(\mathrm{c}\gamma^{\mathrm{B}}\mathrm{t}\frac{\theta_2^{\mathrm{B}}}{2}\mathrm{t}\frac{\theta_3^{\mathrm{B}}}{2}-\mathrm{c}\alpha^{\mathrm{B}}\right)=0\,, \tag{3-20b}$$

$$\left(u^{\mathrm{D}}\mathrm{s}\gamma^{\mathrm{D}}\mathrm{t}\frac{\theta_2^{\mathrm{D}}}{2}\mathrm{t}\frac{\theta_3^{\mathrm{D}}}{2}-w^{\mathrm{D}}\mathrm{s}\alpha^{\mathrm{D}}\right)\left(\mathrm{c}\gamma^{\mathrm{D}}\mathrm{t}\frac{\theta_2^{\mathrm{D}}}{2}\mathrm{t}\frac{\theta_3^{\mathrm{D}}}{2}-\mathrm{c}\alpha^{\mathrm{D}}\right)=0\,. \tag{3-20c}$$

Then the following solutions are obtained.

In linkage A

$$\text{AI:}\quad \mathrm{t}\frac{\theta_2^{\mathrm{A}}}{2}\mathrm{t}\frac{\theta_3^{\mathrm{A}}}{2}=\frac{\mathrm{c}\alpha^{\mathrm{A}}}{\mathrm{c}\gamma^{\mathrm{A}}}, \tag{3-21a}$$

$$\text{AII:}\quad \mathrm{t}\frac{\theta_2^{\mathrm{A}}}{2}\mathrm{t}\frac{\theta_3^{\mathrm{A}}}{2}=\frac{w^{\mathrm{A}}\mathrm{s}\alpha^{\mathrm{A}}}{u^{\mathrm{A}}\mathrm{s}\gamma^{\mathrm{A}}}. \tag{3-21b}$$

In linkage B

$$\text{BI:}\quad \mathrm{t}\frac{\theta_2^{\mathrm{B}}}{2}\mathrm{t}\frac{\theta_3^{\mathrm{B}}}{2}=\frac{\mathrm{c}\alpha^{\mathrm{B}}}{\mathrm{c}\gamma^{\mathrm{B}}}, \tag{3-22a}$$

$$\text{BII:}\quad \mathrm{t}\frac{\theta_2^{\mathrm{B}}}{2}\mathrm{t}\frac{\theta_3^{\mathrm{B}}}{2}=\frac{w^{\mathrm{B}}\mathrm{s}\alpha^{\mathrm{B}}}{u^{\mathrm{B}}\mathrm{s}\gamma^{\mathrm{B}}}. \tag{3-22b}$$

In linkage D

$$\text{DI:}\quad \mathrm{t}\frac{\theta_2^{\mathrm{D}}}{2}\mathrm{t}\frac{\theta_3^{\mathrm{D}}}{2}=\frac{\mathrm{c}\alpha^{\mathrm{D}}}{\mathrm{c}\gamma^{\mathrm{D}}}, \tag{3-23a}$$

$$\text{DII:}\quad \mathrm{t}\frac{\theta_2^{\mathrm{D}}}{2}\mathrm{t}\frac{\theta_3^{\mathrm{D}}}{2}=\frac{w^{\mathrm{D}}\mathrm{s}\alpha^{\mathrm{D}}}{u^{\mathrm{D}}\mathrm{s}\gamma^{\mathrm{D}}}. \tag{3-23b}$$

Each linkage is a plane-symmetric Bricard linkage with six active joints, so $\tan(\theta_2^{\mathrm{K}}/2)\tan(\theta_3^{\mathrm{K}}/2)$ are not always zero or infinity.

As each linkage has two relationships between θ_2^{K} and θ_3^{K}, the assembly of the three linkages has eight types of the combination of the relationships, which are named *motion types*, i.e., AI-BI-DI, AI-BI-DII, AI-BII-DI, AII-BI-DI, AI-BII-DII, AII-BI-DII, AII-BII-DI, AII-BII-DII. Compatibility conditions on the red link should be analyzed under the motion types.

For motion type AI-BI-DI and considering Eqs. (3-16a) and (3-16b), we have

$$\begin{aligned}&\mathrm{t}\frac{\theta_2^{\mathrm{B}}}{2}\mathrm{t}\frac{\theta_3^{\mathrm{D}}}{2}=1,\ \mathrm{t}\frac{\theta_3^{\mathrm{B}}}{2}=\frac{\mathrm{c}\alpha^{\mathrm{B}}}{\mathrm{c}\gamma^{\mathrm{B}}}\mathrm{t}\frac{\theta_3^{\mathrm{D}}}{2},\\&\mathrm{t}\frac{\theta_2^{\mathrm{A}}}{2}\mathrm{t}\frac{\theta_3^{\mathrm{D}}}{2}=\frac{\mathrm{c}\alpha^{\mathrm{A}}\mathrm{c}\alpha^{\mathrm{D}}}{\mathrm{c}\gamma^{\mathrm{A}}\mathrm{c}\gamma^{\mathrm{D}}},\ \mathrm{t}\frac{\theta_3^{\mathrm{A}}}{2}=\frac{\mathrm{c}\gamma^{\mathrm{D}}}{\mathrm{c}\alpha^{\mathrm{D}}}\mathrm{t}\frac{\theta_3^{\mathrm{D}}}{2}.\end{aligned} \tag{3-24}$$

By substituting Eq. (3-24) into Eqs. (3-11a) and (3-12a), we get

$$\mathrm{t}\frac{\theta_4^{\mathrm{A}}}{2}\mathrm{t}\frac{\theta_3^{\mathrm{D}}}{2}=\frac{\mathrm{c}\alpha^{\mathrm{D}}}{\mathrm{c}\gamma^{\mathrm{D}}\mathrm{c}\gamma^{\mathrm{A}}},\ \mathrm{t}\frac{\theta_1^{\mathrm{B}}}{2}\mathrm{t}\frac{\theta_3^{\mathrm{D}}}{2}=-\frac{1}{\mathrm{c}\alpha^{\mathrm{B}}}. \tag{3-25}$$

With $\theta_4^{\mathrm{A}}+\theta_1^{\mathrm{B}}=2\pi$ in Eq. (3-16c), we have

$$\mathrm{c}\alpha^{\mathrm{D}}\mathrm{c}\alpha^{\mathrm{B}} = \mathrm{c}\gamma^{\mathrm{D}}\mathrm{c}\gamma^{\mathrm{A}}. \tag{3-26}$$

Two solutions for the compatibility condition on the red link under motion type AI-BI-DI are obtained

$$\begin{aligned} &\gamma^{\mathrm{D}} = \alpha^{\mathrm{D}},\ \gamma^{\mathrm{A}} = \alpha^{\mathrm{B}},\ \alpha^{\mathrm{K}} = \beta^{\mathrm{K}} + \gamma^{\mathrm{K}}, \\ &u^{\mathrm{B}} + v^{\mathrm{D}} = w^{\mathrm{A}},\ u^{\mathrm{K}} + v^{\mathrm{K}} = w^{\mathrm{K}}, \end{aligned} \tag{3-27a}$$

and

$$\begin{aligned} &\alpha^{\mathrm{D}} = -\gamma^{\mathrm{A}},\ \gamma^{\mathrm{D}} = -\alpha^{\mathrm{B}},\ \alpha^{\mathrm{K}} = \beta^{\mathrm{K}} + \gamma^{\mathrm{K}}, \\ &u^{\mathrm{B}} + v^{\mathrm{D}} = w^{\mathrm{A}},\ u^{\mathrm{K}} + v^{\mathrm{K}} = w^{\mathrm{K}}. \end{aligned} \tag{3-27b}$$

Similarly, compatibility conditions on the red link for the eight motion types are obtained and expressed in the section 3.5. With the comparison among the conditions of eight motion types, there are only five distinct motion types, as AI-BI-DI, AI-BI-DII, AI-BII-DII, AII-BI-DII, AII-BII-DI.

To ensure the mobility of the assembly in Fig. 3-4, each of the links shared by three linkages should satisfy the compatibility condition under a specific motion type. When all links have same compatibility conditions to Eq. (3-27a) or (3-27b), we can get the compatibility conditions on the other shared links as

$$\begin{aligned} &ADE: \alpha^{\mathrm{A}} = \gamma^{\mathrm{A}},\ \gamma^{\mathrm{E}} = \alpha^{\mathrm{D}},\ u^{\mathrm{D}} + v^{\mathrm{A}} = w^{\mathrm{E}}, \\ &DBA: \alpha^{\mathrm{D}} = \gamma^{\mathrm{D}},\ \gamma^{\mathrm{A}} = \alpha^{\mathrm{B}},\ u^{\mathrm{B}} + v^{\mathrm{D}} = w^{\mathrm{A}}, \\ &BCD: \alpha^{\mathrm{B}} = \gamma^{\mathrm{B}},\ \gamma^{\mathrm{D}} = \alpha^{\mathrm{C}},\ u^{\mathrm{C}} + v^{\mathrm{B}} = w^{\mathrm{D}}, \\ &FDE: \alpha^{\mathrm{F}} = \gamma^{\mathrm{F}},\ \gamma^{\mathrm{E}} = \alpha^{\mathrm{D}},\ u^{\mathrm{D}} + v^{\mathrm{F}} = w^{\mathrm{E}}, \\ &DGF: \alpha^{\mathrm{D}} = \gamma^{\mathrm{D}},\ \gamma^{\mathrm{F}} = \alpha^{\mathrm{G}},\ u^{\mathrm{G}} + v^{\mathrm{D}} = w^{\mathrm{F}}, \\ &GCD: \alpha^{\mathrm{G}} = \gamma^{\mathrm{G}},\ \gamma^{\mathrm{D}} = \alpha^{\mathrm{C}},\ u^{\mathrm{C}} + v^{\mathrm{G}} = w^{\mathrm{D}}, \end{aligned} \tag{3-28a}$$

and

$$\begin{aligned} &ADE: \alpha^{\mathrm{A}} = -\gamma^{\mathrm{E}},\ \gamma^{\mathrm{A}} = -\alpha^{\mathrm{D}},\ u^{\mathrm{D}} + v^{\mathrm{A}} = w^{\mathrm{E}}, \\ &DBA: \alpha^{\mathrm{D}} = -\gamma^{A},\ \gamma^{\mathrm{D}} = -\alpha^{\mathrm{B}},\ u^{\mathrm{B}} + v^{\mathrm{D}} = w^{\mathrm{A}}, \\ &BCD: \alpha^{\mathrm{B}} = -\gamma^{\mathrm{D}},\ \gamma^{\mathrm{B}} = -\alpha^{\mathrm{C}},\ u^{\mathrm{C}} + v^{\mathrm{B}} = w^{\mathrm{D}}, \\ &FDE: \alpha^{\mathrm{F}} = -\gamma^{\mathrm{E}},\ \gamma^{\mathrm{F}} = -\alpha^{\mathrm{D}},\ u^{\mathrm{D}} + v^{\mathrm{F}} = w^{\mathrm{E}}, \\ &DGF: \alpha^{\mathrm{D}} = -\gamma^{\mathrm{F}},\ \gamma^{\mathrm{D}} = -\alpha^{\mathrm{G}},\ u^{\mathrm{G}} + v^{\mathrm{D}} = w^{\mathrm{F}}, \\ &GCD: \alpha^{\mathrm{G}} = -\gamma^{\mathrm{D}},\ \gamma^{\mathrm{G}} = -\alpha^{\mathrm{C}},\ u^{\mathrm{C}} + v^{\mathrm{G}} = w^{\mathrm{D}}, \end{aligned} \tag{3-28b}$$

where all the linkages satisfy Eqs. (3-18) and (3-19). Simplifying Eqs. (3-28a) and (3-28b), we obtain two cases, case I and case II assemblies, as

$$\begin{aligned}
&\alpha^{\mathrm{A}} = \gamma^{\mathrm{A}} = \alpha^{\mathrm{B}} = \gamma^{\mathrm{B}} = \varepsilon_{j-1},\\
&\alpha^{\mathrm{C}} = \gamma^{\mathrm{C}} = \alpha^{\mathrm{D}} = \gamma^{\mathrm{D}} = \alpha^{\mathrm{E}} = \gamma^{\mathrm{E}} = \varepsilon_{j},\\
&\alpha^{\mathrm{F}} = \gamma^{\mathrm{F}} = \alpha^{\mathrm{G}} = \gamma^{\mathrm{G}} = \varepsilon_{j+1},\ \beta^{\mathrm{K}} = 0,\\
&u^{\mathrm{K}} + v^{\mathrm{K}} = w^{\mathrm{K}},\ v^{\mathrm{A}} = v^{\mathrm{F}} = w^{\mathrm{E}} - u^{\mathrm{D}},\\
&v^{\mathrm{B}} = v^{\mathrm{G}} = w^{\mathrm{D}} - u^{\mathrm{C}},\ v^{\mathrm{D}} = w^{\mathrm{A}} - u^{\mathrm{B}} = w^{\mathrm{F}} - u^{\mathrm{G}},
\end{aligned} \tag{3-29a}$$

and

$$\begin{aligned}
&\alpha^{\mathrm{A}} = -\gamma^{\mathrm{E}} = \alpha^{\mathrm{F}} = \delta_{j-2},\ \beta^{\mathrm{A}} = \beta^{\mathrm{F}} = \delta_{j-2} + \delta_{j-1},\\
&\gamma^{\mathrm{A}} = -\alpha^{\mathrm{D}} = \gamma^{\mathrm{F}} = -\delta_{j-1},\ \beta^{\mathrm{D}} = \delta_{j-1} + \delta_{j},\\
&\alpha^{\mathrm{B}} = -\gamma^{\mathrm{D}} = \alpha^{\mathrm{G}} = \delta_{j},\ \beta^{\mathrm{B}} = \beta^{\mathrm{G}} = \delta_{j} + \delta_{j+1},\\
&\gamma^{\mathrm{B}} = -\alpha^{\mathrm{C}} = \gamma^{\mathrm{G}} = -\delta_{j+1},\ \beta^{\mathrm{C}} = \delta_{j+1} + \delta_{j+2},\\
&u^{\mathrm{K}} + v^{\mathrm{K}} = w^{\mathrm{K}},\ v^{\mathrm{A}} = v^{\mathrm{F}} = w^{\mathrm{E}} - u^{\mathrm{D}},\\
&v^{\mathrm{B}} = v^{\mathrm{G}} = w^{\mathrm{D}} - u^{\mathrm{C}},\ v^{\mathrm{D}} = w^{\mathrm{A}} - u^{\mathrm{B}} = w^{\mathrm{F}} - u^{\mathrm{G}}.
\end{aligned} \tag{3-29b}$$

As ε_j's in Eq. (3-29a) can be different for case I assembly, all plane-symmetric Bricard linkages on the same guideline X_j, such as linkage C, D, E are identical, but the linkages on different X-guidelines can be with different twists, as shown in Fig. 3-5(a). Similarly, for case II assembly, in Fig. 3-5(b), the linkages on the same guideline Y_j are identical, while those on different Y-guidelines are of different twist δ_j. The prototypes of both cases are shown in Fig. 3-6. However, those two cases cannot be combined together to have both X-guideline and Y-guideline at the same time, which will only lead to the assembly with all Bricard linkages identical rather than all of them are different.

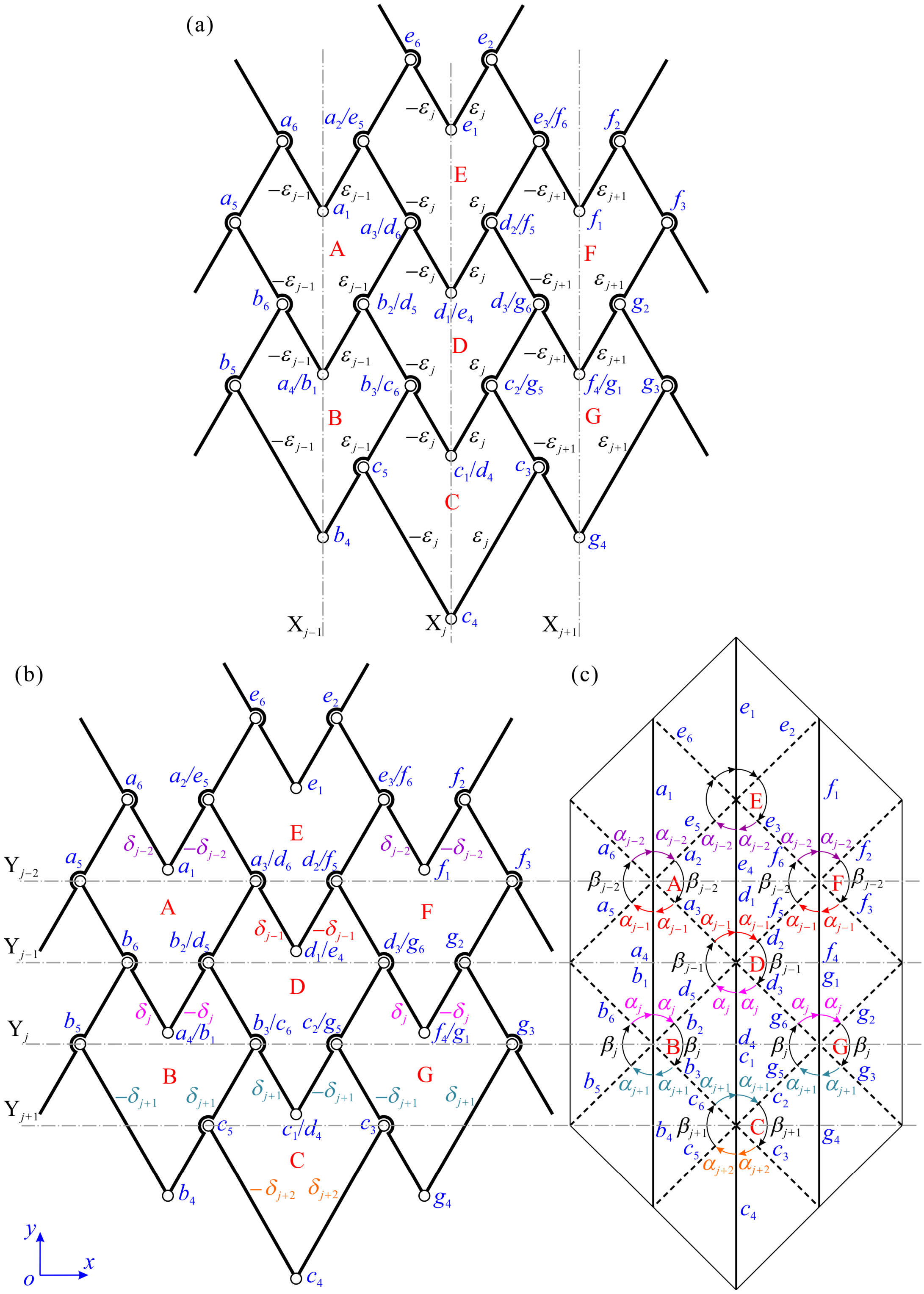

Fig. 3-5 Schematic diagrams of (a) case I, (b) case II assemblies with vertical guidelines X_j and horizontal guidelines Y_j and the crease pattern of graded diamond thick-panel pattern corresponding to case II assembly. Here same colored angles in (b) and (c) have relationships expressed in Eq. (3-30).

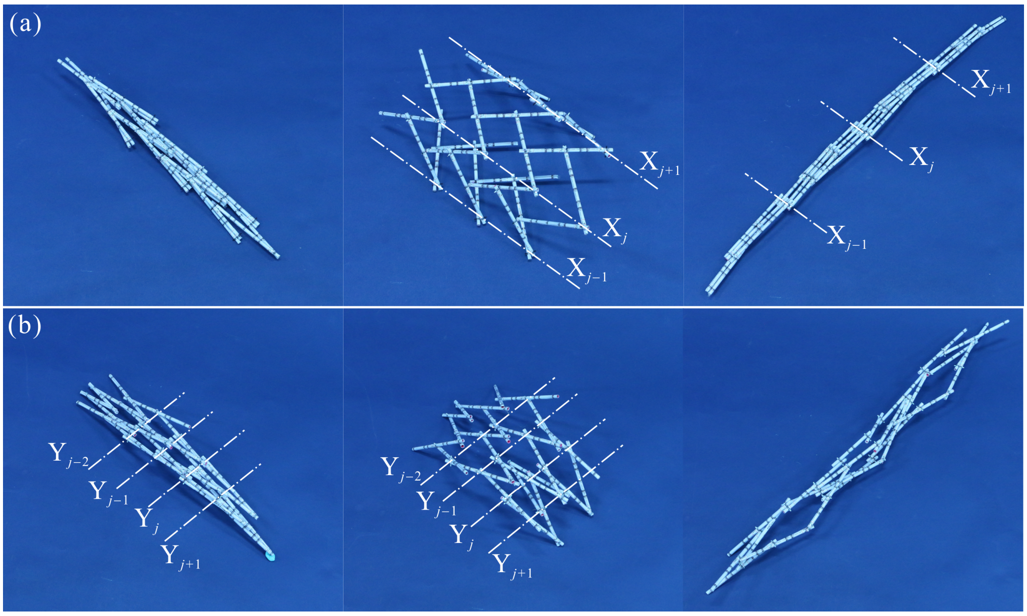

Fig. 3-6 Motion sequences of (a) case I and (b) case II mobile assemblies of plane-symmetric Bricard linkages with guidelines X_j and Y_j, respectively.

3.4 Variation of the Diamond Thick-Panel Origami Patterns

Cases I and II extend the construct condition of mobile assembly of plane-symmetric Bricard linkages. Considering the kinematic equivalence between the mobile assembly and thick-panel origami, they should subsequently enhance the geometric variation in the diamond thick-panel origami.

For case I, X-guideline cannot apply to diamond thick-panel origami, as the twists of linkage lead to negative sector angles of origami from Eq. (3-17). Meanwhile, applying X-guideline would destroy the plane-symmetric property of diamond thick-panel origami. For case II, twists of Bricard linkages on different Y-guidelines can be different (Fig. 3-5(b)). So correspondingly, in the diamond thick-panel pattern, sector angles can be different along different rows of vertices, see Fig. 3-5(c), which is called the *graded diamond thick-panel origami pattern*. The geometric condition for constructing graded diamond thick-panel origami pattern is derived from Eqs. (3-17) and (3-29b)

$$\begin{aligned}
&\alpha_{j-2}=-\delta_{j-2},\ \beta_{j-2}=\delta_{j-2}+\delta_{j-1}+\pi,\\
&\alpha_{j-1}=-\delta_{j-1},\ \beta_{j-1}=\delta_{j-1}+\delta_{j}+\pi,\\
&\alpha_{j}=-\delta_{j},\ \beta_{j}=\delta_{j}+\delta_{j+1}+\pi,\\
&\alpha_{j+1}=-\delta_{j+1},\ \beta_{j+1}=\delta_{j+1}+\delta_{j+2}+\pi,\ \alpha_{j+2}=-\delta_{j+2},\\
&u^{\mathrm{K}}+v^{\mathrm{K}}=w^{\mathrm{K}},\ v^{\mathrm{A}}=v^{\mathrm{F}}=w^{\mathrm{E}}-u^{\mathrm{D}},\\
&v^{\mathrm{B}}=v^{\mathrm{G}}=w^{\mathrm{D}}-u^{\mathrm{C}},\ v^{\mathrm{D}}=w^{\mathrm{A}}-u^{\mathrm{B}}=w^{\mathrm{F}}-u^{\mathrm{G}},
\end{aligned}\tag{3-30}$$

where $-\pi/4 \le \delta_j < 0$, to satisfy the flat foldability in every origami vertex. α_j and β_j are the sector angles in the diamond origami pattern in Fig. 3-5(c).

On the other hand, Fig. 3-3(a) shows that the diamond thick-panel origami is not completely flat but with stairs in the fully unfolded configuration due to the thickness arrangement. However, the thick-panel pattern with flat unfolded profiles is more useful in terms of application. Referring back to the general mobile assembly of plane-symmetric Bricard linkages in case II, it is possible to remove the stairs. Taking a close look at the diamond thick-panel origami vertex in Fig. 3-1(c), stairs are caused by the panels P_{23} and P_{56} whose sizes correspond to link lengths $t_{23}-t'_{23}=t_{56}-t'_{56}=a_{23}^{Br}=a_{56}^{Br}=v^{Br}$. To obtain panels with flat unfolded profiles, we set link lengths $v^{Br}=0$ and $u^{Br}=w^{Br}$. If all plane-symmetric Bricard linkages of mobile assembly in Fig. 3-2(c) satisfy $v^{\mathrm{K}}=0$ and $u^{\mathrm{K}}=w^{\mathrm{K}}$, its corresponding diamond thick-panel pattern would have a flat unfolded profile. Such diamond thick-panel pattern and its corresponding mobile assembly are shown in Fig. 3-7, in which the mobile assembly of Bricard linkages is very different from that one in Fig. 3-3(b) due to the zero link length.

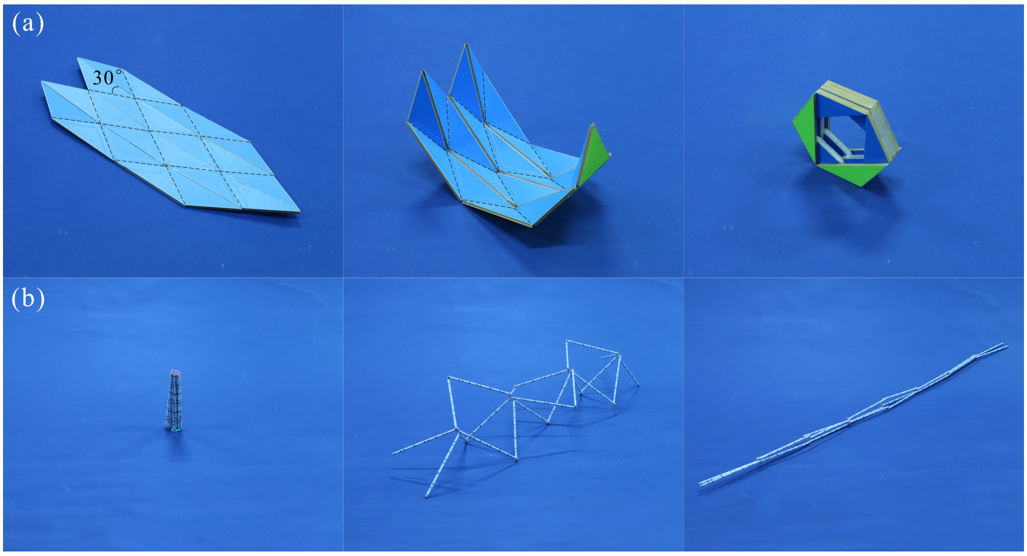

Fig. 3-7 Motion sequences of (a) a diamond thick-panel origami pattern with flat unfolded profiles and (b) its corresponding mobile assembly with $\alpha^{\mathrm{K}}=-30°$, $v^{\mathrm{K}}=0$, $u^{\mathrm{K}}=w^{\mathrm{K}}$.

As this diamond thick-panel origami pattern is folded to an arch, the tessellation along the axial direction can be infinitely extended. But infinite tessellation along the circumferential direction would cause interference during folding, which can be avoided by setting sector angles of the diamond thick-panel origami along the circumferential direction, i.e., the Y-guideline direction in Fig. 3-5(c), changing gradually. They should satisfy the condition of the graded diamond thick-panel origami pattern for mobility in Eq. (3-30). By setting $v^{\mathrm{K}}=0$ and $u^{\mathrm{K}}=w^{\mathrm{K}}$ of case II mobile assembly, a graded diamond thick-panel pattern with flat unfolded profiles can be generated, as shown in Fig. 3-8, which is folded spirally.

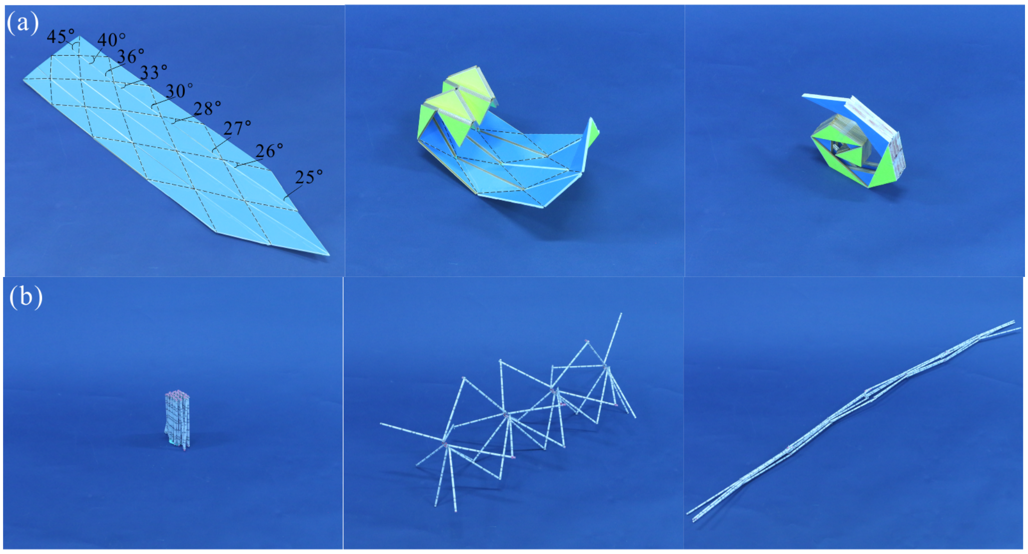

Fig. 3-8 Motion sequences of (a) a graded diamond thick-panel origami pattern with flat unfolded profiles and (b) its corresponding mobile assembly of plane-symmetric Bricard linkages with $v^{\mathrm{K}}=0$, $u^{\mathrm{K}}=w^{\mathrm{K}}$.

3.5 Solutions of Motion Types

Compatibility conditions on the red link of eight motion types are expressed in this part, which are derived from the similar method in section 3.3, as AI-BI-DI, AI-BI-DII, AI-BII-DI, AII-BI-DI, AI-BII-DII, AII-BI-DII, AII-BII-DI, AII-BII-DII.

For the motion type AI-BI-DI, we have two solutions,

$$\begin{aligned}&\alpha^{\mathrm{D}}=-\gamma^{\mathrm{A}},\ \gamma^{\mathrm{D}}=-\alpha^{\mathrm{B}},\ \alpha^{\mathrm{K}}=\beta^{\mathrm{K}}+\gamma^{\mathrm{K}},\\&u^{\mathrm{B}}+v^{\mathrm{D}}=w^{\mathrm{A}},\ u^{\mathrm{K}}+v^{\mathrm{K}}=w^{\mathrm{K}},\end{aligned}\tag{3-31a}$$

and

$$\begin{aligned}&\gamma^{\mathrm{D}}=\alpha^{\mathrm{D}},\ \gamma^{\mathrm{A}}=\alpha^{\mathrm{B}},\ \alpha^{\mathrm{K}}=\beta^{\mathrm{K}}+\gamma^{\mathrm{K}},\\&u^{\mathrm{B}}+v^{\mathrm{D}}=w^{\mathrm{A}},\ u^{\mathrm{K}}+v^{\mathrm{K}}=w^{\mathrm{K}}.\end{aligned}\tag{3-31b}$$

Its corresponding models are the parts with linkages A, B and D of case I and case II assemblies in Fig. 3-6.

For the motion type AI-BI-DII, we have one solution,

$$
\begin{aligned}
&\alpha^{\mathrm{B}} = \beta^{\mathrm{D}} + \gamma^{\mathrm{A}},\ \alpha^{\mathrm{K}} = \beta^{\mathrm{K}} + \gamma^{\mathrm{K}},\\
&u^{\mathrm{B}} + v^{\mathrm{D}} = w^{\mathrm{A}},\ u^{\mathrm{K}} + v^{\mathrm{K}} = w^{\mathrm{K}},\\
&\lambda^{\mathrm{D}} = \frac{w^{\mathrm{D}}}{u^{\mathrm{D}}} = \frac{\mathrm{s}\gamma^{\mathrm{D}}}{\mathrm{s}\alpha^{\mathrm{D}}} \cdot \frac{\mathrm{c}\gamma^{\mathrm{A}}}{\mathrm{c}\alpha^{\mathrm{B}}}.
\end{aligned} \tag{3-32}
$$

When we choose the following parameters in Eq. (3-33), where the unit of the link lengths is millimeter, a model of motion type AI-BI-DII is constructed, as shown in Fig. 3-9.

$$
\begin{aligned}
&\alpha^{\mathrm{A}} = -30°,\ \beta^{\mathrm{A}} = -75°,\ \gamma^{\mathrm{A}} = 45°,\ u^{\mathrm{A}} = 4,\ w^{\mathrm{A}} = 11.464,\\
&\alpha^{\mathrm{B}} = 75°,\ \beta^{\mathrm{B}} = 45°,\ \gamma^{\mathrm{B}} = 30°,\ u^{\mathrm{B}} = 4,\ w^{\mathrm{B}} = 8,\\
&\alpha^{\mathrm{D}} = -30°,\ \beta^{\mathrm{D}} = 30°,\ \gamma^{\mathrm{D}} = -60°,\ u^{\mathrm{D}} = 2,\ \lambda^{\mathrm{D}} = 4.732.
\end{aligned} \tag{3-33}
$$

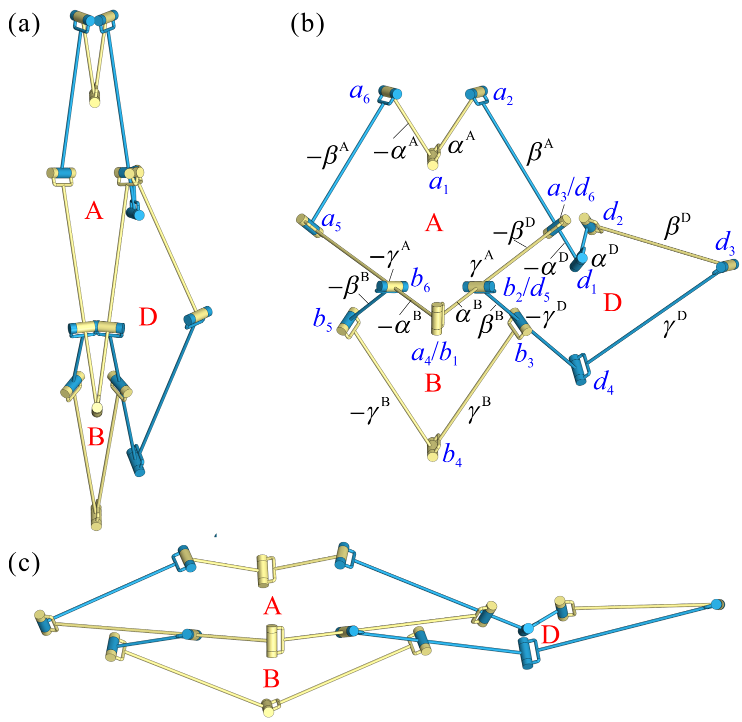

Fig. 3-9 (a)-(c) The motion sequence of a model of motion type AI-BI-DII.

For the motion type AI-BII-DI, we have two special solutions,

$$
\begin{aligned}
&\alpha^{\mathrm{D}} = -\gamma^{\mathrm{A}},\ \gamma^{\mathrm{D}} = -\alpha^{\mathrm{B}},\ \alpha^{\mathrm{K}} = \beta^{\mathrm{K}} + \gamma^{\mathrm{K}},\\
&u^{\mathrm{B}} + v^{\mathrm{D}} = w^{\mathrm{A}},\ u^{\mathrm{K}} + v^{\mathrm{K}} = w^{\mathrm{K}},\\
&\lambda^{\mathrm{B}} = \frac{w^{\mathrm{B}}}{u^{\mathrm{B}}} = \frac{\mathrm{t}\gamma^{\mathrm{B}}}{\mathrm{t}\alpha^{\mathrm{B}}},
\end{aligned} \tag{3-34a}
$$

and

$$\begin{aligned}&\gamma^{\mathrm{D}}=\alpha^{\mathrm{D}},\ \gamma^{\mathrm{A}}=\alpha^{\mathrm{B}},\ \alpha^{\mathrm{K}}=\beta^{\mathrm{K}}+\gamma^{\mathrm{K}},\\&u^{\mathrm{B}}+v^{\mathrm{D}}=w^{\mathrm{A}},\ u^{\mathrm{K}}+v^{\mathrm{K}}=w^{\mathrm{K}},\\&\lambda^{\mathrm{B}}=\frac{w^{\mathrm{B}}}{u^{\mathrm{B}}}=\frac{\mathrm{t}\gamma^{\mathrm{B}}}{\mathrm{t}\alpha^{\mathrm{B}}}.\end{aligned}\tag{3-34b}$$

The Eqs. (3-34a) and (3-34b) are special cases of AI-BI-DI in Eq. (3-31a) and Eq. (3-31b), respectively.

For the motion type AII-BI-DI, we have two special solutions, as

$$\begin{aligned}&\alpha^{\mathrm{D}}=-\gamma^{\mathrm{A}},\ \gamma^{\mathrm{D}}=-\alpha^{\mathrm{B}},\ \alpha^{\mathrm{K}}=\beta^{\mathrm{K}}+\gamma^{\mathrm{K}},\\&u^{\mathrm{B}}+v^{\mathrm{D}}=w^{\mathrm{A}},\ u^{\mathrm{K}}+v^{\mathrm{K}}=w^{\mathrm{K}},\\&\lambda^{\mathrm{A}}=\frac{w^{\mathrm{A}}}{u^{\mathrm{A}}}=\frac{\mathrm{t}\gamma^{\mathrm{A}}}{\mathrm{t}\alpha^{\mathrm{A}}},\end{aligned}\tag{3-35a}$$

and

$$\begin{aligned}&\gamma^{\mathrm{D}}=\alpha^{\mathrm{D}},\ \gamma^{\mathrm{A}}=\alpha^{\mathrm{B}},\ \alpha^{\mathrm{K}}=\beta^{\mathrm{K}}+\gamma^{\mathrm{K}},\\&u^{\mathrm{B}}+v^{\mathrm{D}}=w^{\mathrm{A}},\ u^{\mathrm{K}}+v^{\mathrm{K}}=w^{\mathrm{K}},\\&\lambda^{\mathrm{A}}=\frac{w^{\mathrm{A}}}{u^{\mathrm{A}}}=\frac{\mathrm{t}\gamma^{\mathrm{A}}}{\mathrm{t}\alpha^{\mathrm{A}}}.\end{aligned}\tag{3-35b}$$

The Eqs. (3-35a) and (3-35b) are special cases of AI-BI-DI in Eqs. (3-31a) and (3-31b), respectively.

For the motion type AI-BII-DII, we have

$$\begin{aligned}&\gamma^{\mathrm{A}}=\alpha^{\mathrm{B}}-\alpha^{\mathrm{D}}+\gamma^{\mathrm{D}},\ \beta^{\mathrm{K}}=\alpha^{\mathrm{K}}-\gamma^{\mathrm{K}},\\&w^{\mathrm{B}}=\lambda^{\mathrm{B}}u^{\mathrm{B}},\ w^{\mathrm{D}}=\lambda^{\mathrm{D}}u^{\mathrm{D}},\\&w^{\mathrm{A}}=u^{\mathrm{B}}-u^{\mathrm{D}}+w^{\mathrm{D}},\ v^{\mathrm{K}}=w^{\mathrm{K}}-u^{\mathrm{K}},\end{aligned}\tag{3-36}$$

where λ^{B} and λ^{D} have three special cases, as

$$\begin{aligned}&\lambda^{\mathrm{B}}=-\frac{\mathrm{s}\gamma^{\mathrm{B}}}{2\mathrm{c}\dfrac{\alpha^{\mathrm{B}}}{2}\mathrm{s}\left(\dfrac{\alpha^{\mathrm{B}}}{2}-\gamma^{\mathrm{B}}\right)},\\&\lambda^{\mathrm{D}}=\frac{\mathrm{c}\left(\alpha^{\mathrm{D}}-\alpha^{\mathrm{B}}-\gamma^{\mathrm{D}}\right)\mathrm{s}\gamma^{\mathrm{D}}\mathrm{s}\left(\dfrac{\alpha^{\mathrm{B}}}{2}-\gamma^{\mathrm{B}}\right)}{\mathrm{c}\left(\alpha^{\mathrm{B}}-\gamma^{\mathrm{B}}\right)\mathrm{s}\dfrac{\alpha^{\mathrm{B}}}{2}\mathrm{s}\alpha^{\mathrm{D}}},\end{aligned}\tag{3-37a}$$

$$\lambda^{\mathrm{B}} = \frac{\mathrm{s}\gamma^{\mathrm{B}}}{2\mathrm{s}\dfrac{\alpha^{\mathrm{B}}}{2}\mathrm{c}\left(\dfrac{\alpha^{\mathrm{B}}}{2}-\gamma^{\mathrm{B}}\right)},$$
$$\lambda^{\mathrm{D}} = \frac{\mathrm{c}\left(\alpha^{\mathrm{D}}-\alpha^{\mathrm{B}}-\gamma^{\mathrm{D}}\right)\mathrm{s}\gamma^{\mathrm{D}}\mathrm{c}\left(\dfrac{\alpha^{\mathrm{B}}}{2}-\gamma^{\mathrm{B}}\right)}{\mathrm{c}\left(\alpha^{\mathrm{B}}-\gamma^{\mathrm{B}}\right)\mathrm{c}\dfrac{\alpha^{\mathrm{B}}}{2}\mathrm{s}\alpha^{\mathrm{D}}}, \tag{3-37b}$$

and

$$\lambda^{\mathrm{B}} = \frac{\mathrm{t}\gamma^{\mathrm{B}}}{\mathrm{t}\alpha^{\mathrm{B}}},$$
$$\lambda^{\mathrm{D}} = \frac{\mathrm{c}\left(\alpha^{\mathrm{D}}-\alpha^{\mathrm{B}}-\gamma^{\mathrm{D}}\right)\mathrm{s}\gamma^{\mathrm{D}}}{\mathrm{c}\cos\alpha^{\mathrm{B}}\mathrm{s}\alpha^{\mathrm{D}}}. \tag{3-37c}$$

According to the following parameters in Eqs. (3-38a) to (3-38c), models of motion type AI-BII-DII are constructed, as shown in Fig. 3-10 to Fig. 3-12.

$$\begin{aligned}
&\alpha^{\mathrm{A}}=-30°,\ \beta^{\mathrm{A}}=-60°,\ \gamma^{\mathrm{A}}=30°,\ u^{\mathrm{A}}=4,\ w^{\mathrm{A}}=8,\\
&\alpha^{\mathrm{B}}=-120°,\ \beta^{\mathrm{B}}=150°,\ \gamma^{\mathrm{B}}=30°,\ u^{\mathrm{B}}=4,\ \lambda^{\mathrm{B}}=1/2,\\
&\alpha^{\mathrm{D}}=-30°,\ \beta^{\mathrm{D}}=-150°,\ \gamma^{\mathrm{D}}=120°,\ u^{\mathrm{D}}=4,\ \lambda^{\mathrm{D}}=2;
\end{aligned} \tag{3-38a}$$

$$\begin{aligned}
&\alpha^{\mathrm{A}}=45°,\ \beta^{\mathrm{A}}=15°,\ \gamma^{\mathrm{A}}=30°,\ u^{\mathrm{A}}=6,\ w^{\mathrm{A}}=8,\\
&\alpha^{\mathrm{B}}=60°,\ \beta^{\mathrm{B}}=-30°,\ \gamma^{\mathrm{B}}=30°,\ u^{\mathrm{B}}=12,\ \lambda^{\mathrm{B}}=1/2,\\
&\alpha^{\mathrm{D}}=60°,\ \beta^{\mathrm{D}}=-30°,\ \gamma^{\mathrm{D}}=30°,\ u^{\mathrm{D}}=12,\ \lambda^{\mathrm{D}}=2/3;
\end{aligned} \tag{3-38b}$$

$$\begin{aligned}
&\alpha^{\mathrm{A}}=-30°,\ \beta^{\mathrm{A}}=-60°,\ \gamma^{\mathrm{A}}=30°,\ u^{\mathrm{A}}=4,\ w^{\mathrm{A}}=12,\\
&\alpha^{\mathrm{B}}=-120°,\ \beta^{\mathrm{B}}=150°,\ \gamma^{\mathrm{B}}=30°,\ u^{\mathrm{B}}=4,\ \lambda^{\mathrm{B}}=1/3,\\
&\alpha^{\mathrm{D}}=-30°,\ \beta^{\mathrm{D}}=-150°,\ \gamma^{\mathrm{D}}=120°,\ u^{\mathrm{D}}=4,\ \lambda^{\mathrm{D}}=3.
\end{aligned} \tag{3-38c}$$

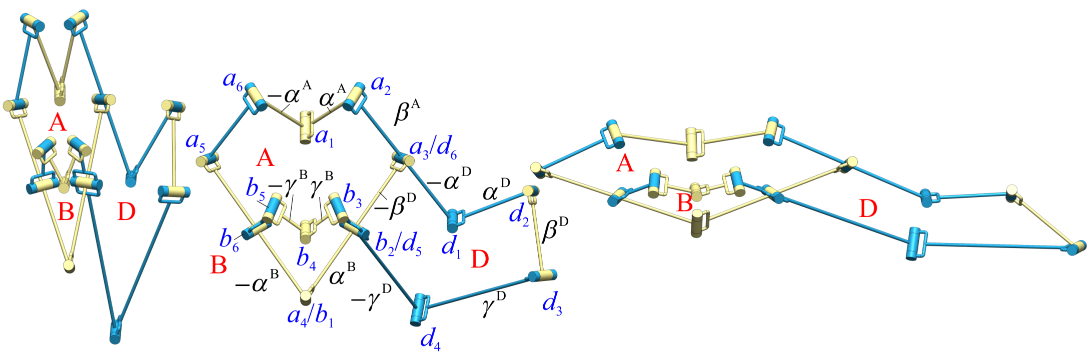

Fig. 3-10 The motion sequence of a model of motion type AI-BII-DII according to the Eq. (3-38a).

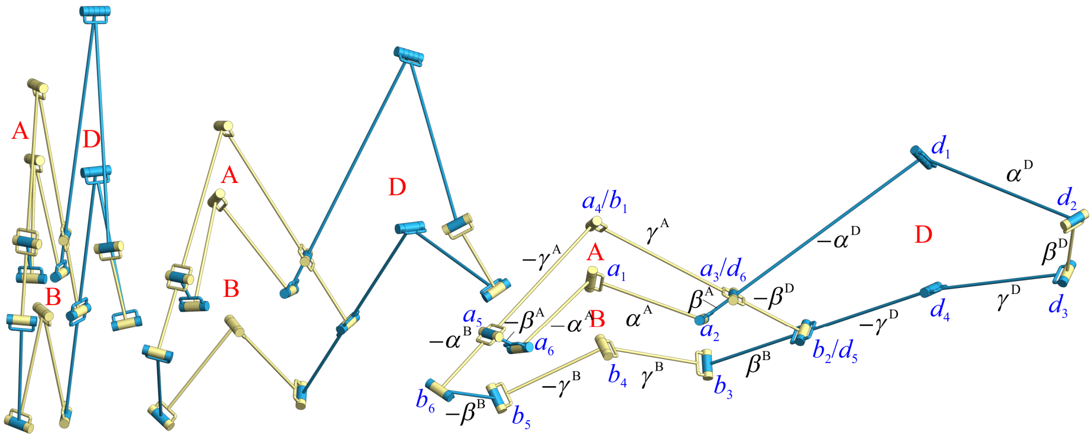

Fig. 3-11 The motion sequence of a model of motion type AI-BII-DII according to the Eq. (3-38b).

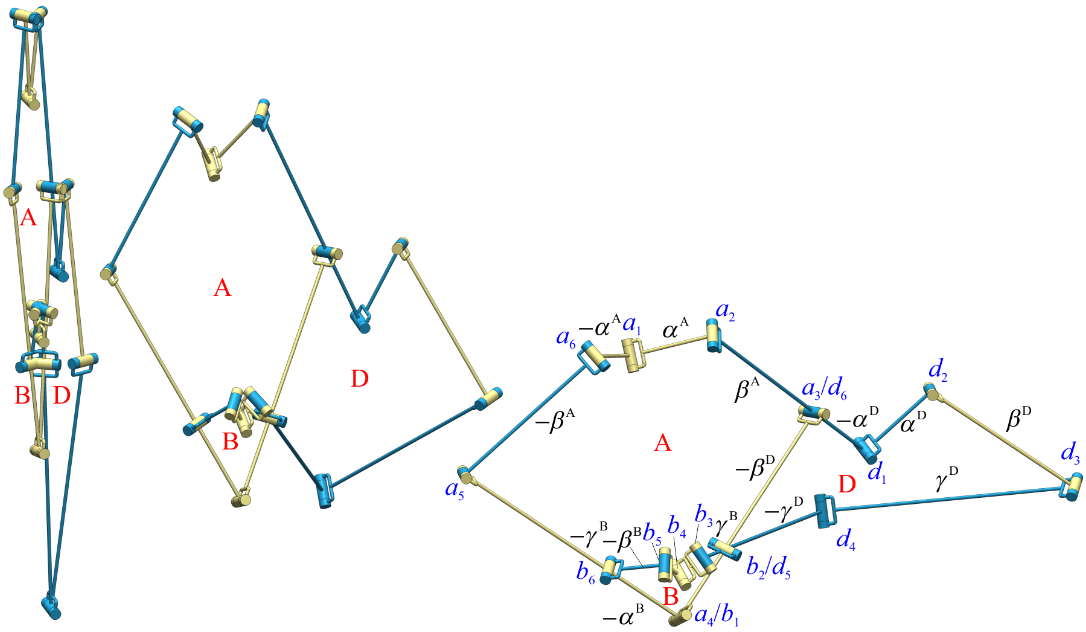

Fig. 3-12 The motion sequence of a model of motion type AI-BII-DII according to the Eq. (3-38c).

For the motion type AII-BI-DII, we have

$$
\begin{aligned}
&\alpha^{\mathrm{B}}=\alpha^{\mathrm{D}}-\gamma^{\mathrm{D}}+\gamma^{\mathrm{A}},\ \beta^{\mathrm{K}}=\alpha^{\mathrm{K}}-\gamma^{\mathrm{K}},\\
&w^{\mathrm{A}}=\lambda^{\mathrm{A}}u^{\mathrm{A}},\ w^{\mathrm{D}}=\lambda^{\mathrm{D}}u^{\mathrm{D}},\\
&u^{\mathrm{B}}=w^{\mathrm{A}}+u^{\mathrm{D}}-w^{\mathrm{D}},\ v^{\mathrm{K}}=w^{\mathrm{K}}-u^{\mathrm{K}},
\end{aligned}
\tag{3-39}
$$

where λ^{A} and λ^{D} have three special cases, as

$$
\lambda^{\mathrm{A}}=1-\mathrm{c}\gamma^{\mathrm{A}}+\frac{\mathrm{s}\gamma^{\mathrm{A}}}{\mathrm{t}\alpha^{\mathrm{A}}},\ \lambda^{\mathrm{D}}=\frac{\mathrm{c}\left(\alpha^{\mathrm{A}}-\gamma^{\mathrm{A}}\right)\mathrm{c}\dfrac{\gamma^{\mathrm{A}}}{2}\mathrm{s}\gamma^{\mathrm{D}}}{\mathrm{c}\left(\alpha^{\mathrm{D}}-\gamma^{\mathrm{D}}+\gamma^{\mathrm{A}}\right)\mathrm{c}\left(\alpha^{\mathrm{A}}-\dfrac{\gamma^{\mathrm{A}}}{2}\right)\mathrm{s}\alpha^{\mathrm{D}}},
\tag{3-40a}
$$

$$
\begin{aligned}
&\lambda^{\mathrm{A}}=1+\mathrm{c}\gamma^{\mathrm{A}}-\frac{\mathrm{s}\gamma^{\mathrm{A}}}{\mathrm{t}\alpha^{\mathrm{A}}},\\
&\lambda^{\mathrm{D}}=-\frac{\mathrm{c}\left(\alpha^{\mathrm{A}}-\gamma^{\mathrm{A}}\right)\mathrm{s}\dfrac{\gamma^{\mathrm{A}}}{2}\mathrm{s}\gamma^{\mathrm{D}}}{\mathrm{c}\left(\alpha^{\mathrm{D}}-\gamma^{\mathrm{D}}+\gamma^{\mathrm{A}}\right)\mathrm{s}\left(\alpha^{\mathrm{A}}-\dfrac{\gamma^{\mathrm{A}}}{2}\right)\mathrm{s}\alpha^{\mathrm{D}}},
\end{aligned}
\tag{3-40b}
$$

$$
\begin{aligned}
&\lambda^{\mathrm{A}}=\frac{\mathrm{t}\gamma^{\mathrm{A}}}{\mathrm{t}\alpha^{\mathrm{A}}},\\
&\lambda^{\mathrm{D}}=\frac{\mathrm{c}\gamma^{\mathrm{A}}\mathrm{s}\gamma^{\mathrm{D}}}{\mathrm{c}\left(\alpha^{\mathrm{D}}-\gamma^{\mathrm{D}}+\gamma^{\mathrm{A}}\right)\mathrm{s}\alpha^{\mathrm{D}}}.
\end{aligned}
\tag{3-40c}
$$

Models of motion type AII-BI-DII are constructed with the parameters in Eqs. (3-41a) to (3-41c), as shown in Fig. 3-13 to Fig. 3-15.

$$
\begin{aligned}
&\alpha^{\mathrm{A}}=30°,\ \beta^{\mathrm{A}}=-30°,\ \gamma^{\mathrm{A}}=60°,\ u^{\mathrm{A}}=4,\ \lambda^{\mathrm{A}}=2,\\
&\alpha^{\mathrm{B}}=30°,\ \beta^{\mathrm{B}}=-15°,\ \gamma^{\mathrm{B}}=45°,\ u^{\mathrm{B}}=6,\ w^{\mathrm{B}}=10,\\
&\alpha^{\mathrm{D}}=30°,\ \beta^{\mathrm{D}}=-30°,\ \gamma^{\mathrm{D}}=60°,\ u^{\mathrm{D}}=4,\ \lambda^{\mathrm{D}}=3/2.
\end{aligned}
\tag{3-41a}
$$

$$
\begin{aligned}
&\alpha^{\mathrm{A}}=-30°,\ \beta^{\mathrm{A}}=-150°,\ \gamma^{\mathrm{A}}=120°,\ u^{\mathrm{A}}=4,\ \lambda^{\mathrm{A}}=2,\\
&\alpha^{\mathrm{B}}=-30°,\ \beta^{\mathrm{B}}=-60°,\ \gamma^{\mathrm{B}}=30°,\ u^{\mathrm{B}}=10,\ w^{\mathrm{B}}=16,\\
&\alpha^{\mathrm{D}}=-120°,\ \beta^{\mathrm{D}}=150°,\ \gamma^{\mathrm{D}}=30°,\ u^{\mathrm{D}}=4,\ \lambda^{\mathrm{D}}=1/2.
\end{aligned}
\tag{3-41b}
$$

$$
\begin{aligned}
&\alpha^{\mathrm{A}}=-30°,\ \beta^{\mathrm{A}}=-150°,\ \gamma^{\mathrm{A}}=120°,\ u^{\mathrm{A}}=4,\ \lambda^{\mathrm{A}}=3,\\
&\alpha^{\mathrm{B}}=-30°,\ \beta^{\mathrm{B}}=-60°,\ \gamma^{\mathrm{B}}=30°,\ u^{\mathrm{B}}=44/3,\ w^{\mathrm{B}}=16,\\
&\alpha^{\mathrm{D}}=-120°,\ \beta^{\mathrm{D}}=150°,\ \gamma^{\mathrm{D}}=30°,\ u^{\mathrm{D}}=4,\ \lambda^{\mathrm{D}}=1/3.
\end{aligned}
\tag{3-41c}
$$

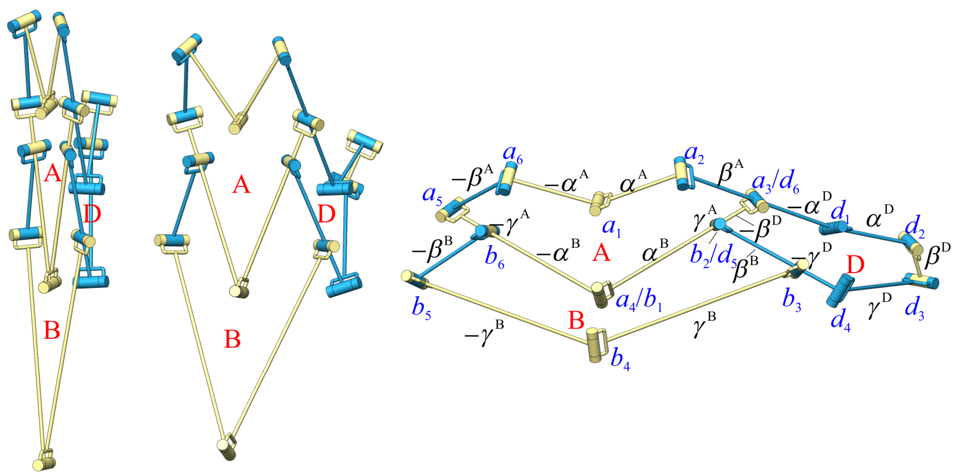

Fig. 3-13 The motion sequence of a model of motion type AII-BI-DII according to the Eq. (3-41a).

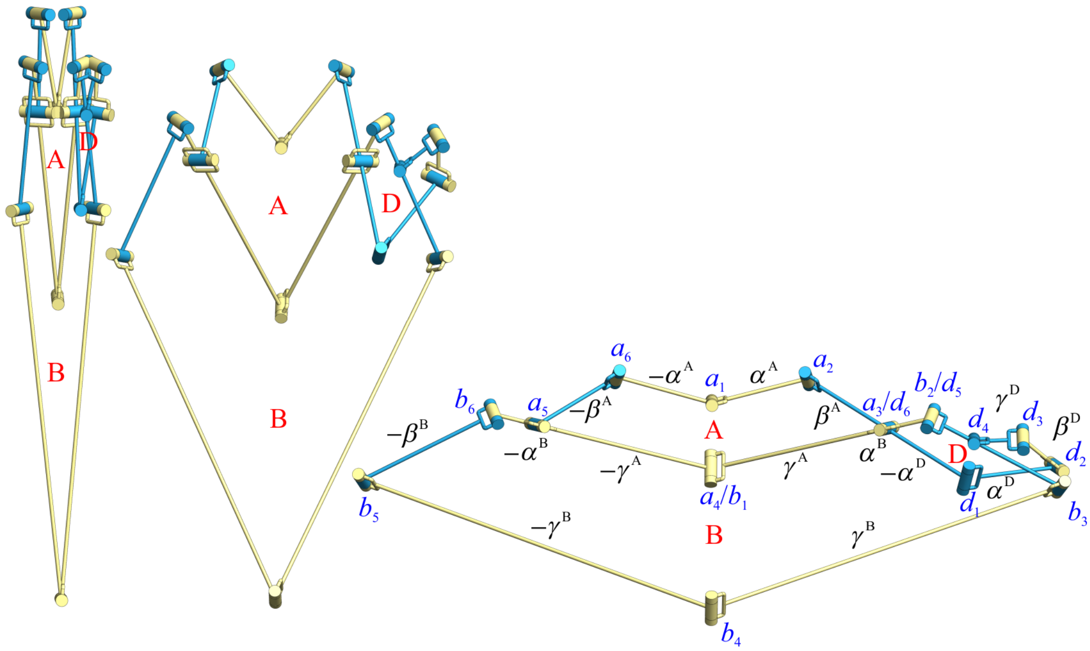

Fig. 3-14 The motion sequence of a model of motion type AII-BI-DII according to the Eq. (3-41b).

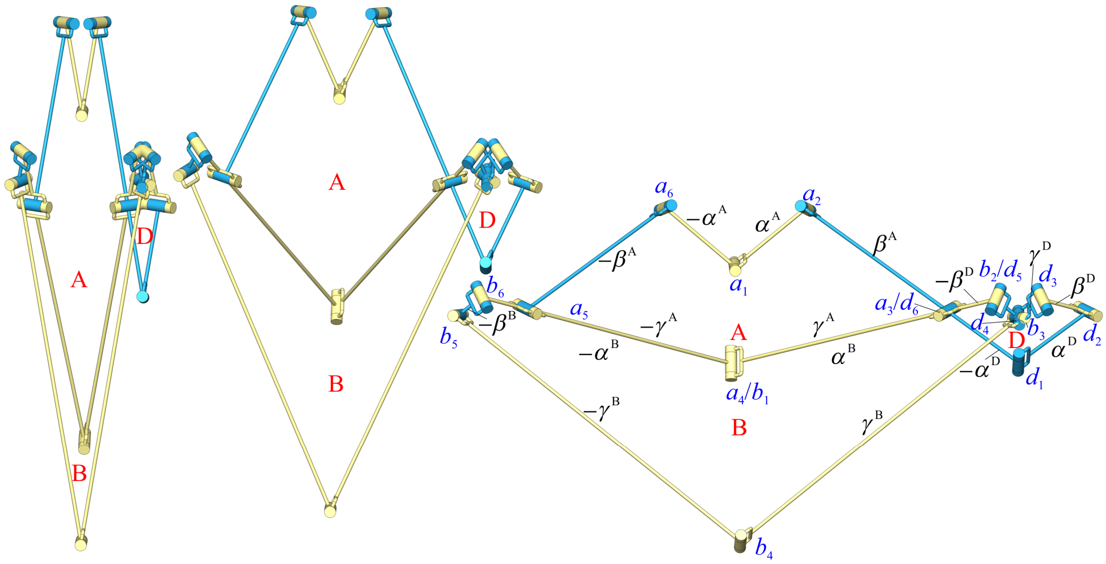

Fig. 3-15 The motion sequence of a model of motion type AII-BI-DII according to the Eq. (3-41c).

For the motion type AII-BII-DI, we have two special solutions, as

$$
\begin{aligned}
&\alpha^{\mathrm{D}}=-\gamma^{\mathrm{D}}=\alpha^{\mathrm{B}}=-\gamma^{\mathrm{A}},\ \gamma^{\mathrm{B}}=-\alpha^{\mathrm{A}},\ \alpha^{\mathrm{K}}=\beta^{\mathrm{K}}+\gamma^{\mathrm{K}},\\
&u^{\mathrm{B}}=w^{\mathrm{A}}+u^{\mathrm{D}}-w^{\mathrm{D}},\ v^{\mathrm{K}}=w^{\mathrm{K}}-u^{\mathrm{K}},\ \lambda^{\mathrm{B}}=\frac{1}{\lambda^{\mathrm{A}}},
\end{aligned}
\tag{3-42a}
$$

and

$$\alpha^{\mathrm{D}} = \gamma^{\mathrm{D}},\ \alpha^{\mathrm{B}} = \gamma^{\mathrm{A}},\ \gamma^{\mathrm{B}} = \alpha^{\mathrm{A}},\ \alpha^{\mathrm{K}} = \beta^{\mathrm{K}} + \gamma^{\mathrm{K}},$$
$$u^{\mathrm{B}} = w^{\mathrm{A}} + u^{\mathrm{D}} - w^{\mathrm{D}},\ v^{\mathrm{K}} = w^{\mathrm{K}} - u^{\mathrm{K}},\ \lambda^{\mathrm{B}} = \frac{1}{\lambda^{\mathrm{A}}}. \tag{3-42b}$$

As the parameters in Eqs. (3-43a) and (3-43b) satisfy Eqs. (3-42a) and (3-42b), respectively, two models of motion type AII-BII-DI are constructed, as shown in Fig. 3-16 and Fig. 3-17.

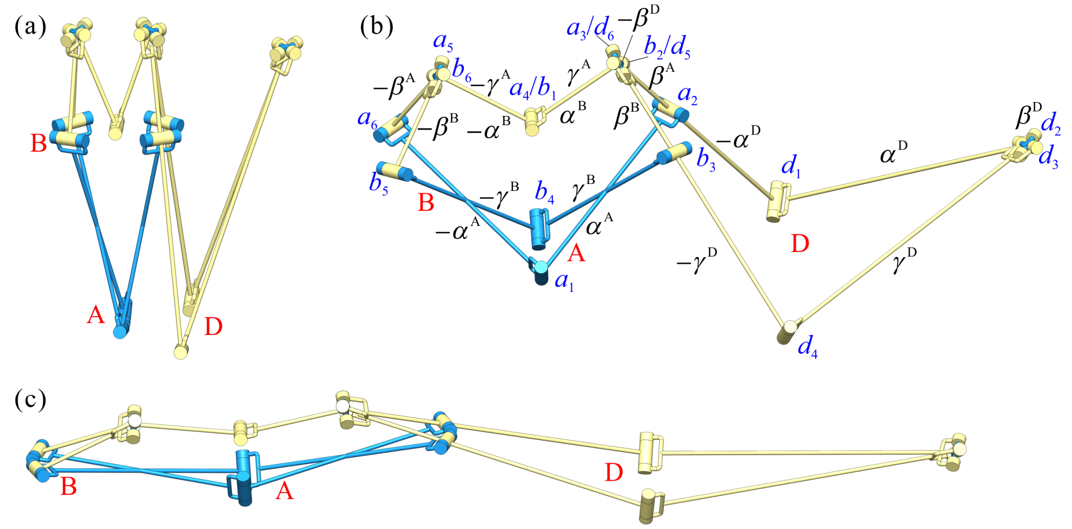

Fig. 3-16 (a)-(c) The motion sequence of a model of motion type AII-BII-DI according to Eq. (3-43a).

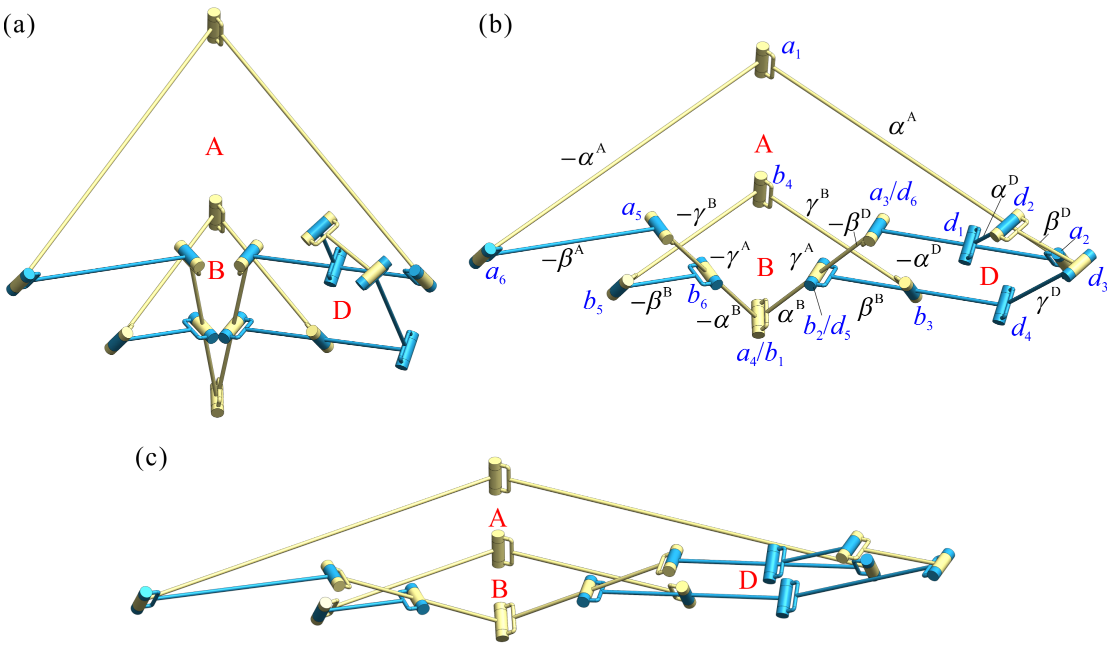

Fig. 3-17 (a)-(c) The motion sequence of a model of motion type AII-BII-DI according to Eq. (3-43b).

$$\begin{aligned}
&\alpha^{\mathrm{A}}=-120°,\ \beta^{\mathrm{A}}=150°,\ \gamma^{\mathrm{A}}=30°,\ u^{\mathrm{A}}=8,\ \lambda^{\mathrm{A}}=1/2,\\
&\alpha^{\mathrm{B}}=-30°,\ \beta^{\mathrm{B}}=-150°,\ \gamma^{\mathrm{B}}=120°,\ u^{\mathrm{B}}=4,\ \lambda^{\mathrm{B}}=2,\\
&\alpha^{\mathrm{D}}=-30°,\ \beta^{\mathrm{D}}=-60°,\ \gamma^{\mathrm{D}}=30°,\ u^{\mathrm{D}}=12,\ w^{\mathrm{D}}=12.
\end{aligned} \tag{3-43a}$$

$$\begin{aligned}
&\alpha^{\mathrm{A}}=30°,\ \beta^{\mathrm{A}}=-60°,\ \gamma^{\mathrm{A}}=-30°,\ u^{\mathrm{A}}=16,\ \lambda^{\mathrm{A}}=1/2,\\
&\alpha^{\mathrm{B}}=-30°,\ \beta^{\mathrm{B}}=-60°,\ \gamma^{\mathrm{B}}=30°,\ u^{\mathrm{B}}=4,\ \lambda^{\mathrm{B}}=2,\\
&\alpha^{\mathrm{D}}=-30°,\ \beta^{\mathrm{D}}=0°,\ \gamma^{\mathrm{D}}=-30°,\ u^{\mathrm{D}}=4,\ w^{\mathrm{D}}=8.
\end{aligned} \tag{3-43b}$$

For the motion type AII-BII-DII, we get solutions which are the special cases of AI-BI-DI, as

$$\begin{aligned}
&\alpha^{\mathrm{D}}=-\gamma^{\mathrm{A}},\ \gamma^{\mathrm{D}}=-\alpha^{\mathrm{B}},\ \alpha^{\mathrm{K}}=\beta^{\mathrm{K}}+\gamma^{\mathrm{K}},\\
&u^{\mathrm{B}}=w^{\mathrm{A}}+u^{\mathrm{D}}-w^{\mathrm{D}},\ v^{\mathrm{K}}=w^{\mathrm{K}}-u^{\mathrm{K}},\\
&\lambda^{\mathrm{K}}=\frac{w^{\mathrm{K}}}{u^{\mathrm{K}}}=\frac{\mathrm{t}\gamma^{\mathrm{K}}}{\mathrm{t}\alpha^{\mathrm{K}}},
\end{aligned} \tag{3-44a}$$

and

$$\begin{aligned}
&\alpha^{\mathrm{D}}=\gamma^{\mathrm{D}},\ \alpha^{\mathrm{B}}=\gamma^{\mathrm{A}},\ \alpha^{\mathrm{K}}=\beta^{\mathrm{K}}+\gamma^{\mathrm{K}},\\
&u^{\mathrm{B}}=w^{\mathrm{A}}+u^{\mathrm{D}}-w^{\mathrm{D}},\ v^{\mathrm{K}}=w^{\mathrm{K}}-u^{\mathrm{K}},\\
&\lambda^{\mathrm{K}}=\frac{w^{\mathrm{K}}}{u^{\mathrm{K}}}=\frac{\mathrm{t}\gamma^{\mathrm{K}}}{\mathrm{t}\alpha^{\mathrm{K}}}.
\end{aligned} \tag{3-44b}$$

From the eight motion types, we find five types are different, i.e., AI-BI-DI, AI-BI-DII, AI-BII-DII, AII-BI-DII, AII-BII-DI. Compatibility condition of a mobile assembly can be derived from the combination of compatibility conditions on all links under the selected motion types.

3.6 Conclusions

In this chapter, the mobile assemblies of plane-symmetric Bricard linkages have been constructed from the diamond thick-panel origami based on their kinematic equivalence. The compatibility analysis on the diamond assembly extends the construct condition of the two newly-found mobile assemblies of plane-symmetric Bricard linkages with X-guidelines and Y-guidelines. By transferring the general construct condition of mobile assemblies back to diamond thick-panel origami, thickness and sector angles of diamond thick-panel origami can be varied according to the condition of case II assembly. Then a diamond thick-panel origami with flat unfolded profiles and a graded diamond thick-panel origami pattern with spirally folded configuration are inspired from the case II assembly. The graded diamond thick-panel origami pattern is more potential in engineering applications, such as solar panels.

Chapter 4 Vertex-Splitting on Rigid Origami

4.1 Introduction

There are many multi-DOF rigid origami patterns which have large potentials in engineering applications. Yet it is generally difficult to fully control the motion in the desired manner. In this chapter, a vertex-splitting technique is proposed to reduce the DOF of diamond origami pattern and obtain one-DOF origami patterns with kinematic equivalence. As some applications are sensitive to the flat unfolded state, the relationship between variations of the mobile assembly of two Bennett linkages and that of corresponding thick-panel origami will be studied to construct thick-panel origami patterns with flat-surface unfolded profiles by removing some hinges.

The layout of the chapter is as follows. Two vertex-splitting schemes are proposed on the diamond vertex and generate three types of unit patterns in section 4.2 with analysis of their kinematic behaviours. The technique is applied to the multi-vertex diamond origami pattern to produce one-DOF basic assemblies and one-DOF origami patterns in section 4.3. Hinge-removing is proposed by analysing relationships between the construction of Waldron's hybrid 6*R* linkage from the assembly of two Bennett linkages and the variation of their corresponding thick-panel origami pattern, which is applied to construct thick-panel origami with flat unfolded profiles in section 4.4. Finally, conclusions are drawn in section 4.5.

4.2 Vertex-Splitting on the Diamond Vertex

A diamond vertex has six creases meeting at one point, as shown in Fig. 4-1. z_i ($i = 1, 2, 3, 4, 5, 6$) are axes of the six creases and $\alpha_{i(i+1)}$ are sector angles with the geometric conditions

$$\begin{aligned}&\alpha_{12} = \alpha_{61} = \alpha,\\&\alpha_{23} = \alpha_{56} = \pi - 2\alpha,\\&\alpha_{34} = \alpha_{45} = \alpha,\end{aligned} \tag{4-1}$$

where $0 < \alpha \le \pi/4$, to ensure flat foldability. θ_i^{A} represent angles of rotation between two panels joined by a crease and φ_i^{A} represent dihedral angle between two panels joined by a crease. Taking creases and rigid panels as revolute joints and links, respectively, the diamond vertex can be considered as a spherical 6*R* linkage with three DOFs.

Imposing the line- and plane-symmetric conditions to the diamond vertex in Fig. 4-1, i.e. $\theta_1^{\mathrm{A}} = \theta_4^{\mathrm{A}}$ and $\theta_2^{\mathrm{A}} = \theta_3^{\mathrm{A}} = \theta_5^{\mathrm{A}} = \theta_6^{\mathrm{A}}$ [133], the kinematic equations of spherical 6*R* linkage can be derived from matrix method in section 1.2.1.1, as

$$\tan\frac{\theta_1^{\mathrm{A}}}{2} = -\cos\alpha\tan\frac{\theta_2^{\mathrm{A}}}{2},\ \theta_1^{\mathrm{A}} = \theta_4^{\mathrm{A}},\ \theta_2^{\mathrm{A}} = \theta_3^{\mathrm{A}} = \theta_5^{\mathrm{A}} = \theta_6^{\mathrm{A}}, \tag{4-2}$$

in which θ_i^{A} is the kinematic variables set up with D-H notation. In origami study, dihedral angles φ_i^{A} are preferred to have a direct presentation of the folding process. The dihedral angles and kinematic variables have the following relationship [42],

$$\begin{aligned} &\theta_1^{\mathrm{A}} = \pi - \varphi_1^{\mathrm{A}},\ \theta_2^{\mathrm{A}} = \pi + \varphi_2^{\mathrm{A}},\ \theta_3^{\mathrm{A}} = \pi + \varphi_3^{\mathrm{A}}, \\ &\theta_4^{\mathrm{A}} = \pi - \varphi_4^{\mathrm{A}},\ \theta_5^{\mathrm{A}} = \pi + \varphi_5^{\mathrm{A}},\ \theta_6^{\mathrm{A}} = \pi + \varphi_6^{\mathrm{A}}, \end{aligned} \tag{4-3}$$

Eq. (4-2) becomes

$$\tan\frac{\varphi_1^{\mathrm{A}}}{2} = \frac{1}{\cos\alpha}\tan\frac{\varphi_2^{\mathrm{A}}}{2},\ \varphi_1^{\mathrm{A}} = \varphi_4^{\mathrm{A}},\ \varphi_2^{\mathrm{A}} = \varphi_3^{\mathrm{A}} = \varphi_5^{\mathrm{A}} = \varphi_6^{\mathrm{A}}. \tag{4-4}$$

Hence, the diamond vertex exhibits one-DOF in symmetric folding, whose motion is shown in Fig. 4-2.

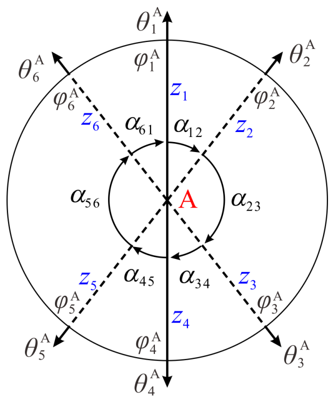

Fig. 4-1 A diamond vertex.

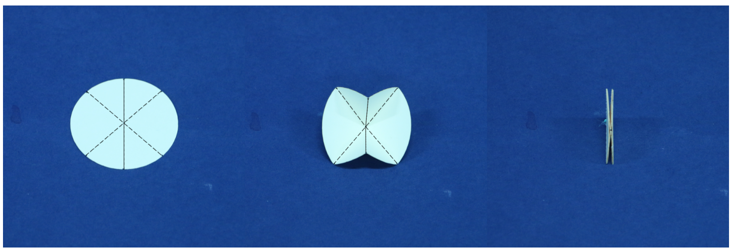

Fig. 4-2 The motion sequence of diamond vertex in symmetric folding.

As the diamond vertex is plane-symmetric about the central creases a_1 and a_4 (Fig. 4-3a), two vertex-splitting schemes are proposed, SI is splitting towards the direction parallel to the central creases to get pattern DI and SII is towards the direction perpendicular to the central creases to obtain pattern DII, see Fig. 4-3(b) and (c). Two schemes acting on the diamond vertex at the same time produce pattern DI-II in Fig. 4-3(d).

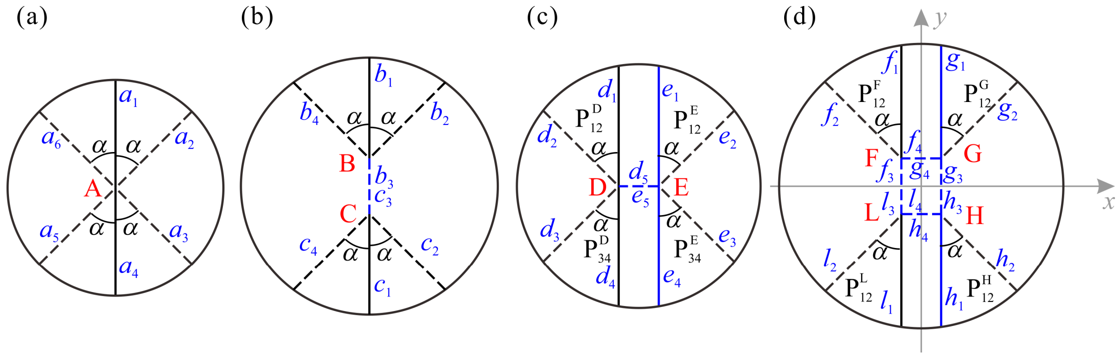

Fig. 4-3 The crease patterns of a diamond vertex and its corresponding patterns by splitting vertices. (a) Diamond vertex; (b) pattern DI, (c) pattern DII and (d) pattern DI-II. Here, the blue lines represent the added creases for splitting the vertex.

Pattern DI (Fig. 4-3(b)) consists of two four-crease vertices B and C, which can be regarded as two spherical 4R linkages connected in series with one DOF. The kinematic equations of spherical 4R linkages B and C can be derived, as

$$\tan\frac{\varphi_1^{\mathrm{B}}}{2}=\frac{1}{\cos\alpha}\tan\frac{\varphi_2^{\mathrm{B}}}{2},\ \ \varphi_1^{\mathrm{B}}=\varphi_3^{\mathrm{B}},\ \ \varphi_2^{\mathrm{B}}=\varphi_4^{\mathrm{B}}, \tag{4-5a}$$

$$\tan\frac{\varphi_1^{\mathrm{C}}}{2}=\frac{1}{\cos\alpha}\tan\frac{\varphi_2^{\mathrm{C}}}{2},\ \ \varphi_1^{\mathrm{C}}=\varphi_3^{\mathrm{C}},\ \ \varphi_2^{\mathrm{C}}=\varphi_4^{\mathrm{C}}. \tag{4-5b}$$

The shared crease b_3/c_3 satisfies angular relation $\varphi_3^{\mathrm{B}}=\varphi_3^{\mathrm{C}}$. When giving an input dihedral angle, all the other angles will be determined, according to Eqs. (4-5a) and (4-5b). For the original diamond vertex in Fig. 4-3(a) and pattern DI in Fig. 4-3(b), setting input $\varphi_2^{\mathrm{A}}=\varphi_2^{\mathrm{B}}$, from Eqs. (4-4), (4-5a) and (4-5b), the relationship of the other dihedral angles can be obtained as

$$\varphi_3^{\mathrm{A}}=\varphi_5^{\mathrm{A}}=\varphi_6^{\mathrm{A}}=\varphi_4^{\mathrm{B}}=\varphi_2^{\mathrm{C}}=\varphi_4^{\mathrm{C}}, \tag{4-6a}$$

$$\varphi_1^{\mathrm{A}}=\varphi_4^{\mathrm{A}}=\varphi_1^{\mathrm{B}}=\varphi_1^{\mathrm{C}}. \tag{4-6b}$$

Hence, pattern DI is kinematically equivalent to the original diamond vertex in line- and plane-symmetric conditions. It is flat-foldable, whose motion sequence is shown in Fig. 4-4.

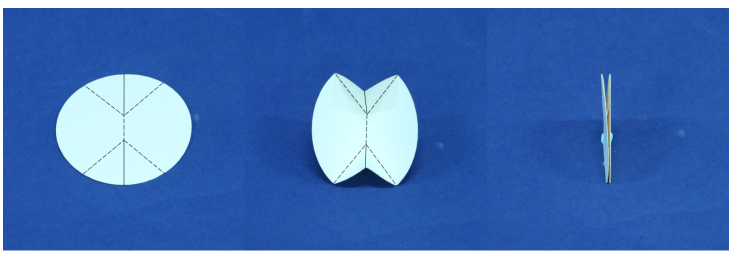

Fig. 4-4 The motion sequence of pattern DI.

Pattern DII (Fig. 4-3(c)) has two five-crease vertices with shared crease d_5/e_5. As each five-crease vertex has two DOFs, this pattern has multiple DOFs. As each vertex is plane-symmetric about crease d_5/e_5, symmetric folding of each vertex is allowed by introducing symmetric conditions of dihedral angles, i.e., $\varphi_3^{\mathrm{D/E}}=\varphi_2^{\mathrm{D/E}}$, $\varphi_4^{\mathrm{D/E}}=\varphi_1^{\mathrm{D/E}}$ to vertices D and E. The following kinematic equations are obtained.

$$\tan\varphi_1^{\mathrm{D}}=-\cos\alpha\cot\frac{\varphi_2^{\mathrm{D}}}{2},\ \varphi_3^{\mathrm{D}}=\varphi_2^{\mathrm{D}},\ \varphi_4^{\mathrm{D}}=\varphi_1^{\mathrm{D}},$$
$$\cos\varphi_5^{\mathrm{D}}=8\sin^2\alpha-8\sin^4\alpha-8\sin^2\alpha\sin^2\frac{\varphi_2^{\mathrm{D}}}{2}+8\sin^4\alpha\sin^2\frac{\varphi_2^{\mathrm{D}}}{2}+2\sin^4\alpha\sin^2\frac{\varphi_2^{\mathrm{D}}}{2}-1,\tag{4-7a}$$

$$\tan\varphi_1^{\mathrm{E}}=-\cos\alpha\cot\frac{\varphi_2^{\mathrm{E}}}{2},\ \varphi_3^{\mathrm{E}}=\varphi_2^{\mathrm{E}},\ \varphi_4^{\mathrm{E}}=\varphi_1^{\mathrm{E}},$$
$$\cos\varphi_5^{\mathrm{E}}=8\sin^2\alpha-8\sin^4\alpha-8\sin^2\alpha\sin^2\frac{\varphi_2^{\mathrm{E}}}{2}+8\sin^4\alpha\sin^2\frac{\varphi_2^{\mathrm{E}}}{2}+2\sin^4\alpha\sin^2\frac{\varphi_2^{\mathrm{E}}}{2}-1.\tag{4-7b}$$

With $\varphi_5^{\mathrm{D}}=\varphi_5^{\mathrm{E}}$ at the shared crease d_5/e_5, one input dihedral angle will determine the configuration of pattern DII in symmetric conditions, i.e., it has one-DOF. Taking $\varphi_2^{\mathrm{A}}=\varphi_2^{\mathrm{D}}$ into Eqs. (4-4), (4-7a) and (4-7b), we obtain

$$\varphi_3^{\mathrm{A}}=\varphi_5^{\mathrm{A}}=\varphi_6^{\mathrm{A}}=\varphi_2^{\mathrm{D}}=\varphi_3^{\mathrm{D}}=\varphi_2^{\mathrm{E}}=\varphi_3^{\mathrm{E}},\tag{4-8a}$$
$$\varphi_1^{\mathrm{A}}=\varphi_4^{\mathrm{A}}=2\left(\varphi_1^{\mathrm{D}}-\pi/2\right)=2\left(\varphi_4^{\mathrm{D}}-\pi/2\right)=2\left(\varphi_1^{\mathrm{E}}-\pi/2\right)=2\left(\varphi_4^{\mathrm{E}}-\pi/2\right).\tag{4-8b}$$

Thus, the dihedral angles of the valley creases d_2, d_3, e_2, e_3 are equal to that of creases a_2, a_3, a_5, a_6 in diamond vertex. The dihedral angles between the panels P1 $\mathrm{P}_{12}^{\mathrm{D}}$ and $\mathrm{P}_{12}^{\mathrm{E}}$, the panels $\mathrm{P}_{34}^{\mathrm{D}}$ and $\mathrm{P}_{34}^{\mathrm{E}}$ in Fig. 4-3(d) are equal to φ_1^{A}. This also indicates pattern DII is kinematically equivalent to diamond vertex which is under line- and plane-symmetric conditions. Its motion sequence is shown in Fig. 4-5. It should be noted that pattern DII loses flat-foldability due to the five-crease vertex.

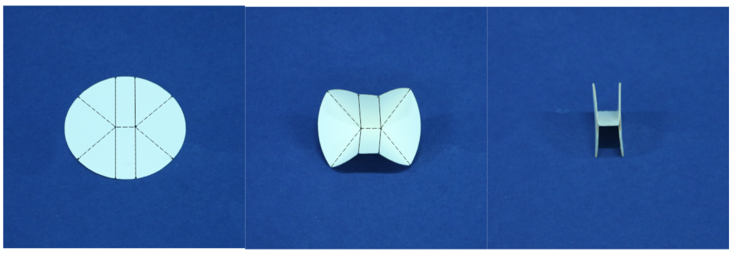

Fig. 4-5 The motion sequence of pattern DII in symmetric conditions.

Applying the two above-introduced vertex-splitting methods to the diamond vertex at the same time, a plane-symmetric pattern DI-II, with four four-crease origami vertices is constructed, as shown in Fig. 4-3(d). Based on the truss method [44], we first trim the edge facets to triangular or quadrilateral shapes, as shown in Fig. 4-6(a). The pattern is then converted to a truss form by replacing creases with bars and vertices by nodes. For triangular facets, three bars will make a facet rigid; for quadrilateral facets, an arbitrary point out of the facets can be introduced to generate the truss form, such as the facet GHV_5V_4 in Fig. 4-6(a) to tetrahedrons W_2GHV_4 and $W_2HV_5V_4$ in Fig. 4-6(b).

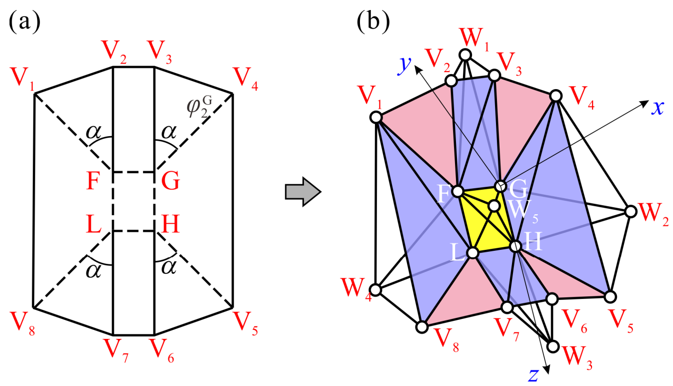

Fig. 4-6 Pattern DI-II. (a) pattern DI-II with the edge facets trimmed to triangular or quadrilateral shapes; (b) the corresponding truss form. Here, the origin of the Cartesian coordinate system is a node G, the *z*-axis is along the direction of the bar GH, the *x*-axis is perpendicular to *z*-axis on the plane GHV_5V_4 and *y*-axis is determined by the right-hand rule.

By counting, the truss form of pattern DI-II in Fig. 4-6(b) contains $j = 17$ nodes, $b = 45$ bars. When taking $\alpha = 45°$ and $\varphi_2^G = 120°$ in pattern DI-II, the coordinate of nodes can be obtained as expressed in Eq. (4-9a) in a Cartesian coordinate system noted in Fig. 4-6(b). The equilibrium matrix of pattern DI-II can be established according to [44]. Then, the rank of the matrix $r = 44$ is obtained. The numbers of self-stresses and mobility in pattern DI-II are $s = 1$, $m = 1$ derived from Eqs. (1-10) and (1-11). Hence, the pattern DI-II is overconstrained with one-DOF.

$$\begin{aligned}
\boldsymbol{W}_1 &= [2.99482507,\ 60.25081951,\ -19.17794444]^{\mathrm{T}}, \\
\boldsymbol{W}_2 &= [35.35533906,\ -35.35533906,\ 0]^{\mathrm{T}}, \\
\boldsymbol{W}_3 &= [-14.01357621,\ 18.58891502,\ 88.86421410\ ]^{\mathrm{T}}, \\
\boldsymbol{W}_4 &= [-68.51379857,\ 7.04905881,\ 0\ ]^{\mathrm{T}}, \\
\boldsymbol{W}_5 &= [-7.17746781,\ 35.33389245,\ 10\ ]^{\mathrm{T}},
\end{aligned} \tag{4-9a}$$

$$\begin{aligned}
&\boldsymbol{F}=[-18.51640200,\ 7.55928946,\ 0]^{\mathrm{T}},\ \boldsymbol{G}=[0,\ 0,\ 0]^{\mathrm{T}},\ \boldsymbol{H}=[0,\ 0,\ 30]^{\mathrm{T}},\\
&\boldsymbol{L}=[-18.51640200,\ 7.55928946,\ 30]^{\mathrm{T}},\\
&\boldsymbol{V}_1=[-43.77021561,\ 32.30287243,\ -35.35533906]^{\mathrm{T}},\\
&\boldsymbol{V}_2=[-5.50937557,\ 39.41986727,\ -39.02107927]^{\mathrm{T}},\\
&\boldsymbol{V}_3=[13.00702642,\ 31.86057781,\ -39.02107927]^{\mathrm{T}},\\
&\boldsymbol{V}_4=[35.35533906,\ 0,\ -35.35533906]^{\mathrm{T}},\\
&\boldsymbol{V}_5=[35.35533906,\ 0,\ 65.35533906]^{\mathrm{T}},\\
&\boldsymbol{V}_6=[13.00702642,\ 31.86057781,\ 69.02107927]^{\mathrm{T}},\\
&\boldsymbol{V}_7=[-5.50937557,\ 39.41986727,\ 69.02107927]^{\mathrm{T}},\\
&\boldsymbol{V}_8=[-43.77021561,\ 32.30287243,\ 65.35533906]^{\mathrm{T}}.
\end{aligned}\tag{4-9b}$$

With the symmetric condition that linkages F, G, H, L are symmetric about x-axis and y-axis, these vertices have equivalent motions, as follows

$$\begin{aligned}
&\tan\varphi_1^i=-\cos\alpha\cot\frac{\varphi_2^i}{2},\\
&\sin\varphi_3^i=\cos\varphi_2^i\sin\varphi_1^i-\cos\alpha\sin\varphi_1^i\sin\varphi_2^i,\\
&\cos\varphi_4^i=2\sin^2\alpha\cos^2\frac{\varphi_2^i}{2}-1,\\
&i=\mathrm{F},\ \mathrm{G},\ \mathrm{H},\ \mathrm{L}.
\end{aligned}\tag{4-10}$$

Because of the dihedral angles satisfying

$$\varphi_4^{\mathrm{F}}=\varphi_4^{\mathrm{G}},\ \varphi_3^{\mathrm{G}}=\varphi_3^{\mathrm{H}},\ \varphi_4^{\mathrm{L}}=\varphi_4^{\mathrm{H}},\ \varphi_3^{\mathrm{F}}=\varphi_3^{\mathrm{L}}.\tag{4-11}$$

Taking $\varphi_2^{\mathrm{A}}=\varphi_2^{\mathrm{G}}$ into Eqs. (4-4), (4-10) and (4-11), we can obtain

$$\begin{aligned}
&\varphi_3^{\mathrm{A}}=\varphi_5^{\mathrm{A}}=\varphi_6^{\mathrm{A}}=\varphi_2^{\mathrm{F}}=\varphi_2^{\mathrm{H}}=\varphi_2^{\mathrm{L}},\\
&\varphi_1^{\mathrm{A}}=\varphi_4^{\mathrm{A}}=2(\varphi_1^{\mathrm{F}}-\pi/2)=2(\varphi_1^{\mathrm{G}}-\pi/2)=2(\varphi_1^{\mathrm{H}}-\pi/2)=2(\varphi_1^{\mathrm{L}}-\pi/2).
\end{aligned}\tag{4-12}$$

Similar to patterns DI and DII, diamond vertex under line- and plane-symmetric conditions is kinematically equivalent to pattern DI-II. Because the sum of the alternate angles about each vertex is not equal to π, this pattern is non-flat-foldable [107]. The motion sequence of this pattern is shown in Fig. 4-7.

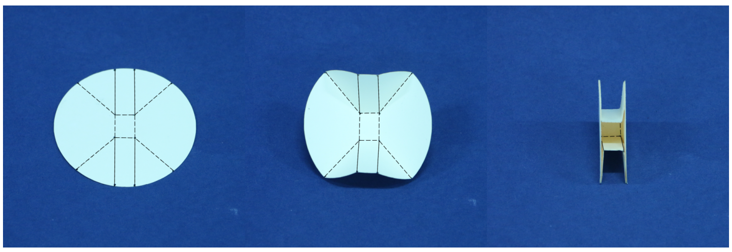

Fig. 4-7 The motion sequence of pattern DI-II.

4.3 Vertex-Splitting on Multi-Vertex Diamond Origami Pattern

A multi-DOF diamond origami pattern with six identical six-crease vertices is shown in Fig. 4-8. These vertices can be divided into four rows and three columns. Each vertex is noted A, B, C, D, E, F. According to the truss analogy, we obtain this pattern has nine DOFs with $j=18$ nodes, $b=39$ bars. Thus, the motion of this pattern is much difficult to be fully controlled. In order to maintain the symmetrically geometrical characteristics and avoid the non-rigid origami patterns, the vertices of the diamond origami pattern are split in whole row or column. SI can be applied to vertices in a whole row to produce pattern DI. Four rows generate fifteen cases of vertex-splitting SI_1 to $\mathrm{SI}_{1,2,3,4}$ in Table 4-1. Here, SI_i means applying the vertex-splitting method SI to split the vertices in rows *i* (*i*=1, 2, 3, 4). SII can be applied to vertices in a whole column, which leads to five cases SII_1 to $\mathrm{SII}_{1,2,3}$ in Table 4-1. Therefore, the mix of the two methods SI and SII can generate $5\times15=75$ cases. SI_0 and SII_0 mean no vertex-splitting on rows and columns, correspondingly. So the number of all the cases including the original one is $(5+1)\times(15+1)=96$. The corresponding origami patterns are shown in appendix A, whose DOF can be determined by the one-DOF basic assemblies in the patterns. Next, those basic assemblies of four-crease, five-crease, and/or six-crease vertices are discussed.

Basic assemblies of four-crease vertices A, B, C, D are shown in Fig. 4-9(a) to (f) which can be denoted by the diagram with quadrilateral loops of four spherical 4*R* linkages in Fig. 4-9(g). They are overconstrained with one-DOF due to the plane-symmetric conditions [104].

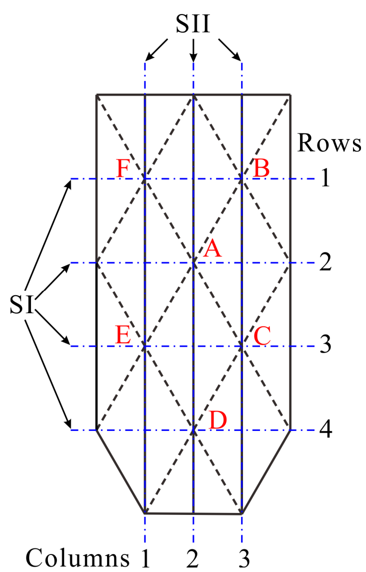

Fig. 4-8 A diamond origami pattern with six vertices.

Table 4-1 Cases of vertex-splitting on multi-vertex diamond origami pattern in Fig. 4-8

	SII_0	SII_1	SII_2	$SII_{1,3}$	$SII_{1,2}$	$SII_{1,2,3}$
SI_0	*m*	*m*	*m*	*m*	*m*	*m*
SI_1	*m*	*m*	*m*	*m*	*m*	*m*
SI_2	*m*	*m*	*m*	*m*	*m*	*m*
SI_3	*m*	*m*	*m*	*m*	*m*	*m*
SI_4	*m*	*m*	*m*	*m*	*m*	*m*
$SI_{1,2}$	*m*	*m*	*m*	1	1	1
$SI_{1,3}$	1	1	1	1	1	1
$SI_{1,4}$	*m*	*m*	*m*	1	1	1
$SI_{2,3}$	*m*	*m*	*m*	1	*m*	1
$SI_{2,4}$	*m*	*m*	*m*	*m*	*m*	*m*
$SI_{3,4}$	*m*	*m*	*m*	1	*m*	1
$SI_{1,2,3}$	1	1	1	1	1	1
$SI_{1,2,4}$	1	1	1	1	1	1
$SI_{1,3,4}$	1	1	1	1	1	1
$SI_{2,3,4}$	*m*	*m*	*m*	1	*m*	1
$SI_{1,2,3,4}$	1	1	1	1	1	1

The '*m*' means multi-DOF and '1' means one-DOF.

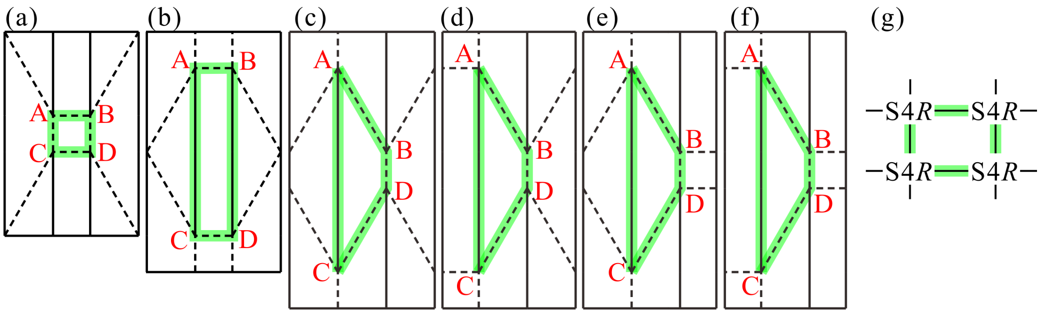

Fig. 4-9 Basic assemblies of four-crease vertices. (a)-(f) One-DOF assemblies of four crease vertices and (g) their corresponding diagram where S4*R* represents a spherical 4*R* linkage.

Basic assemblies of four-crease vertices and one five-crease vertex are shown in Fig. 4-10(a) to (d). For the pattern in Fig. 4-10(a), the motion of five-crease vertex B with two DOFs can be determined by two input dihedral angles φ_1^{B} and φ_5^{B}. The kinematic equations can be represented by

$$\varphi_2^{\mathrm{B}} = f_2^{\mathrm{B}}\left(\varphi_1^{\mathrm{B}},\ \varphi_5^{\mathrm{B}}\right),\ \varphi_3^{\mathrm{B}} = f_3^{\mathrm{B}}\left(\varphi_1^{\mathrm{B}},\ \varphi_5^{\mathrm{B}}\right),\ \varphi_4^{\mathrm{B}} = f_4^{\mathrm{B}}\left(\varphi_1^{\mathrm{B}},\ \varphi_5^{\mathrm{B}}\right), \tag{4-13}$$

where f_i^{B} represents the function to determine φ_i^{B}. From the assembly of two four-crease vertices A and C sharing a crease, we can construct a relationship between φ_1^{B} and φ_5^{B},

$$\varphi_5^{\mathrm{B}} = f_5^{\mathrm{B}}\left(\varphi_1^{\mathrm{B}}\right), \tag{4-14}$$

which give a constraint to the Eq. (4-13). So one input φ_1^{B} can determine the motion of the pattern in Fig. 4-10(a) and the pattern is one-DOF. According to the truss method, this pattern contains $j=11$ nodes and $b=26$ bars. The rank of its equilibrium matrix is $r=26$. The result $s=0$ and $m=1$ ensures that this pattern is non-overconstrained with one-DOF. Similarly, the pattern in Fig. 4-10(b) is non-overconstrained with one-DOF. For the patterns in Fig. 4-10(c) to (d), the motion of five-crease vertex can be determined by setting the dihedral angles φ_1^{D} and φ_2^{D}. As the relationship between φ_1^{D} and φ_2^{D} is constructed by the one-DOF assembly of four-crease vertices E, F and G, the motion of this pattern can be determined by giving φ_1^{D}, i.e., this pattern has one-DOF. Truss method also verifies the result. Those four patterns can be represented by the diagram of Fig. 4-10(e) which indicates that the pattern with one-DOF assembly connecting to a spherical 5*R* linkage by two creases which makes the pattern one-DOF.

The pattern in Fig. 4-10(f) contains two five-crease vertices sharing a crease. Giving angles φ_2^{N} and φ_5^{N} can determine the motion of vertex N and produce an input $\varphi_1^{\mathrm{L}}=\varphi_1^{\mathrm{N}}$ to vertex L. By introducing φ_5^{L}, the motion of vertex L can be determined. So the dihedral angles of vertices N and L can be derived by φ_2^{N}, φ_5^{N} and φ_5^{L}, that is

$$\begin{aligned}&\varphi_1^{\mathrm{N}}=\varphi_1^{\mathrm{L}}=f_1^{\mathrm{N}}\left(\varphi_2^{\mathrm{N}},\ \varphi_5^{\mathrm{N}}\right),\ \varphi_3^{\mathrm{N}}=f_3^{\mathrm{N}}\left(\varphi_2^{\mathrm{N}},\ \varphi_5^{\mathrm{N}}\right),\ \varphi_4^{\mathrm{N}}=f_4^{\mathrm{N}}\left(\varphi_2^{\mathrm{N}},\ \varphi_5^{\mathrm{N}}\right),\\&\varphi_2^{\mathrm{L}}=f_2^{\mathrm{L}}\left(\varphi_2^{\mathrm{N}},\ \varphi_5^{\mathrm{N}},\ \varphi_5^{\mathrm{L}}\right),\ \varphi_3^{\mathrm{L}}=f_3^{\mathrm{L}}\left(\varphi_2^{\mathrm{N}},\ \varphi_5^{\mathrm{N}},\ \varphi_5^{\mathrm{L}}\right),\ \varphi_4^{\mathrm{L}}=f_4^{\mathrm{L}}\left(\varphi_2^{\mathrm{N}},\ \varphi_5^{\mathrm{N}},\ \varphi_5^{\mathrm{L}}\right).\end{aligned}\tag{4-15}$$

From the two four-crease vertices H and M, we can obtain

$$\varphi_2^{\mathrm{N}}=f_2^{\mathrm{N}}\left(\varphi_5^{\mathrm{L}}\right),\ \varphi_5^{\mathrm{N}}=f_5^{\mathrm{N}}\left(\varphi_2^{\mathrm{L}}\right),\tag{4-16}$$

Combining Eqs. (4-15) and (4-16), all the dihedral angles of this pattern can be derived by giving φ_5^{L}. So this pattern is non-overconstrained with one-DOF, which is verified by the truss method. This pattern is represented by the diagram of Fig. 4-10(g).

Basic assemblies of four-crease and six-crease vertices shown in Fig. 4-11(a) to (e) are the same type which can be represented by the diagram in Fig. 4-11(f). In Fig. 4-11(a) to (c), giving one input φ_3^{A}, dihedral angles φ_4^{A} and φ_5^{A} can be derived from the one-DOF assembly of four-crease vertices B, C, D, E, F. The three angles can be inputs to determine the motion of vertex A. Similarly, giving one input, the one-DOF assemblies of four-crease vertices H, L, M, N in Fig. 4-11(d) and (e) can provide three inputs φ_5^{G}, φ_6^{G}, φ_1^{G} to determine the motion of the six-crease vertex G. So these patterns are non-overconstrained with one DOF, which are confirmed by the truss method. In Fig. 4-11(g), two constraints about the relationships of φ_2^{O} & φ_3^{O} and φ_5^{O} & φ_6^{O} derived from the one-DOF assemblies of vertices Q&R and T&S, respectively, can determine the motion of six-crease vertex O. So this pattern is non-overconstrained with one-DOF. Similarly, patterns in Fig. 4-11(h) to (i) are non-overconstrained with one-DOF, which can be represented by the diagram in Fig. 4-11(j).

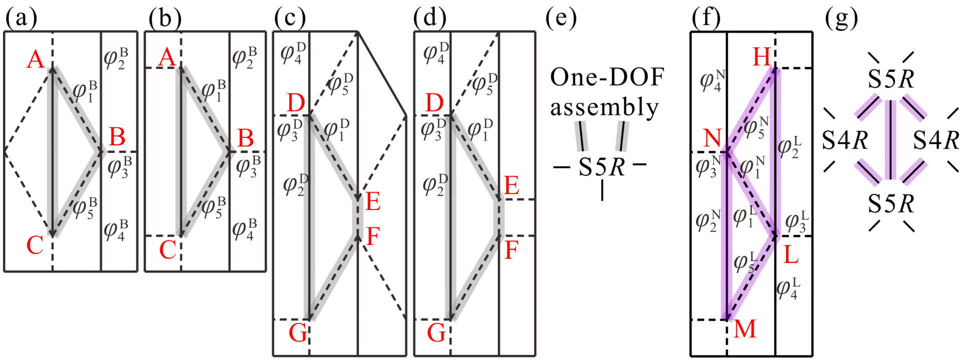

Fig. 4-10 Basic assemblies of four-crease and five-crease vertices. (a)-(d) one-DOF basic assemblies with one five-crease vertex and (e) their corresponding diagram; (f) one-DOF basic assembly with two five-crease vertices and (g) its corresponding diagram. Here, S5*R* represents a spherical 5*R* linkage.

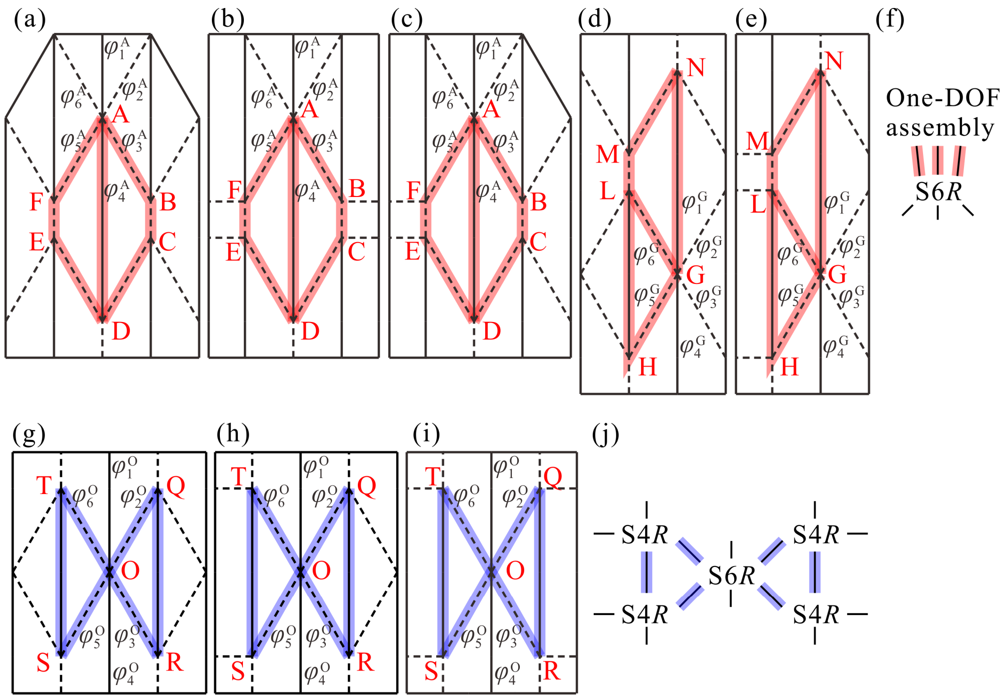

Fig. 4-11 Basic assemblies of four-crease and six-crease vertices. (a)-(e) The one-DOF basic assemblies with three creases connecting the six-crease vertex and four-crease vertices, and (f) their corresponding diagram; (g)-(i) one-DOF basic assemblies with four creases connecting the six-crease vertex and four-crease vertices and (j) their corresponding diagram. Here, S6*R* represents a spherical 6*R* linkage.

In Fig. 4-12, a basic assembly of four-crease, five-crease and six-crease vertices is founded from the pattern by splitting vertices with $\mathrm{SI}_{1,4}$ and $\mathrm{SII}_{1,3}$, as shown in Fig. A1. According to the truss analogy, it contains $j = 22$ nodes, $b = 59$ bars. Considering the rank of its equilibrium matrix $r = 59$, it is found that the pattern is non-overconstrained with one-DOF.

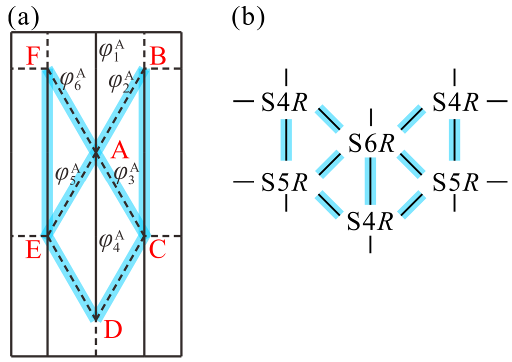

Fig. 4-12 A basic assembly of four-crease, five-crease, and six-crease vertices. (a) The one-DOF basic assembly and (b) its corresponding diagram.

The one-DOF assemblies in Fig. 4-10(e) and Fig. 4-11(f) can be replaced by any pattern in the figures above, as long as the two connected vertices satisfy motion compatibility. Those one-DOF basic assemblies are used to determine that 42 of 96 cases in appendix A and Table 4-1 are of one-DOF, such as the two patterns in Fig. 4-13. The remaining patterns are multi-DOF, due to their one-DOF basic assemblies cannot provide enough constraints to determine the motion of all the vertices.

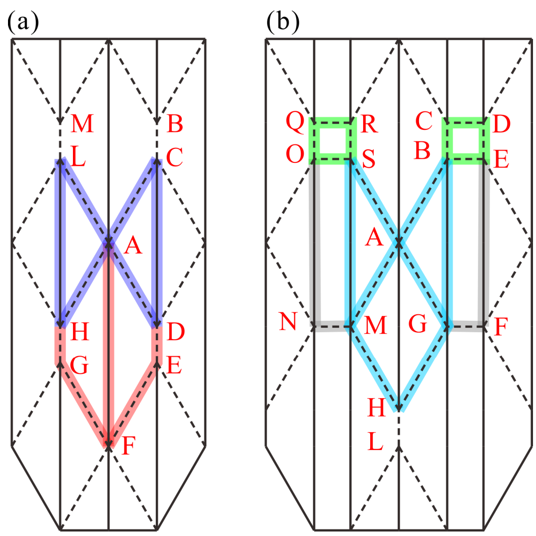

Fig. 4-13 One-DOF origami patterns verified by one-DOF basic assemblies. (a) The flat-foldable origami pattern; (b) the non-flat-foldable origami pattern.

The pattern (Fig. 4-13(a)) derived by splitting vertices with $SI_{1,3}$ and SII_0 has the one-DOF basic assembly of vertices A, C, D, H, L which is identical to the pattern in Fig. 4-11(g). Four-crease vertices E and G connecting to the one-DOF basic assembly construct a new one-DOF assembly of A, C, D, E, G, H, L. This assembly gives three inputs to the spherical 6*R* linkage F and fully determines its motion, according to the diagram in Fig. 4-11(f). Hence, this pattern can be considered as the combination of four-crease vertices B, M and basic assemblies in Fig. 4-11(f), (g) to obtain one-DOF with flat-foldability, whose motion sequence is shown in Fig. 4-14(a).

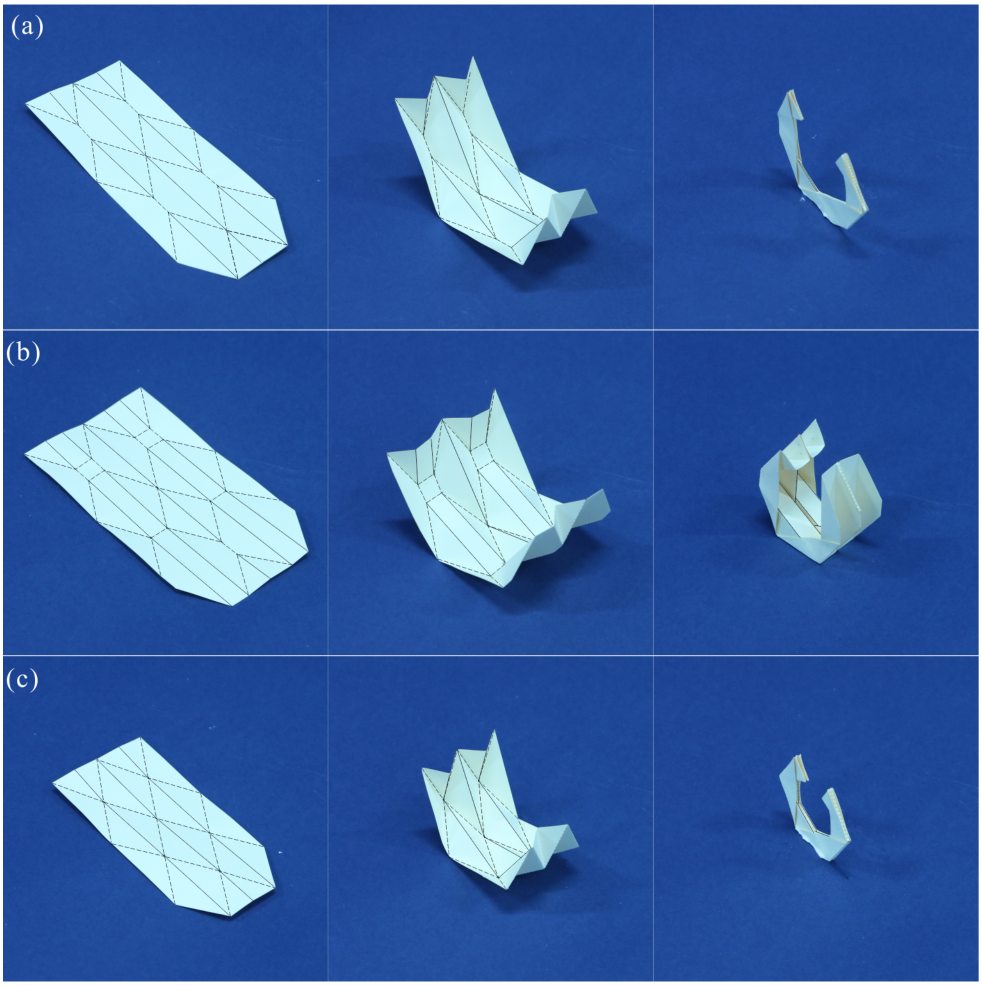

Fig. 4-14 Motion sequences of rigid origami. (a) The flat-foldable origami pattern and (b) the non-flat-foldable origami pattern derived from splitting vertices; (c) the multi-vertex diamond origami pattern in symmetric folding.

By splitting vertices with $SI_{1,4}$ and $SII_{1,3}$, the pattern in Fig. 4-13(b) can be obtained. The assemblies of vertices B, C, D, E and vertices O, Q, R, S are the same as the one-DOF basic assembly in Fig. 4-9(a). The assembly of vertices A, B, G, H, M, S is identical to the one-DOF basic assembly in Fig. 4-12(a). The combination of the three basic assemblies can be regarded as the one-DOF assembly in Fig. 4-10(e) and gives two inputs to the five-crease vertices N and F. So this pattern is considered as the combination of four-crease vertex L and basic assemblies in Fig. 4-9(a), Fig. 4-10(e) and Fig. 4-12 (a) with one-DOF, whose motion sequence is shown in Fig. 4-14(b). Due to the five-crease vertex, this pattern is non-flat-foldable. As two one-DOF patterns can be considered as the assembly of kinematically equivalent diamond vertex and patterns DI, DII, DI-II, they will retain the motion with all vertices in symmetric folding. Hence, they are kinematically equivalent to original diamond origami pattern with symmetric folding shown in Fig. 4-14(c).

4.4 Hinge-Removing on Thick-Panel Origami

An origami pattern with two flat-foldable four-crease origami vertices shared a crease a_3/b_3 is shown in Fig. 4-15(a). In this pattern, the sector angles satisfy $\beta > \alpha$ and $\delta > \gamma$. The distance between the vertices, $d_{\mathrm{AB}} \geq r^{\mathrm{A}}\cos(\beta-\alpha)+r^{\mathrm{B}}\cos(\delta-\gamma)$, ensures the pattern being fully flat-foldable. Its thick-panel form is constructed by applying the offsetting hinge technique, as shown in Fig. 4-15(b), where $t^{\mathrm{A}}_{i(i+1)}$ and $t^{\mathrm{B}}_{i(i+1)}$ (i=1, 2, 3, 4; when i=4, i+1=1) represent the thickness of panels corresponding to vertices A and B. Its corresponding mobile assembly of two Bennett linkages shared a hinge is derived from connecting the adjacent hinge axes along the nearest distance with bars according to section 2.3, as shown in Fig. 4-15(c). Here, twists of Bennett linkages A and B are noted by $\alpha^{Be}_{i(i+1)}$ and $\beta^{Be}_{i(i+1)}$, respectively; link lengths of them are noted by $a^{Be}_{i(i+1)}$ and $b^{Be}_{i(i+1)}$, respectively. The twists and link lengths satisfy

$$\begin{aligned}
&\alpha^{Be}_{12}=\alpha^{Be}_{34}=\pi-\alpha,\ \alpha^{Be}_{23}=\alpha^{Be}_{41}=\pi-\beta,\\
&\beta^{Be}_{12}=\beta^{Be}_{34}=\pi-\gamma,\ \beta^{Be}_{23}=\beta^{Be}_{41}=\pi-\delta,\\
&a^{Be}_{12}=a^{Be}_{34}=a^{\mathrm{A}},\ a^{Be}_{23}=a^{Be}_{41}=b^{\mathrm{A}},\\
&b^{Be}_{12}=b^{Be}_{34}=a^{\mathrm{B}},\ b^{Be}_{23}=b^{Be}_{41}=b^{\mathrm{B}}.
\end{aligned} \tag{4-17}$$

Here, link lengths $a^{\mathrm{B}}>b^{\mathrm{A}},\ b^{\mathrm{B}}>a^{\mathrm{A}}$ are chosen. As the link lengths of the mobile assembly correspond to the thickness of panels, they satisfy the following conditions

$$\begin{aligned}
&a^{\mathrm{A}}=t^{\mathrm{A}}_{12}=t^{\mathrm{A}}_{34},\ b^{\mathrm{A}}=t^{\mathrm{A}}_{23}=t^{\mathrm{A}}_{41},\\
&a^{\mathrm{B}}=t^{\mathrm{B}}_{12}=t^{\mathrm{B}}_{34},\ b^{\mathrm{B}}=t^{\mathrm{B}}_{23}=t^{\mathrm{B}}_{41}.
\end{aligned} \tag{4-18}$$

Due to $t^{\mathrm{A}}_{12}+t^{\mathrm{A}}_{41}=t^{\mathrm{A}}_{23}+t^{\mathrm{A}}_{34},\ t^{\mathrm{B}}_{12}+t^{\mathrm{B}}_{41}=t^{\mathrm{B}}_{23}+t^{\mathrm{B}}_{34}$, this thick-panel origami can be compactly folded into a configuration that dihedral angles of creases are zero and panels $\mathrm{P}^{\mathrm{A}}_{12}$, $\mathrm{P}^{\mathrm{A}}_{41}$,

$\mathrm{P}_{12}^{\mathrm{B}}$, $\mathrm{P}_{41}^{\mathrm{B}}$ are stored in the gap between panels $\mathrm{P}_{23}^{\mathrm{A}}/\mathrm{P}_{34}^{\mathrm{B}}$ and $\mathrm{P}_{23}^{\mathrm{B}}/\mathrm{P}_{34}^{\mathrm{A}}$. It should be noted that the thickness of other panels should satisfy $t_0 > 0,\ t_0' > 0$ to form a continuously movable thick-panel origami structure.

By removing the common hinge a_3/b_3 in the assembly of two Bennett linkages (Fig. 4-15(c)) and the two links with lengths a_{23}^{Be} and a_{34}^{Be} connected by this hinge, the Waldron's hybrid 6*R* linkage is obtained, as shown in Fig. 4-15(d). Here, $\alpha_{j(j+1)}^{Wa}$ and $a_{j(j+1)}^{Wa}$ (*j*=1, 2, 3,..., 6; when *j*=6, *j*+1=1) represent the twists and link lengths of Waldron's hybrid 6*R* linkage, and they satisfy

$$\begin{aligned}
&\alpha_{12}^{Wa} = \alpha_{12}^{Be} = \pi - \alpha,\ \alpha_{23}^{Wa} = \beta_{34}^{Be} - \alpha_{23}^{Be} = \beta - \gamma,\\
&\alpha_{34}^{Wa} = \beta_{41}^{Be} = \pi - \delta,\ \alpha_{45}^{Wa} = \beta_{12}^{Be} = \pi - \gamma,\\
&\alpha_{56}^{Wa} = \beta_{23}^{Be} - \alpha_{34}^{Be} = \alpha - \delta,\ \alpha_{61}^{Wa} = \alpha_{41}^{Be} = \pi - \beta,\\
&c_{12}^{Wa} = a_{12}^{Be} = a^{\mathrm{A}},\ c_{23}^{Wa} = b_{34}^{Be} - a_{23}^{Be} = a^{\mathrm{B}} - b^{\mathrm{A}},\\
&c_{34}^{Wa} = b_{41}^{Be} = b^{\mathrm{B}},\ c_{45}^{Wa} = b_{12}^{Be} = a^{\mathrm{B}},\\
&c_{56}^{Wa} = b_{23}^{Be} - a_{34}^{Be} = b^{\mathrm{B}} - a^{\mathrm{A}},\ c_{61}^{Wa} = a_{41}^{Be} = b^{\mathrm{A}}.
\end{aligned} \tag{4-19}$$

Correspondingly, removing both the hinge a_3b_3 in Fig. 4-15(b) and the stairs of panels which are with thickness t_{23}^{A} and t_{34}^{A}, a thick-panel origami pattern with six creases corresponding to the Waldron's hybrid 6*R* linkage is constructed, as shown in Fig. 4-15(e) where $t_{j(j+1)}^{Wa}$ represent the thickness of panels and satisfies

$$\begin{aligned}
&t_{12}^{Wa} = c_{12}^{Wa} = a^{\mathrm{A}},\ t_{23}^{Wa} = c_{23}^{Wa} = a^{\mathrm{B}} - b^{\mathrm{A}},\\
&t_{34}^{Wa} = c_{34}^{Wa} = b^{\mathrm{B}},\ t_{45}^{Wa} = c_{45}^{Wa} = a^{\mathrm{B}},\\
&t_{56}^{Wa} = c_{56}^{Wa} = b^{\mathrm{B}} - a^{\mathrm{A}},\ t_{61}^{Wa} = c_{61}^{Wa} = b^{\mathrm{A}}.
\end{aligned} \tag{4-20}$$

Since the assembly of two Bennett linkages is kinematically equivalent to the Waldron's hybrid 6*R* linkage, the thick-panel origami with two four-crease vertices and the generated thick-panel origami pattern with six creases also have equivalent motion. Back on the zero-thickness origami pattern, one slit can be made at the crease a_3/b_3 to remove the shared hinge. Then, a pattern with six creases is obtained, which is actually Bennett 6*R* hybrid linkage with one-DOF.

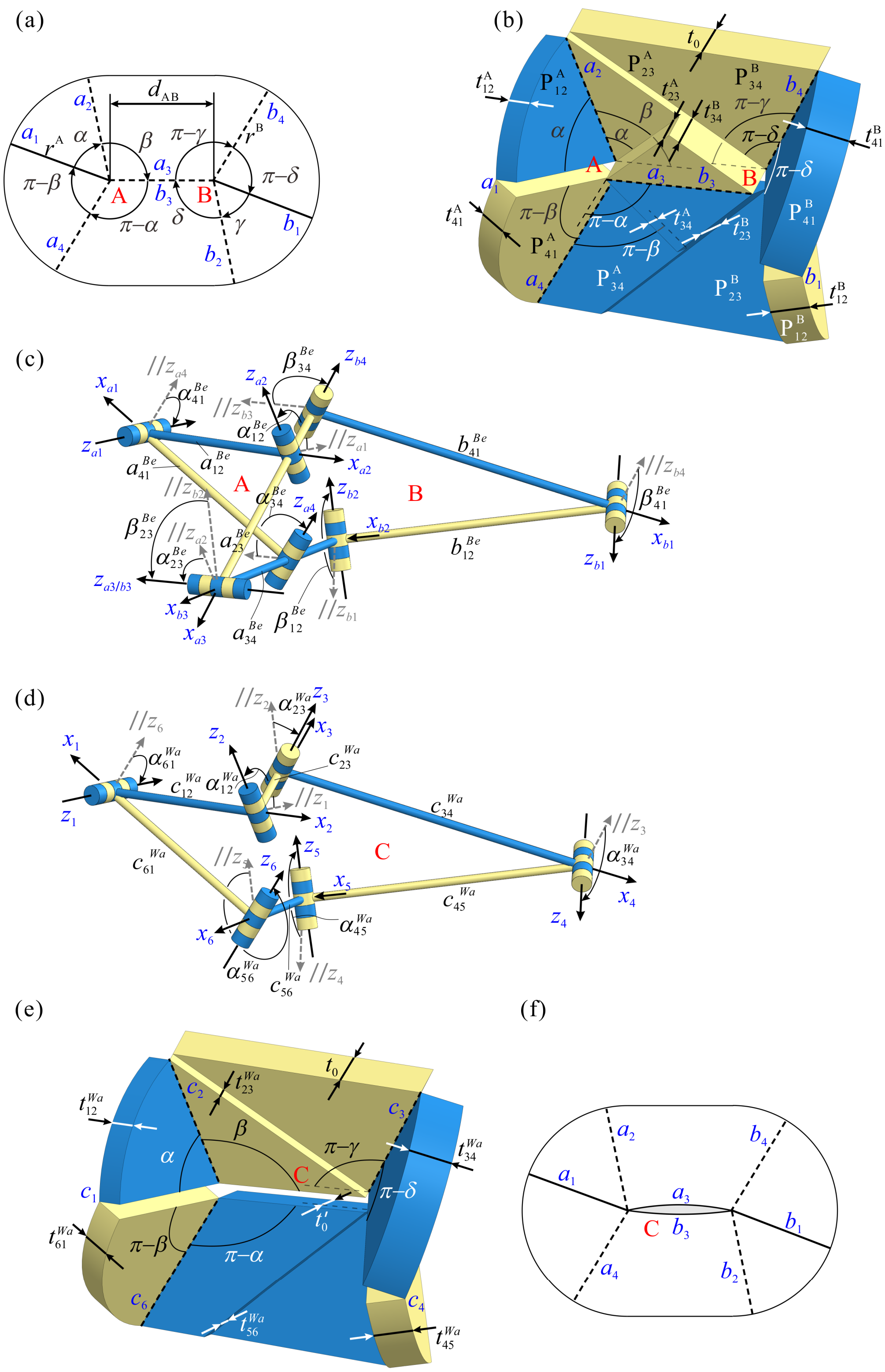

Fig. 4-15 Correspondence between the construction of Waldron's hybrid 6*R* linkage and the hinge-removing on thick-panel origami. (a) An origami pattern with two four-crease vertices; (b) the corresponding thick-panel origami pattern; (c) the assembly of two Bennett linkages; (d) the Waldron's hybrid 6*R* linkage; (e) the thick-panel origami pattern with six creases derived from (b) by removing the shared hinges and stairs; (f) the origami pattern with a slit at the shared crease. The slit is purposely made larger to highlight their presence.

For the origami pattern mixed with four-crease and six-crease vertices shown in Fig. 4-13(a), its corresponding thick-panel origami pattern is constructed by applying the offset hinge technique, as shown in Fig. 4-16(a). To obtain the thick-panel origami pattern with flat-surface unfolded profiles, panels forming the six-crease vertex should have equal thickness according to the study of section 3.4. Every two adjacent four-crease vertices B&C, D&E, G&H, L&M correspond to an assembly of two Bennett linkages by sharing a hinge, whose shared panels and hinge forms the stairs. According to construction of thick-panel origami in Fig. 4-15(e), the shared hinges can be removed. Taking $\alpha=\pi-\beta=\gamma=\pi-\delta$ and $t_{23}^{Wa}=t_{56}^{Wa}=0$ to Eqs. (4-20), and considering Eq. (1-13c),

$$t_{12}^{Wa}=t_{34}^{Wa}=t_{45}^{Wa}=t_{61}^{Wa}=a^{\mathrm{A}}=b^{\mathrm{A}}=a^{\mathrm{B}}=b^{\mathrm{B}} \tag{4-21}$$

is derived to obtain the thick-panel origami pattern with flat-surface unfolded profiles. Hence, the four-crease vertices should correspond to Bennett linkages with identical link lengths. When the thickness of shared panels between every two vertices B&C, D&E, G&H, L&M are equal to that of other panels, the thick-panel origami pattern with flat-surface unfolded profiles can be obtained, as shown in Fig. 4-16(b). This pattern can be regarded as an assembly of Waldron's hybrid 6*R* linkages and plane-symmetric Bricard linkages with one DOF. It also can be regarded as the vertex-splitting technique applied on the thick-panel model shown in Fig. 3-7(a).

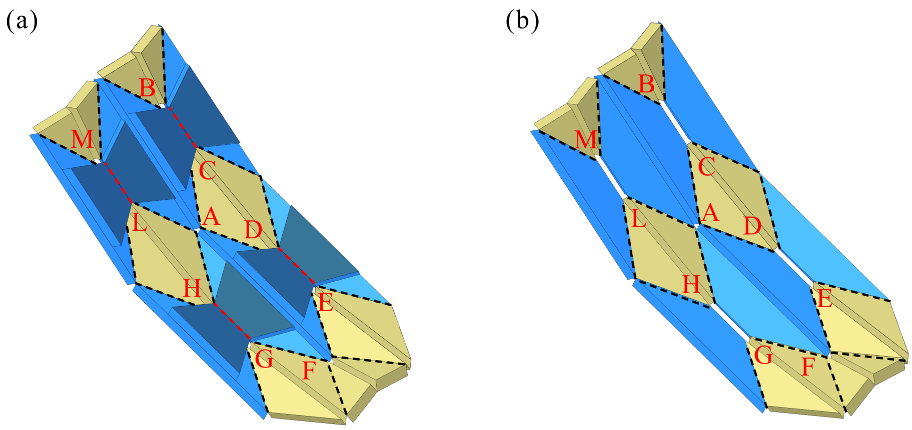

Fig. 4-16 Hinge-removing on a hybrid thick-panel origami with four-crease and six-crease vertices. (a) The thick-panel origami pattern; (b) the thick-panel origami with flat-surface unfolded profiles.

Hinge-removing can be used to other four-crease origami patterns, such as the Tachi-Miura origami pattern and the identical linkage-type origami pattern to construct thick-panel origami pattern with flat-surface unfolded profiles.

Tachi-Miura origami is a Miura-base rigid origami, whose crease pattern with sector angles α, $\pi-\alpha$ is shown in Fig. 4-17(a). By applying the offset hinge technique, its corresponding thick-panel origami pattern is constructed, as shown in Fig. 4-17(b). Hinge-removing can be carried out to these hinges connecting panels with stairs. After removing the hinges and stairs, the thick-panel origami pattern in Fig. 4-17(c) with flat-surface unfolded profiles is obtained. In this thick-panel origami, four-crease vertices A and B, C and D, L and M, N and O are transformed into Waldron's hybrid 6*R* linkage. Hence, this pattern is related to an assembly of Waldron's hybrid 6*R* linkages and Bennett linkages with one-DOF. This thick-panel origami can be folded on a flat surface, so that large deployable structures can use this origami which can be expanded infinitely with reasonable parameters.

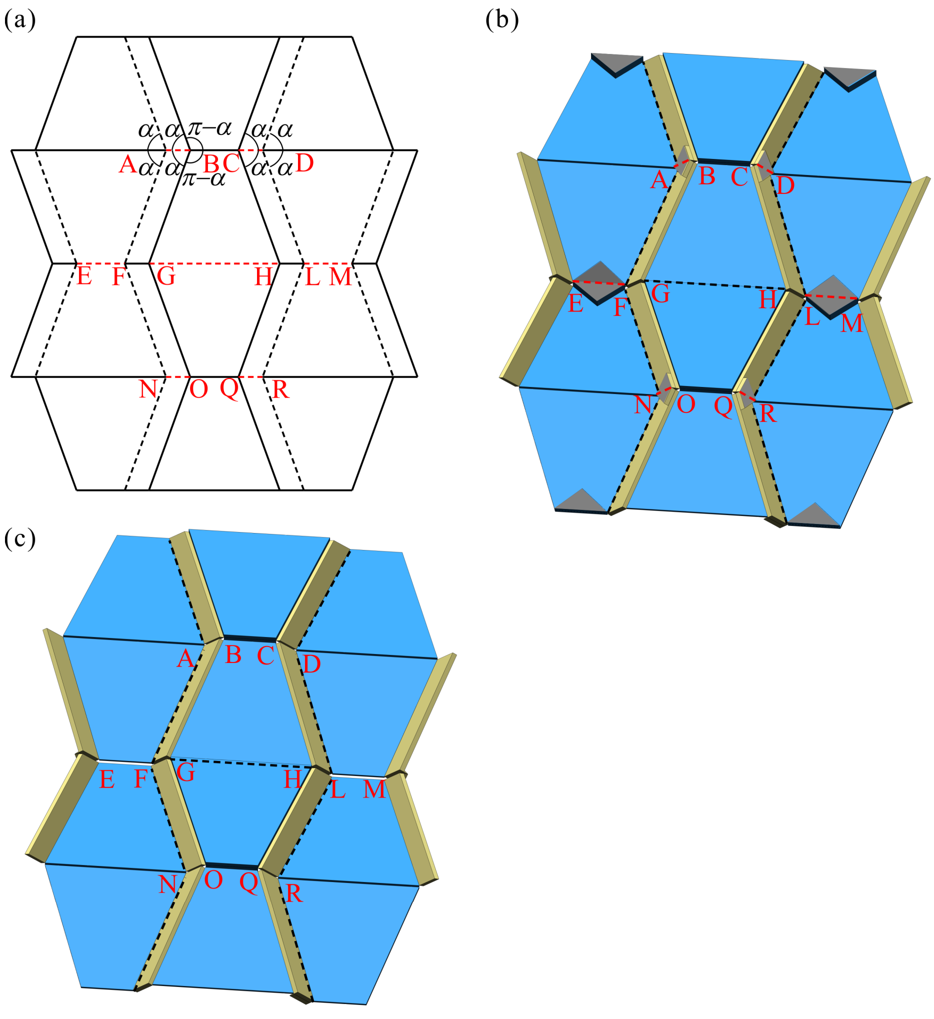

Fig. 4-17 Hinge-removing on Tachi-Miura thick-panel origami. (a) Crease pattern of Tachi-Miura thick-panel origami pattern; (b) the thick-panel form; (c) the thick-panel origami with flat-surface unfolded profiles.

Identical linkage-type origami pattern with eight identical vertices is shown in Fig. 4-18, where each vertex has sector angles α, β, $\pi-\beta$, $\pi-\alpha$. According to the thick-panel method, its corresponding thick-panel origami pattern by replacing the spherical 4*R* linkages by identical Bennett linkages can be constructed, as shown in Fig. 4-18(b). As the panels connected by hinges at the red creases cause stairs, the hinges can be removed to transform the assemblies of two Bennett linkages at vertices A and B, vertices C and D, vertices E and F, vertices G and H into Waldron's hybrid 6*R* linkages with one-DOF. By varying the thickness of these panels to be equal, a thick-panel origami pattern with flat-surface unfolded profiles is constructed, as shown in Fig. 4-18(c).

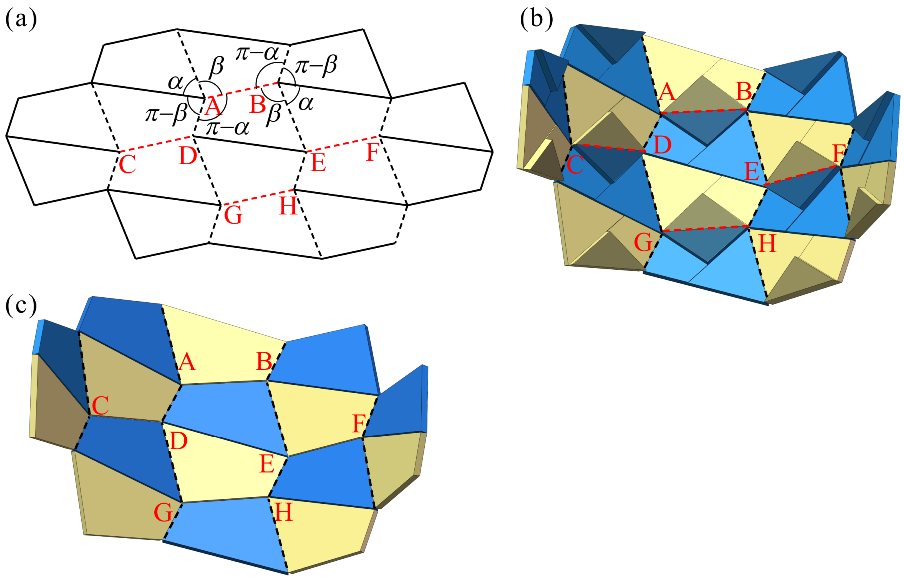

Fig. 4-18 Hinge-removing on identical linkage-type thick-panel origami. (a) Crease pattern of identical linkage-type thick-panel origami pattern; (b) the corresponding thick-panel form; (c) the identical linkage-type thick-panel origami with flat-surface unfolded profiles.

4.5 Conclusions

This chapter presents a vertex-splitting technique to reduce the DOF of the diamond origami and construct one-DOF origami patterns. Two vertex-splitting schemes are proposed from the diamond vertex and three types of unit patterns are generated. The kinematic analysis indicates that the three patterns are equivalent to the diamond vertex with symmetric folding. By applying vertex-splitting to multi-vertex diamond origami pattern, a large number of rigid origami patterns are constructed. Six types of one-DOF basic assemblies are discussed, which ensure the one-DOF cases of those origami patterns. Among them, two one-DOF origami patterns mixed with four-crease, six-crease and/or five-crease vertices are discussed, one of which is flat-foldable and the other is non-flat-foldable. They maintain the kinematic motion characteristics of diamond origami pattern with symmetric folding. Meanwhile, the vertex-splitting technique can be applied to other multi-DOF origami patterns, such as waterbomb pattern and Resch patterns. The one-DOF basic assemblies form a new rule in the one-DOF determination in complex origami patterns.

Variations of thick-panel origami corresponding to the construction of Waldron's hybrid 6*R* linkage from Bennett linkages are studied, which displays a kinematically equivalent crease thick-panel origami pattern with six creases can be derived from thick-panel origami pattern with two four-crease vertices by removing the shared hinge. This inspires hinge-removing which is used to construct three thick-panel origami patterns with flat-surface unfolded profiles from the four- and six-crease thick-panel origami pattern, Tachi-Miura origami pattern, and identical linkage-type thick-panel origami pattern.

Chapter 5 Achievements and Future Works

The aim of this dissertation is to study the relationship between spatial linkages and rigid origami by taking their thick-panel origami forms as the intermediate bridges to design mobile assemblies of spatial linkages, rigid origami and the thick-panel origami patterns. In this chapter, the main achievements followed by an overview of further works are summarised.

5.1 Main Achievements

- **Mobile assemblies of Bennett linkages from four-crease origami patterns**

First, a transition technique is proposed to realize the mobile assemblies of Bennett linkages from four-crease origami patterns by taking their thick-panel forms as the intermedium. Mobile assemblies of equilateral Bennett linkages have been derived by applying the technique to Miura-ori and graded Miura-ori pattern. Different mountain-valley crease assignments of the supplementary-type origami patterns have been confirmed to correspond to mobile assemblies of Bennett linkages with negative link lengths. Applying the technique to the identical linkage-type origami pattern produces a new Bennett linkage mobile assembly.

The technique presented in Chapter 2 offers a new approach to construct mobile assemblies of spatial linkages from origami patterns. The outcomes widen the existing geometric conditions to design mobile assemblies of Bennett linkages.

- **Diamond thick-panel origami and mobile assemblies of Bricard linkages**

Second, equivalence between the diamond thick-panel origami and mobile assembly of plane-symmetric Bricard linkages has been studied to design new of both. Diamond assembly has been constructed from the diamond thick-panel origami based on their kinematic equivalence, whose construction conditions have been extended to two new mobile assemblies of plane-symmetric Bricard linkages with compatibility analysis. According to the condition of one assembly, a diamond thick-panel origami with flat-surface unfolded profiles, and a graded diamond thick-panel origami pattern with flat-surface unfolded profiles and spirally folded configuration are generated by varying the thickness and sector angles of panels.

A prototype of the graded diamond thick-panel origami pattern without physical interference has been constructed in Chapter 3, which is more potential in engineering applications, such as solar panels.

- **Vertex-Splitting on Multi-DOF Origami Pattern**

Third, vertex-splitting technique is proposed to reduce the DOF of diamond origami pattern. We also have constructed one-DOF thick-panel origami pattern with flat-surface unfold profile by removing hinges. Two vertex-splitting schemes have been proposed to generate three types of unit patterns with equivalently symmetric folding from the diamond vertex. A number of origami patterns are generated by applying vertex-splitting to multi-vertex diamond origami pattern. One-DOF basic assemblies are discussed to ensure the one-DOF origami patterns which can be mixed with four-crease, five-crease and six-crease vertices.

The construction of the Waldron's hybrid 6*R* linkage from an assembly of two Bennett linkages by removing the shared hinge, and the variation of their corresponding thick-panel origami pattern are studied. Hinge-removing of thick-panel origami pattern with two four-crease vertices is proposed, which has been used to the four- and six-crease thick-panel origami pattern, Tachi-Miura thick-panel origami pattern and identical linkage-type thick-panel origami pattern to construct three thick-panel origami patterns with one-DOF and flat-surface unfolded profiles.

The newly-found one-DOF origami patterns in Chapter 4 will facilitate engineering applications of rigid origami. The vertex-splitting technique paves a way to construct one-DOF origami patterns. The hinge-removing not only constructs the flat-surface unfold thick-panel origami pattern for application, but also indicates the relationship between the constructions of Bennett-based linkages and variations of corresponding thick-panel origami patterns.

5.2 Future Works

The research reported in this dissertation provides many opportunities to study further.

Firstly, the transition technique is used to construct mobile assemblies of spatial overconstrained linkages from rigid origami patterns based on their thick-panel origami forms. As there are multiply rigid origami patterns, such as waterbomb origami pattern and Resch pattern, each rigid origami pattern can be furtherly studied to find mobile assemblies of spatial overconstrained linkages. In addition, multi-layer origami patterns, such as Miura-ori, can be used to construct mobile assemblies of multi-layer Bennett linkages. As none of the discussed origami patterns can transit to the case 1 mobile assembly of the Bennett linkages, we conjuncture that this mobile assembly may correspond to an origami pattern that differs from commonly known ones. It would be extremely interesting to find out what it is.

Secondly, in the research of diamond thick-panel origami pattern and corresponding mobile assemblies of plane-symmetric Bricard linkages, it should be noted that diamond vertex of six creases has three degrees of freedom. Due to the geometric condition with both line and plane symmetry, line-symmetric constraints can be applied to transfer it into the thick-panel forms, which will lead to the new mobile assemblies of line-symmetric Bricard linkages.

Thirdly, in the work on vertex-splitting, two schemes are proposed to construct one-DOF rigid origami patterns with equivalently symmetric folding to diamond origami pattern. How to widen the vertex-splitting technique to reduce other multi-DOF origami patterns to construct one-DOF origami patterns is an interesting research subject. First, the direction of splitting vertex and the added creases can become more general. Second, how to determine the DOF of newly-generated origami by splitting vertices. Third, supposing that the obtained origami is non-rigid, the relationships between adding creases or slice creases and the number of DOF of an origami pattern may be studied to transform it into one-DOF origami.

Fourthly, the hinge-removing on thick-panel origami pattern indicates the relationship between the construction of Waldron's hybrid linkages and variations of four-crease thick-panel origami pattern. Therefore, further study on the relationship of other Bennett-based linkages, such as Goldberg 5*R* and Goldberg 6*R* linkages, may bring new possibilities of the construction of thick-panel origami.

Finally, in this dissertation, we have only done some theoretical research on the mobile assemblies of spatial linkages and rigid origami. We do not take the following features into consideration. One is the section area of the bar and the number of hinges connected by two panels which can influence the strength and rigidity of a thick-panel origami pattern. The other is the influence of the manufacturing errors on the movement of the mechanism. In addition, the target configuration and package volume are two important factors to design a deployable structure in engineering applications. Hence, the relationship between the design parameters of the deployable structures and the target configuration and package volume needs further study.

References

[1] You Z. Motion structures extend their reach [J]. Materials Today, 2007, 10(12): 52-57.

[2] Hedgepeth J M. Structures for remotely deployable precision antennas [J]. Langley Research Center, Earth Science Geostationary Platform Technology, 1989, 109-128.

[3] Guest S, Pellegrino S. A new concept for solid surface deployable antennas [J]. Acta Astronautica, 1996, 38(2): 103-113.

[4] Cui J, Huang H, Li B, et al. A novel surface deployable antenna structure based on special form of bricard linkages [M]//Dai S J, Zoppi M, Kong X. Advances in Reconfigurable Mechanisms and Robots I. London; Springer London. 2012: 783-792.

[5] Santiago-Prowald J, Baier H. Advances in deployable structures and surfaces for large apertures in space [J]. CEAS Space Journal, 2013, 5(3): 89-115.

[6] Morterolle S, Maurin B, Dube J F, et al. Modal behavior of a new large reflector conceptual design [J]. Aerospace Science and Technology, 2015, 42(74-79).

[7] Xu Y, Guan F L. Structure-electronic synthesis design of deployable truss antenna [J]. Aerospace Science and Technology, 2013, 26(1): 259-267.

[8] Miura K. Triangles and quadrangles in space [C]. Proceedings of the 50th Symposium of the International Association for Shell and Spatial Structures, Valencia: Editorial Universitat Politècnica de València, 2009:27-38.

[9] Dufour L, Owen K, Mintchev S, et al. A drone with insect-inspired folding wings [C]. Proceedings of the 2016 IEEE/RSJ International Conference on Intelligent Robots and Systems (IROS), Daejeon: IEEE, 2016: 1576-1581.

[10] Mira L A, Thrall A P, De Temmerman N. Deployable scissor arch for transitional shelters [J]. Automation in Construction, 2014, 43: 123-131.

[11] Lee T U, Gattas J M. Geometric design and construction of structurally stabilized accordion shelters [J]. Journal of Mechanisms and Robotics, 2016, 8(3): 031009.

[12] Pellegrino S, Kassabian P E, You Z. Retractable roof structures [J]. Structures & Buildings, 1999, 134(1): 45-56.

[13] Thrall A P, Adriaenssens S, Paya-Zaforteza I, et al. Linkage-based movable bridges: Design methodology and three novel forms [J]. Engineering Structures, 2012, 37: 214-223.

[14] Lederman G, You Z, Glišić B. A novel deployable tied arch bridge [J]. Engineering Structures, 2014, 70: 1-10.

[15] Kuribayashi K, Tsuchiya K, You Z, et al. Self-deployable origami stent grafts as a biomedical application of Ni-rich TiNi shape memory alloy foil [J]. Materials Science and Engineering: A, 2006, 419(1-2): 131-137.

[16] Edmondson B J, Bowen L A, Grames C L, et al. Oriceps: Origami-inspired forceps [C]. Proceedings of the ASME 2013 International Design Engineering Technical Conferences and Computers and Information in Engineering Conference, Snowbird: ASME, 2013: V001T01A027.

[17] Hawkes E, An B, Benbernou N M, et al. Programmable matter by folding[J]. Proceedings of the National Academy of Sciences, 2010, 107(28): 12441-12445.

[18] Koh J S, Cho K J. Omega-shaped inchworm-inspired crawling robot with large-index-and-pitch (LIP) SMA spring actuators [J]. IEEE/ASME Transactions On Mechatronics, 2013, 18(2): 419-429.

[19] Belke C H, Paik J. Mori: a modular origami robot [J]. IEEE/ASME Transactions on Mechatronics, 2017, 22(5): 2153-2164.

[20] Rus D, Tolley M T. Design, fabrication and control of origami robots [J]. Nature Reviews Materials, 2018: 1.

[21] Escrig F, Sanchez J, Valcarcel J P. Two way deployable spherical grids [J]. International Journal of Space Structures, 1996, 11(1-2): 257-274.

[22] You Z, Pellegrino S. Foldable bar structures [J]. International Journal of Solids and Structures, 1997, 34(15): 1825-1847.

[23] Akg N Y, Gantes C J, Kalochairetis K E, et al. A novel concept of convertible roofs with high transformability consisting of planar scissor-hinge structures [J]. Engineering Structures, 2010, 32(9): 2873-2883.

[24] Akgün Y, Gantes C J, Sobek W, et al. A novel adaptive spatial scissor-hinge structural mechanism for convertible roofs[J]. Engineering Structures, 2011, 33(4): 1365-1376.

[25] Zhao J S, Wang J Y, Chu F, et al. Structure synthesis and statics analysis of a foldable stair [J]. Mechanism and Machine Theory, 2011, 46(7): 998-1015.

[26] Bennett G T. A new mechanism [J]. Engineering, 1903, 76(12): 777-778.

[27] Myard F E. Contribution à la géométrie des systèmes articulés [J]. Bull. Soc. Math. France, 1931, 59: 183-210.

[28] Bricard R. Leçons de cinématique, T. II [J]. Paris, France: Gauthier-Villars, 1927.

[29] Chen Y. Design of structural mechanisms [D]. Oxford: University of Oxford, doctoral dissertation, 2003.

[30] Silverberg J L, Evans A A, McLeod L, et al. Using origami design principles to fold reprogrammable mechanical metamaterials [J]. Science, 2014, 345(6197): 647-650.

[31] Overvelde J T B, De Jong T A, Shevchenko Y, et al. A three-dimensional actuated origami-inspired transformable metamaterial with multiple degrees of freedom [J]. Nature communications, 2016, 7: 10929.

[32] Li S, Vogt D M, Rus D, Wood R J. Fluid-driven origami-inspired artificial muscles [J]. Proceedings of the National Academy of Sciences, 2017: 201713450.

[33] Jeong D, Lee K. Design and analysis of an origami-based three-finger manipulator [J]. Robotica, 2018, 36(2): 261-274.

[34] Pagano A, Yan T, Chien B, et al. A crawling robot driven by multi-stable origami [J]. Smart Materials and Structures, 2017, 26(9): 094007.

[35] Miura K. Proposition of pseudo-cylindrical concave polyhedral shells [M]. Institute of Space and Aeronautical Science, University of Tokyo, 1969.

[36] Miura K. Method of packaging and deployment of large membranes in space [J]. Title The Institute of Space and Astronautical Science Report, 1985, 618: 1-9.

[37] Dai J S, Rees Jones J. Mobility in metamorphic mechanisms of foldable/erectable kinds [J]. Journal of Mechanical Design, 1999, 121(3): 375-382.

[38] Dai J S, Rees Jones J. Matrix representation of topological changes in metamorphic mechanisms[J]. Journal of Mechanical Design, 2005, 127(4): 837-840.

[39] Wang K, Chen Y. Folding a patterned cylinder by rigid origami [M]. // Wang-Iverson P, Lang R J, Yim M. Origami 5. New York: A K Peters/CRC Press. 2011: 265-276.

[40] Chen Y, Peng R, You Z. Origami of thick panels [J]. Science, 2015, 349(6246): 396-400.

[41] Denavit J, Hartenberg R S. A kinematic notation for lower-pair mechanisms based on matrices [J]. Journal of Applied Mechanics, 1955, 22: 215-221.

[42] Feng H, Peng R, Ma J, et al. Rigid foldability of generalized triangle twist origami pattern and its derived 6*R* linkages [J]. Journal of Mechanisms and Robotics, 2018, 10(5): 051003.

[43] Maxwell JC. On the calculation of the equilibrium and stiffness of frames [J]. Philosophical Magazine, 1864, XXVII: 599.

[44] Yang F, Chen Y, Kang R, et al. Truss transformation method to obtain the non-overconstrained forms of 3D overconstrained linkages [J]. Mechanism and Machine Theory, 2016, 102: 149-166.

[45] Pellegrino S, Calladine C R. Matrix analysis of statically and kinematically indeterminate frameworks [J]. International Journal of Solids and Structures, 1986, 22(4): 409-428.

[46] Pellegrino S. Structural computations with the singular value decomposition of the equilibrium matrix [J]. International Journal of Solids and Structures, 1993, 30(21): 3025-3035.

[47] Tarnai T. Infinitesimal and finite mechanisms [M]//Pellegrino S. Deployable Structures. Vienna: Springer, 2001: 113-142.

[48] Chen Y, Yang F, You Z. Transformation of polyhedrons [J]. International Journal of Solids and Structures, 2018, 138: 193-204.

[49] Yang F, Chen Y. One-DOF transformation between tetrahedron and truncated tetrahedron [J]. Mechanism and Machine Theory, 2018, 121: 169-183.

[50] Zhang M, Yang F, Ma J, et al. Design of one-DOF triangular Resch pattern with thick-panel origami [C]. Proceedings of the ASME 2018 International Design Engineering Technical Conferences and Computers and Information in Engineering Conference, Quebec: ASME, 2018: V05BT07A067.

[51] Hunt K H. Kinematic geometry of mechanisms [M]. Oxford: Oxford University Press, 1978.

[52] Bennett G T. LXXVII. The parallel motion of Sarrut and some allied mechanisms[J]. Philosophical Magazine, 1905, 9(54): 803-810.

[53] Sarrus P T. Note sur la transformation des mouvements rectilignes alternatifs, en mouvements circulaires, et reciproquement [J]. Académie des Sciences, 1853, 36: 1036-1038.

[54] Baker J E. The Bennett linkage and its associated quadric surfaces [J]. Mechanism and machine theory, 1988, 23(2): 147-156.

[55] Goldberg M. New five-bar and six-bar linkages in three dimensions [J]. Transactions of ASME, 1943, 65: 649-661.

[56] Baker J E. An analysis of the Bricard linkages [J]. Mechanism and Machine Theory, 1980, 15(4): 267-286.

[57] Baker J E. The Bennett, Goldberg and Myard linkages—in perspective [J]. Mechanism and Machine Theory, 1979, 14(4): 239-253.

[58] Wohlhart K. Merging two general Goldberg 5*R* linkages to obtain a new 6*R* space mechanism [J]. Mechanism and Machine Theory, 1991, 26(7): 659-668.

[59] Song C Y, Chen Y. A family of mixed double-Goldberg 6*R* linkages [J]. Proceedings of the Royal Society A: Mathematical, Physical and Engineering Sciences, 2011, 468(2139): 871-890.

[60] Song C Y, Chen Y. A spatial 6*R* linkage derived from subtractive Goldberg 5*R* linkages [J]. Mechanism and Machine Theory, 2011, 46(8): 1097-1106.

[61] Waldron K J. Hybrid overconstrained linkages [J]. Journal of Mechanisms, 1968, 3(2): 73-78.

[62] Baker J E. A comparative survey of the Bennett-based, 6-revolute kinematic loops [J]. Mechanism and Machine Theory, 1993, 28(1): 83-96.

[63] Song C Y, Feng H, Chen Y, et al. Reconfigurable mechanism generated from the network of Bennett linkages [J]. Mechanism and Machine Theory, 2015, 88: 49-62.

[64] Wohlhart K. On isomeric overconstrained space mechanisms [C]. Proceedings of the 8th IFToMM World Congress, Prague: IFToMM, 1991: 153-158.

[65] Guo H, Song X, Li L, et al. Type synthesis of deployable single-loop overconstrained linkages based on Bennett linkages [J]. Mechanism and Machine Theory, 2018, 120: 1-29.

[66] Bricard R. Mémoire sur la théorie de l'octaèdre articulé [J]. Journal de Mathématiques pures et appliquées, 1897, 3: 113-148.

[67] You Z, Chen Y. Motion structures: deployable structural assemblies of mechanisms [M]. New York: Spon Press, 2014.

[68] Phillips J. Freedom in machinery: screw theory exemplified [M]. Cambridge: Cambridge University Press, 1990.

[69] Wohlhart K. The two types of the orthogonal Bricard linkage [J]. Mechanism and machine theory, 1993, 28(6): 809-817.

[70] Chai W H, Chen Y. The line-symmetric octahedral Bricard linkage and its structural closure [J]. Mechanism and Machine Theory, 2010, 45(5): 772-779.

[71] Chen Y, Chai W H. Bifurcation of a special line and plane symmetric Bricard linkage [J]. Mechanism and Machine Theory, 2011, 46(4): 515-533.

[72] Song C Y, Chen Y, Chen I M. Kinematic Study of the Original and Revised General Line-Symmetric Bricard 6*R* Linkages [J]. Journal of Mechanisms and Robotics, 2014, 6(3): 031002.

[73] Feng H, Chen Y, Dai J S, et al. Kinematic study of the general plane-symmetric Bricard linkage and its bifurcation variations [J]. Mechanism and Machine Theory, 2017, 116: 89-104.

[74] Baker J E. A geometrico-algebraic exploration of Altmann's linkage [J]. Mechanism and Machine Theory, 1993, 28(2): 249-260.

[75] Grodzinski P, M'Ewen E. Link mechanisms in modern kinematics [J]. Proceedings of the Institution of Mechanical Engineers, 1954, 168(1): 877-896.

[76] Wohlhart K. A new 6*R* space mechanism [C]. Proceedings of the 7th World Congress on the Theory of Machines and Mechanisms, Sevilla: IFToMM, 1987: 17-22.

[77] Chen Y, You Z, Tarnai T. Threefold-symmetric Bricard linkages for deployable structures [J]. International journal of solids and structures, 2005, 42(8): 2287-2301.

[78] Huang H, Deng Z, Li B. Mobile assemblies of large deployable mechanisms [J]. Journal of Space Engineering, 2012, 5(1): 1-14.

[79] You Z, Chen Y. Mobile Assemblies Based on the Bennett Linkage [J]. Proceedings of the Royal Society A: Mathematical, Physical and Engineering Sciences, 2005, 461(2056): 1229-1245.

[80] Chen Y, You Z. On Mobile Assemblies of Bennett Linkages [J]. Proceedings of the Royal Society A: Mathematical, Physical and Engineering Sciences, 2008, 464(2093): 1275-1293.

[81] Baker J E. A collapsible network of similar pairs of nested Bennett linkages [J]. Mechanism and Machine Theory, 2013, 59: 119-124.

[82] Lu S, Zlatanov D, Ding X. Approximation of cylindrical surfaces with deployable Bennett networks [J]. Journal of Mechanisms and Robotics, 2017, 9(2): 021001.

[83] Liu S Y, Chen Y. Myard linkage and its mobile assemblies [J]. Mechanism and Machine Theory, 2009, 44(10): 1950-1963.

[84] Qi X Z, Deng Z Q, Ma B Y, et al. Design of large deployable networks constructed by Myard linkages [J]. Key Engineering Materials, 2011, 486: 291-296.

[85] Huang H, Yan Z. Deployed profile synthesis of deployable Bricard mechanism [C]. Proceedings of the 2015 IEEE International Conference on Cyber Technology in Automation, Shenyang: IEEE, 2015: 624-629.

[86] Yang F F, Li J M, Chen Y, et al. A deployable Bennett network in saddle surface [C]. Proceedings of the 14th IFToMM World Congress, Taiwan: IFToMM, 2015: 428-434.

[87] Kiper G, Söylemez E. Regular polygonal and regular spherical polyhedral linkages comprising Bennett loops [M]//Kecskem T A, M L A. Computational Kinematics. Berlin: Springer, 2009: 249-256.

[88] Song X, Deng Z, Guo H, et al. Networking of Bennett linkages and its application on deployable parabolic cylindrical antenna [J]. Mechanism and Machine Theory, 2017, 109: 95-125.

[89] Chen Y, You Z. An extended Myard linkage and its derived 6*R* linkage [J]. Journal of Mechanical Design, 2008, 130(5): 052301.

[90] Huang H, Li B, Zhu J, et al. A new family of Bricard-derived deployable mechanisms[J]. Journal of Mechanisms and Robotics, 2016, 8(3): 034503.

[91] Song X, Guo H, Li B, et al. Large deployable network constructed by Altmann linkages[J]. Proceedings of the Institution of Mechanical Engineers, Part C: Journal of Mechanical Engineering Science, 2017, 231(2): 341-355.

[92] Atarer F, Korkmaz K, Kiper G. Design alternatives of network of Altmann linkages [J]. International Journal of Computational Methods and Experimental Measurements, 2017, 5(4): 495-503.

[93] Zirbel S A, Trease B P, Thomson M W, et al. HanaFlex: a large solar array for space applications [C]. Micro-and Nanotechnology Sensors, Systems, and Applications VII. International Society for Optics and Photonics, Baltimore: SPIE DEFENSE SECURITY, 2015: 94671C.

[94] Miyashita S, Guitron S, Yoshida K, et al. Ingestible, controllable, and degradable origami robot for patching stomach wounds [C]. Proceedings-IEEE International Conference on Robotics and Automation, Sheffield: IEEE, 2016: 909-916.

[95] Felton S, Tolley M, Demaine E, et al. A method for building self-folding machines [J]. Science, 2014, 345(6197): 644-646.

[96] Lee J Y, Kang B B, Lee D Y, et al. Development of a multi-functional soft robot (snUMaX) and performance in robosoft grand challenge [J]. Frontiers in Robotics and AI, 2016, 3: 63.

[97] Boyvat M, Koh J S, Wood R J. Addressable wireless actuation for multijoint folding robots and devices [J]. Science Robotics, 2017, 2(8): eaan1544.

[98] Miyashita S, Guitron S, Ludersdorfer M, et al. An untethered miniature origami robot that self-folds, walks, swims, and degrades [C]. Proceedings of the 2015 IEEE International Conference on Robotics and Automation (ICRA), Seattle: IEEE, 2015: 1490-1496.

[99] Watanabe N, Kawaguchi K I. The method for judging rigid foldability [M]// Lang R J. Origami 4. New York: A K Peters/CRC Press. 2009: 265-276.

[100] Tachi T. Generalization of rigid-foldable quadrilateral-mesh origami [J]. Journal of the International Association for Shell and Spatial Structures, 2009, 50(3): 173-179.

[101] Tachi T. Geometric considerations for the design of rigid origami structures [C]. Proceedings of the International Association for Shell and Spatial Structures (IASS) Symposium, Shanghai: IASS, 2010, 12(10): 458-460.

[102] Wu W, You Z. Modelling rigid origami with quaternions and dual quaternions [J]. Proceedings of the Royal Society A: Mathematical, Physical and Engineering Science, 2010, 466(2119): 2155-2174.

[103] Cai J, Zhang Y, Xu Y, et al. The foldability of cylindrical foldable structures based on rigid origami [J]. Journal of Mechanical Design, 2016, 138(3): 031401.

[104] Liu S, Chen Y, Lu G. Liu S, Chen Y, Lu G. The rigid origami patterns for flat surface [C]. Proceedings of the ASME 2013 International Design Engineering Technical Conferences and Computers and Information in Engineering Conference, Portland: ASME, 2013: V06BT07A039.

[105] Liu S, Lv W, Chen Y, et al. Deployable prismatic structures with rigid origami patterns [J]. Journal of Mechanisms and Robotics, 2016, 8(3): 031002.

[106] Chen Y, Lv W, Li J, et al. An extended family of rigidly foldable origami tubes [J]. Journal of Mechanisms and Robotics, 2017, 9(2): 021002.

[107] Hull T. On the mathematics of flat origamis [J]. Congressus numerantium, 1994: 215-224.

[108] Hull T. The combinatorics of flat folds: a survey [C]. Proceedings of the Third International Meeting of Origami Science, 2002: 29-38.

[109] Lang R J. Twists, Tilings, and Tessellations: Mathematical Methods for Geometric Origami [M]. New York: AK Peters/CRC Press, 2017.

[110] Gattas J M, Wu W, You Z. Miura-base rigid origami: parameterizations of first-level derivative and piecewise geometries [J]. Journal of Mechanical Design, 2013, 135(11): 111011.

[111] Sareh P, Guest S D. Design of isomorphic symmetric descendants of the Miura-ori[J]. Smart Materials and Structures, 2015, 24(8): 085001.

[112] Sareh P, Guest S D. Design of non-isomorphic symmetric descendants of the Miura-ori[J]. Smart Materials and Structures, 2015, 24(8): 085002.

[113] Xie R, Li J, Chen Y. The graded origami structures [C]. Proceedings of the ASME 2015 International Design Engineering Technical Conferences and Computers and Information in Engineering Conference, Boston: ASME, 2015: V05BT08A026.

[114] Evans T A, Lang R J, Magleby S P, et al. Rigidly foldable origami gadgets and tessellations [J]. Royal Society open science, 2015, 2(9): 150067.

[115] Tachi T. One-DOF cylindrical deployable structures with rigid quadrilateral panels [C]. Proceedings of Symposium of the International Association for Shell and Spatial Structures. Evolution and Trends in Design, Valencia: Editorial Universitat Politècnica de València. 2010: 2295-2305.

[116] Tachi T, Miura K. Rigid-foldable cylinders and cells [J]. Journal of the international association for shell and spatial structures, 2012, 53(4): 217-226.

[117] Mousanezhad D, Kamrava S, Vaziri A. Origami-based building blocks for modular construction of foldable structures [J]. Scientific reports, 2017, 7(1): 14792.

[118] Lang R J, Howell L. Rigidly foldable quadrilateral meshes from angle arrays [J]. Journal of Mechanisms and Robotics, 2018, 10(2): 021004.

[119] Liu X, Gattas J M, Chen Y. One-DOF superimposed rigid origami with multiple states [J]. Scientific reports, 2016, 6: 36883.

[120] Yoshimura Y. On the mechanism of buckling of a circular cylindrical shell under axial compression [J]. 1955.

[121] Ma J, You Z. Modelling of the waterbomb origami pattern and its applications [C]. Proceedings of the ASME 2014 International Design Engineering Technical Conferences and Computers and Information in Engineering Conference, American Society of Mechanical Engineers, Buffalo: ASME, 2014: V05BT08A047.

[122] Resch R D. Self-supporting structural unit having a series of repetitious geometrical modules: U.S. Patent 3,407,558 [P]. 1968-10-29.

[123] T Tachi T. Designing freeform origami tessellations by generalizing Resch's patterns [J]. Journal of Mechanical Design, 2013, 135(11): 111006.

[124] Onal C D, Wood R J, Rus D. An origami-inspired approach to worm robots [J]. IEEE/ASME Transactions on Mechatronics, 2013, 18(2): 430-438.

[125] Lee D Y, Kim J S, Kim S R, et al. The deformable wheel robot using magic-ball origami structure [C]. Proceedings of the ASME 2013 International Design Engineering Technical Conferences and Computers and Information in Engineering Conference, American Society of Mechanical Engineers, Portland: ASME, 2013: V06BT07A040.

[126] Zhang K, Qiu C, Dai J S. An extensible continuum robot with integrated origami parallel modules [J]. Journal of Mechanisms and Robotics, 2016, 8(3): 031010.

[127] Fang H, Zhang Y, Wang K W. An earthworm-like robot using origami-ball structures [C]. Proceedings of the Active and Passive Smart Structures and Integrated Systems 2017, International Society for Optics and Photonics, Portland: SPIE DIGITAL LIBRARY, 2017: 1016414.

[128] Lee D Y, Kim S R, Kim J S, et al. Origami wheel transformer: A variable-diameter wheel drive robot using an origami structure [J]. Soft robotics, 2017, 4(2): 163-180.

[129] Tachi T. Simulation of rigid origami [M]// Lang R J. Origami 4. New York: A K Peters/CRC Press, 2009: 175-187.

[130] Yu H, Guo Z, Wang J. A method of calculating the degree of freedom of foldable plate rigid origami with adjacency matrix [J]. Advances in Mechanical Engineering, 2018, 10(6): 1687814018779696.

[131] De Temmerman I N, Mollaert M, Van Mele I T, et al. Design and analysis of a foldable mobile shelter system [J]. International Journal of Space Structures, 2007, 22(3): 161-168.

[132] Cai J, Deng X, Xu Y, et al. Motion analysis of a foldable barrel vault based on regular and irregular Yoshimura Origami [J]. Journal of Mechanisms and Robotics, 2016, 8(2): 021017.

[133] Chen Y, Feng H, Ma J, et al. Symmetric waterbomb origami [J]. Proceedings of the Royal Society of London A: Mathematical, Physical and Engineering Sciences, 2016, 472(2190): 20150846.

[134] Feng H, Ma J, Chen Y, et al. Twist of tubular mechanical metamaterials based on waterbomb origami [J]. Scientific Reports, 2018, 8(1): 9522.

[135] Hull T C, Tachi T. Double-line rigid origami [J]. arXiv preprint arXiv:1709.03210, 2017.

[136] Lang R J, Tolman K A, Crampton E B, et al. A review of thickness-accommodation techniques in origami-inspired engineering [J]. Applied Mechanics Reviews, 2018, 70(1): 010805.

[137] Tachi T. Rigid-foldable thick origami [M]// Wang-Iverson P, Lang R J, Yim M. Origami 5. New York: A K Peters/CRC Press. 2011: 253-264.

[138] Zirbel S A, Lang R J, Thomson M W, et al. Accommodating thickness in origami-based deployable arrays [J]. Journal of Mechanical Design, 2013, 135(11): 111005.

[139] Edmondson B J, Lang R J, Magleby S P, et al. An offset panel technique for thick rigidily foldable origami [C]. Proceedings of the ASME 2014 International Design Engineering Technical Conferences and Computers and Information in Engineering Conference, Buffalo: ASME, 2014: V05BT08A054.

[140] Morgan M R, Lang R J, Magleby S P, et al. Towards developing product applications of thick origami using the offset panel technique [J]. Mechanical Sciences, 2016, 7(1): 69.

[141] Hoberman C. Folding structures made of thick hinged sheets: U.S. Patent 7,794,019 [P]. 2010-9-14.

[142] Hoberman C. Reversibly expandable structures: U.S. Patent 4,981,732 [P]. 1991-1-1.

[143] Ku J S, Demaine E D. Folding flat crease patterns with thick materials [J]. Journal of Mechanisms and Robotics, 2016, 8(3): 031003.

[144] Tolman K A, Lang R J, Magleby S P, et al. Split-vertex technique for thickness-accommodation in origami-based mechanisms [C]. Proceedings of the ASME 2017 International Design Engineering Technical Conferences and Computers and Information in Engineering Conference, Cleveland: ASME, 2017: V05BT08A054.

[145] Lang R J, Nelson T, Magleby S, et al. Thick rigidly foldable origami mechanisms based on synchronized offset rolling contact elements [J]. Journal of Mechanisms and Robotics, 2017, 9(2): 021013.

[146] Pehrson N A, Magleby S P, Lang R J, et al. Introduction of monolithic origami with thick-sheet materials [C]. Proceedings of IASS Annual Symposia. International Association for Shell and Spatial Structures (IASS), Tokyo: IASS, 2016, 2016(13): 1-10.

[147] Pehrson N A, Magleby S P, Howell L L. An origami-based thickness-accommodating bistable mechanism in monolithic thick-sheet materials [C]. 2018 International Conference on Reconfigurable Mechanisms and Robots (ReMAR), Delft: IEEE, 2018: 1-7.

[148] Wang C, Li J, You Z. A kirigami-inspired foldable model for thick panels [M]// Lang R J, Bolitho M, You Z. Origami 7. St Albans: Tarquin, 2018, 3: 715-730

[149] Dai J S, Rees Jones J. Kinematics and mobility analysis of carton folds in packing manipulation based on the mechanism equivalent [J]. Proceedings of the Institution of Mechanical Engineers, Part C: Journal of Mechanical Engineering Science, 2002, 216(10): 959-970.

[150] Cannella F, Dai J S. Crease stiffness and panel compliance of carton folds and their integration in modelling [J]. Proceedings of the Institution of Mechanical Engineers, Part C: Journal of Mechanical Engineering Science, 2006, 220(6): 847-855.

[151] Dai J S, Cannella F. Stiffness characteristics of carton folds for packaging [J]. Journal of mechanical design, 2008, 130(2): 022305.

[152] Qiu C, Aminzadeh V, Dai J S. Kinematic and stiffness analysis of an origami-type carton [C]. Proceedings of the ASME 2013 International Design Engineering Technical Conferences and Computers and Information in Engineering Conference, Portland: ASME, 2013: V06BT07A026.

[153] Winder B G, Magleby S P, Howell L L. Kinematic representations of pop-up paper mechanisms [J]. Journal of Mechanisms and Robotics, 2009, 1(2): 021009.

[154] Leal E R, Dai J S. From origami to a new class of centralized 3-DOF parallel mechanisms [C]. Proceedings of the ASME 2007 International Design Engineering Technical Conferences and Computers and Information in Engineering Conference, Las Vegas: ASME, 2007: 1183-1193.

[155] Wei G, Dai J S. Geometry and kinematic analysis of an origami-evolved mechanism based on artmimetics [C]. Proceedings of the 2009 ASME/IFToMM International Conference on Reconfigurable Mechanisms and Robots, London: IEEE, 2009: 450-455.

[156] Zhang K, Fang Y, Fang H, et al. Geometry and constraint analysis of the three-spherical kinematic chain based parallel mechanism [J]. Journal of Mechanisms and Robotics, 2010, 2(3): 031014.

[157] Wei G, Dai J S. Origami-inspired integrated planar-spherical overconstrained mechanisms [J]. Journal of Mechanical Design, 2014, 136(5): 051003.

Appendix

A. Vertex-splitting on diamond origami pattern corresponding to section 4.3

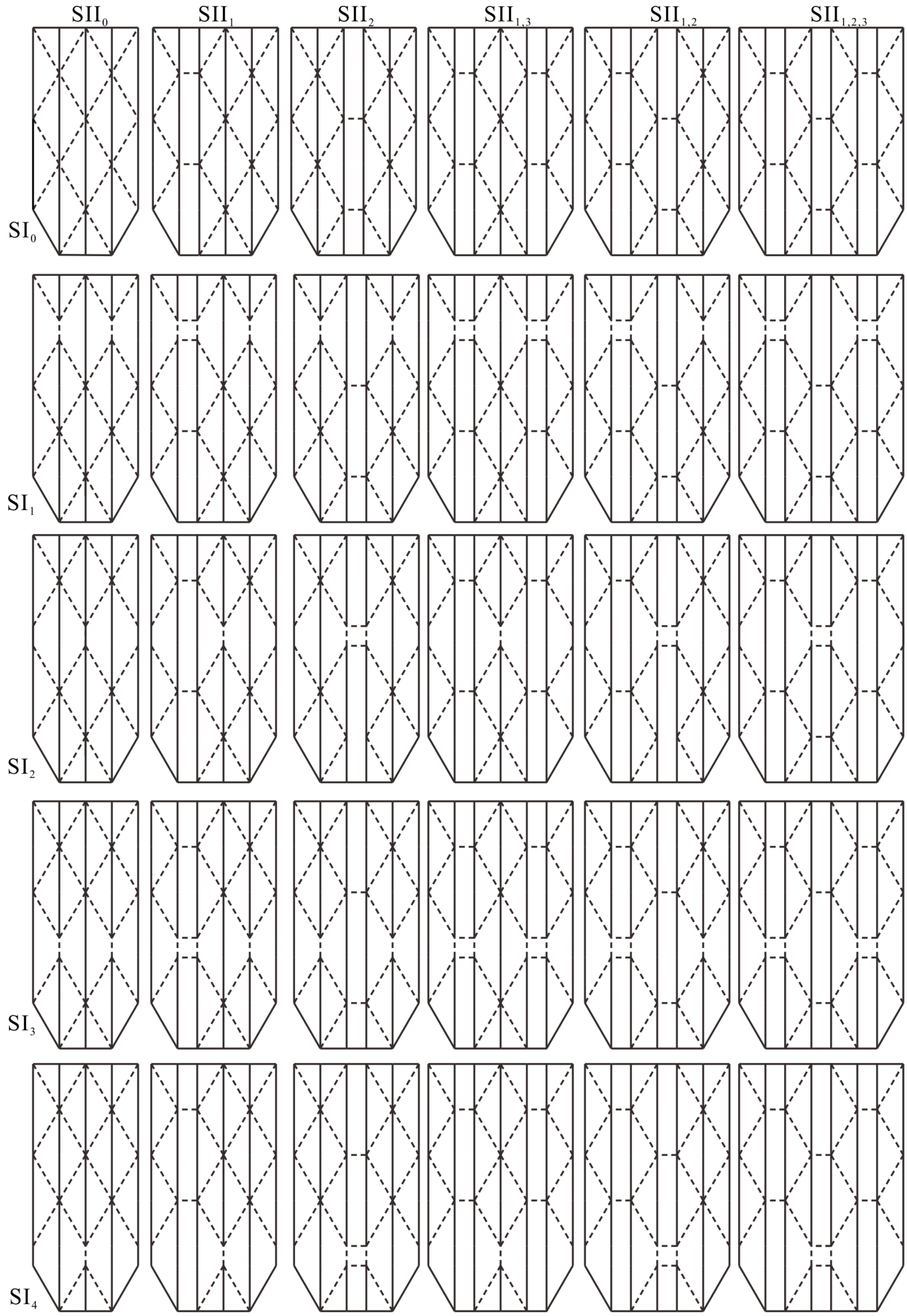

Fig. A1 Cases of vertex-splitting on diamond origami pattern with six vertices.

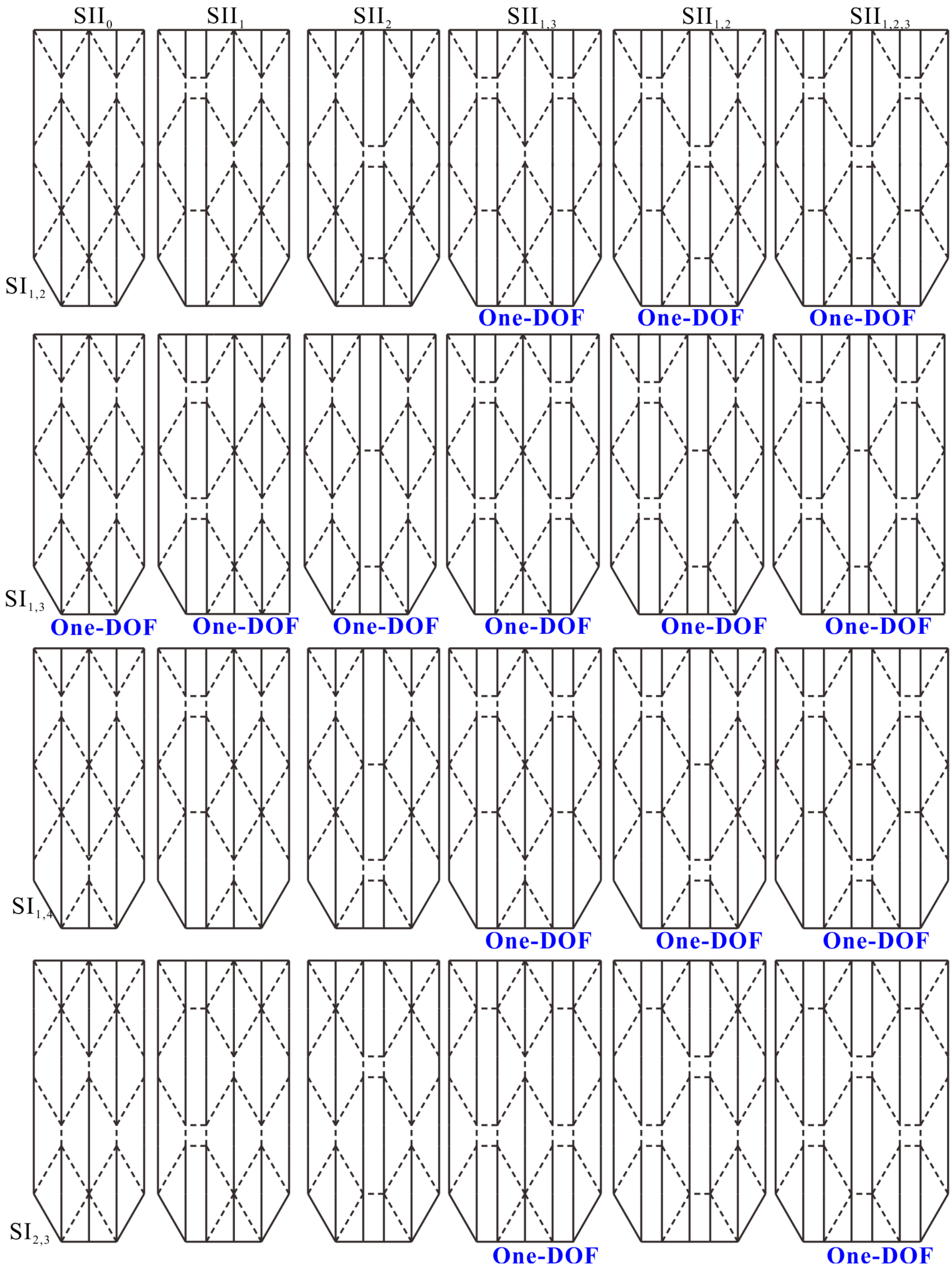

Fig. A1 Cases of vertex-splitting on diamond origami pattern with six vertices (Continued).

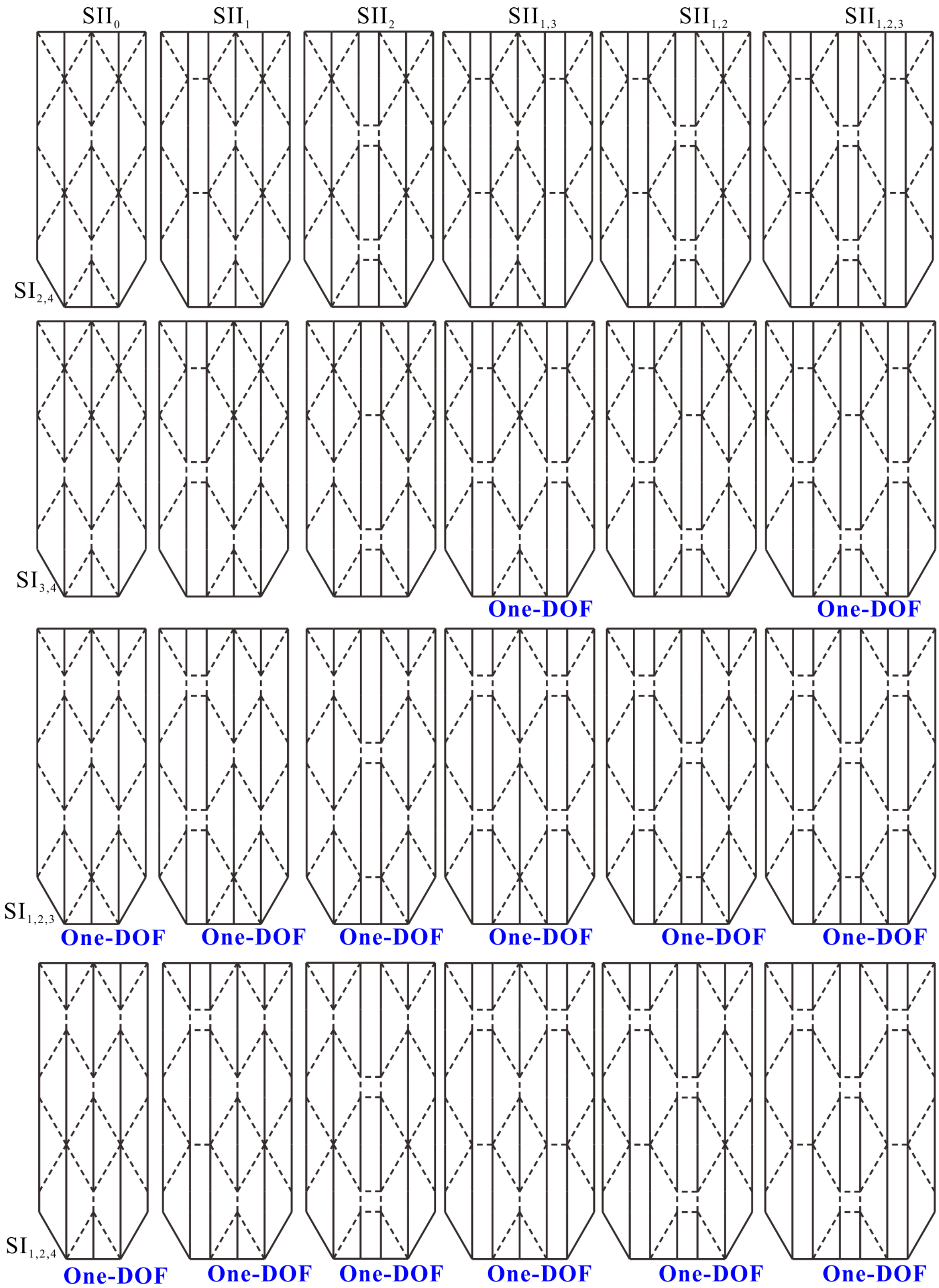

Fig. A1 Cases of vertex-splitting on diamond origami pattern with six vertices (Continued).

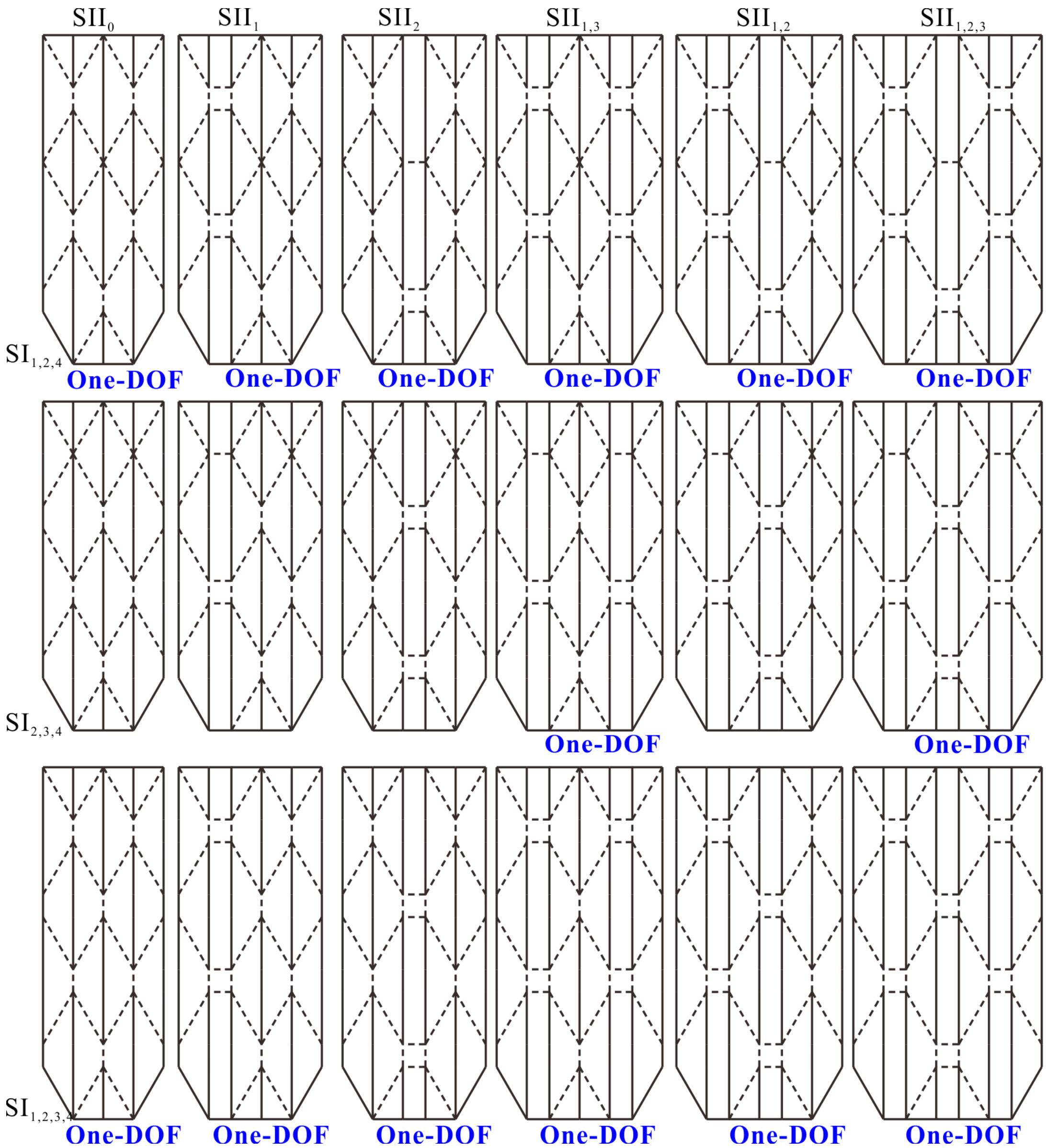

Fig. A1 Cases of vertex-splitting on diamond origami pattern with six vertices (Continued).

中文大摘要

可展结构是一种几何形状可变的结构，其可以实现从紧密折叠状态到可控展开状态的变化。该类结构在折叠状态下便于存贮和运输，在展开状态下执行正常工作任务。可展结构以其良好的折叠特性广泛应用于各类工程领域中，如航空航天领域的卫星天线、太阳能电池板和飞机机翼，土木工程领域的帐篷、穹顶和桥梁，生物医学领域的折纸血管支架和手术钳，以及机器人领域等。虽然可展结构种类繁多，但根据其组成构件形态的差异可分为两类：由杆单元或框架单元组成的杆状可展结构和由连续面单元构成的面状可展结构。其中，由连杆机构组成的可展机构网格和由面结构组成的折纸，具有较少的自由度和良好的折叠特性，而备受相关领域研究人员的关注。

连杆机构可以作为构成大型可展机构网格的单元，并将其良好的可展特性传递给由其构成的可展机构网格。常见的可展机构网格单元主要包括经典的剪式单元和基于单自由度单环空间过约束连杆机构构造的单元。剪式单元具有运动同步可靠、折叠紧凑、用料经济等优点，在大型可展结构，如屋顶、帐篷、天线等设计中应用最为广泛。单自由度单环空间过约束连杆机构的自由度数不遵循 Grübler-Kutzbach 准则，其特殊的几何条件保证其正常运动，常见的主要有 Bennett 机构、Myard 机构和 Bricard 机构。此类机构能够以较少的杆件产生复杂的三维运动，且其过约束几何特征能够为可展结构提供额外的刚度，因此如何设计由此类机构组成可展机构网格也成为了相关学者的研究热点。几何覆盖法的提出为以空间过约束连杆机构为基本单元构造可展机构网格奠定了基础。然而，求解复杂非线性方程以获得可展机构网格中各连杆机构间的运动协调条件是设计可展机构网格的难点。

折纸是一门通过折叠将纸张变成三维结构的艺术，它根据预先设计的折痕图案折成不同的形状。其中一些折纸可以从大尺度结构折叠成小尺度结构，因而应用于可展结构的设计中，近来相关的研究证实折纸可以应用于如超材料、机器人等领域。刚性折纸是一种特殊的折纸，在折叠过程中各个面可绕折痕旋转且面内不发生变形，可以采用高刚度的材料设计制造此折纸。其中单自由度折纸（如 Miura-ori 折纸）以其结构简单、易于控制的特点被广泛研究；多自由度折纸则以其可变的展开状态在变形机器人的设计中应用广泛。然而，如何设计单自由度折纸图案以及精确控制多自由度折纸的运动依然是一个巨大挑战。

基于折纸设计的可展结构一般可以简化为零厚度折纸进行分析。将刚性折纸的折痕和刚性面分别视为转动副和杆件，单顶点刚性折纸可以等价成为一个球面连杆机构，多个顶点的刚性折纸可视为由多个球面连杆机构组成的网格，因此，

可以引入机构学相关理论分析刚性折纸。然而，在某些对可展结构的强度或刚度有要求的场合，忽略材料的厚度会引起模型运动过程中的物理干涉，进而导致可展结构无法折叠，因此引出厚板折叠问题。偏移铰链法利用空间过约束连杆机构替换原有球面连杆机构建立厚板折纸的运动模型，不仅完美解决了厚板折纸的干涉问题，还建立起了空间过约束机构与刚性折纸的运动等价关系。以厚板折纸为桥梁，研究刚性折纸与空间过约束机构之间的关系，不仅可以从折纸的角度出发设计空间机构网格，还可以在空间机构网格的运动分析中拓宽折纸的设计空间。

本文旨在以厚板折纸为基础研究空间连杆机构与刚性折纸之间的关系，并设计新型由空间连杆机构组成的可展机构网格、刚性折纸和厚板折纸。

本文首先从四折痕折纸出发提出了一种基于厚板折纸的转化法，实现了四折痕折纸到 Bennett 机构的转化，发现了一种由 Bennett 机构组成的新型可展机构网格。其次，在六折痕 diamond 折纸中应用基于厚板折纸的转化法，获得了一种由面对称 Bricard 机构组成的可展机构网格，并构造了在展开状态具有平整表面、折叠状态是螺旋形的 diamond 厚板折纸。最后，针对 diamond 折纸具有多自由度的缺陷，提出了一种减少折纸自由度数的顶点拆分法，并据此构造了多种单自由度折纸；研究了 Waldron 混联六杆机构的构造过程与其对应厚板折纸模型的几何形状变化的关系，通过去除铰链构造具有平整展开表面的厚板折纸。本文工作主要包括如下三部分：

- **基于四折痕折纸设计的由 Bennett 机构组成的可展机构网格**

采用偏移铰链法设计的厚板折纸与零厚度刚性折纸及由空间过约束机构组成的网格运动等价，因此可将厚板折纸视为研究零厚度刚性折纸与该机构网格关系的桥梁。从已知的四种四折痕折纸图案出发建立其相应的厚板折纸模型，并设计形成由 Bennett 机构组成的可展机构网格。

本文**第二章**以单顶点四折痕折纸、单顶点厚板折纸以及 Bennett 机构的运动等价性为基础，建立了从四折痕折纸到 Bennett 机构的转化法。将该转化法应用于多顶点四折痕折纸中，得到了一系列由 Bennett 机构组成的可展机构网格。

首先选取具有平面可折叠特性的单顶点四折痕折纸为研究对象。该折纸相对的两个扇形角之和为 180 度。将刚性折纸的折痕和刚性面分别视为转动副和杆件，其运动与球面四杆机构等价。然后，利用偏移铰链法构造出该折纸对应的厚板形态，观察发现厚板折纸的四条铰链轴线不再交于一点，因此该厚板折纸可视为杆长与厚板厚度相关的 Bennett 机构。通过建立适当的 D-H 标记，获得厚板折纸的扇形角、板厚与 Bennett 机构的扭角、杆长之间的关联关系。之后，沿相邻铰链轴线的公法线方向用直杆替代原有的厚板，并将其连接到相邻的铰链，构造出了与原有厚板折纸运动等价的、具有杆件形式的 Bennett 机构。由此，提出了四折痕折纸到 Bennett 机构的转化法。此外，零厚度刚性折纸(其相应的球面机构)

和厚板折纸(其相应的 Bennett 机构)具有相同的拓扑结构，文中引入拓扑图来描述杆件之间的本质关系，并将其应用于多顶点折纸的分析与转化中。

对于多顶点折纸，首先以包含四个四折痕顶点的 Miura-ori 折纸为例，建立其厚板折纸模型。通过分析四个顶点对应 Bennett 机构组成闭环的相对连接关系，确定了各厚板上连接铰链在其厚度方向上的分布顺序。将厚板转化为杆件，并按顺序将铰链布置到相应的杆件上，建立了与厚板折纸运动等价的、由四个 Bennett 机构组成的可展机构网格。分析该网格中机构扭角的关系，发现 Miura-ori 厚板折纸对应的是由具有等杆长特征的 Bennett 机构组成的可展机构网格。之后将基于厚板折纸的转化法应用到互补型折纸中，发现从互补型折纸的三种不同的山谷线排布图案中分别得到由不同负杆长特征的 Bennett 机构组成的可展机构网格。最后以 identical linkage-type 折纸为对象，应用折纸到机构网格的基于厚板折纸的转化法，形成了一种新型的 Bennett 机构网格。对其开展的运动协调性分析进一步保证了其可动的特性。

建立起四折痕刚性折纸到 Bennett 机构网格的基于厚板折纸的转化法，为从折纸的角度设计可展机构网格提供了一种新思路。研究获得 Bennett 机构网格的运动协调条件也扩展了可展机构网格的设计空间。

- **Diamond 厚板折纸及其对应的由 Bricard 机构组成的可展机构网格**

利用折纸到机构的基于厚板折纸的转化方法，从四折痕厚板折纸出发可构造出由 Bennett 机构组成的可展机构网格；对于具有面对称特征的六折痕厚板折纸（如典型的 diamond 和 waterbomb 厚板折纸），其每个顶点的运动与一个面对称 Bricard 机构运动等价，因此可以类似的应用基于厚板折纸的转化法构造由面对称 Bricard 机构组成的可展机构网格。与此同时，对于这种网格的运动协调性分析可以用来拓宽厚板折纸的可行设计空间。

在第三章中，我们首先对具有面对称特征的单顶点 diamond 厚板折纸应用基于厚板折纸的转化法，将其厚板转化为杆件并连接相应的铰链，构造出运动等价的面对称 Bricard 机构。在适当的 D-H 标记下，建立了单顶点六折痕厚板折纸的扇形角、板厚与面对称 Bricard 机构扭角、杆长间的关系方程。然后对包含有四个顶点的 diamond 厚板折纸，分析其各顶点处面对称 Bricard 机构的连接关系，确定连接铰链在板厚方向上的分布顺序，进而将其转化为包含四个相同面对称 Bricard 机构的 diamond 机构网格，且该网格与 diamond 厚板折纸运动等价。根据厚板与机构间参数的对应关系，给出了构造此机构网格的运动协调条件。

从一般面对称 Bricard 机构的闭环方程出发，选取包含七个面对称 Bricard 机构的 diamond 机构网格为研究对象，分析其运动协调性。根据机构的分布特点，选择共用同一杆件的三个面对称 Bricard 机构形成的组合进行运动协调条件的分析，结果表明三个面对称 Bricard 机构可以组合形成八种运动类型。采用其中一

种运动类型，求得了两组构造面对称 Bricard 机构网格的运动协调条件，并设计出两种具有不同扭角条件的面对称 Bricard 机构网格。

借助 diamond 厚板折纸与面对称 Bricard 机构几何参数的关系方程，从一组 Bricard 机构网格的运动协调条件中得到构造 diamond 厚板折纸更一般的几何条件。依据此条件分析优化 diamond 厚板折纸的几何参数，构造了不同外形的厚板折纸。其中，通过改变厚板折纸的扇形角，确定了具有渐变特征的 diamond 型厚板折纸的构造条件。基于机构杆长与厚板折纸板厚之间的关系方程，通过改变厚板折纸的板厚，构造出具有平整展开表面的 diamond 厚板折纸。综合改变折纸扇形角和板厚构造出一种新型的具有平整展开表面和螺旋折叠构型的厚板折纸。该折纸可以通过合理的参数设计获得折叠结构紧凑、可无限延展的可展结构，有利于厚板折纸在工程中的应用。

此外，通过分析三个面对称 Bricard 机构的组合，获得八种运动状态下的运动协调条件，其中有五种是不同的类型。通过给定设计参数，构造了五种运动类型下的机构网格模型。这些模型可以根据需要组合到一起，通过验证运动协调性可以作为机构单元进一步构造大型的 Bricard 机构网格。

- **基于刚性折纸的节点拆分法**

拥有面对称运动特征的 diamond 厚板折纸可以实现单自由度运动，其对应的零厚度折纸所具有的六折痕顶点可以视为三自由度的球面六杆机构，因此包含多顶点的零厚度 diamond 折纸是多自由度的。基于此类折纸、采用薄板材设计制造出的可展结构具有多自由度的特点，因此获得所需的面对称运动往往比较困难。**第三章**中以 diamond 折纸为研究对象，提出了一种减少自由度数的顶点拆分法，在多顶点 diamond 折纸上应用该方法获得了一系列运动等价的单自由度刚性折纸。为获得具有平整展开表面的厚板折纸，基于 Waldron 混联六杆机构的构造过程，得出四折痕厚板折纸可以通过去除部分铰链来获得单自由度的六折痕厚板折纸，构造了多种具有平整展开表面的厚板折纸。

从单顶点 diamond 型折纸出发，根据其山谷线排布的对称特性提出了顶点拆分的两种方式：SI 沿平行于对称折痕方向拆分和 SII 沿垂直于对称折痕方向拆分。两种拆分方式应用到单顶点 diamond 型折纸中共获得三种类型的折纸单元：沿平行于对称折痕方向拆分形成包含两个相同四折痕顶点的 DI 型折纸，沿垂直于对称折痕方向拆分形成包含两个相同五折痕顶点的 DII 型折纸，沿两个方向分别拆分可以获得包含有四个相同四折痕顶点的 DI-II 型折纸，其中 DI 和 DI-II 型折纸具有单自由度。此外，当 DII 型折纸中的五折痕顶点引入面对称约束条件时，这三类折纸与在线面对称约束条件下的单顶点 diamond 折纸具有等价的面对称运动特性。

对于包含六个相同六折痕顶点的 diamond 折纸，其各顶点均可应用顶点拆分

法形成 DI、DII 和 DI-II 三类折纸单元。为得到刚性折纸，分别采用 SI、SII 方式拆分整行、整列的顶点，共得到 96 种不同的拆分结果。通过总结分析，从中获得了包含四折痕顶点、五折痕顶点及六折痕顶点的具有单自由度特征的基本折纸图案。由四个四折痕顶点组成的、具有面对称特征的基本折纸图案可以看作是由四个球面四连杆机构组成的单自由度面对称环路。包含有四折痕顶点和一个五折痕顶点的基本折纸图案，四折痕顶点可以为该五折痕顶点提供两个约束使整个基本折纸图案也具有单自由度特征。此外，由四折痕顶点与两个五折痕顶点构成的基本折纸图案、由四折痕顶点与一个六折痕顶点分别通过三条折痕和四条折痕构成的基本折纸图案、由四折痕顶点与五折痕顶点再与六折痕顶点构成的基本折纸图案，这些折纸中所有顶点的运动都可以通过给定一个输入来确定，因此，这些图案都是单自由度的基本折纸图案。利用这些具有单自由度特征的基本折纸图案，可以确定 96 种不同的拆分结果中有 42 种情况是单自由度的。剩余的折纸中，各折纸的单自由度基本折纸图案不能提供足够用于确定所有顶点运动的约束，因此都是多自由度的。

由两个具有平面可折叠特性的四折痕顶点、通过共用一个同类型的折痕组成的折纸，可以利用偏移铰链法构造对应的厚板折纸。该厚板折纸包含两个四折痕顶点，可以应用基于厚板的转化法得到由两个 Bennett 机构通过一个铰链连接的机构组合。根据 Waldron 混联六杆机构的构造方法，去除该机构组合中两个 Bennett 机构的共用铰链，得到运动等价的 Waldron 混联六杆机构；去除厚板折纸上两个四折痕顶点共用的铰链和厚板上的台阶，产生了与 Waldron 混合型六杆机构运动等价的六折痕厚板。由此提出了四折痕厚板折纸去除铰链构造运动等价六折痕厚板折纸的方法。在包含四折痕与六折痕顶点的厚板折纸中，相邻四折痕顶点间的共用铰链及其厚板形成了该厚板折纸在展开状态时的台阶。通过去除铰链，再根据 Waldron 混联六杆机构的构造条件改变相应的板厚，可以构造一种具有平整展开表面的单自由度厚板折纸。此外，通过去掉 Tachi-Miura 型厚板折纸、identical linkage-type 厚板折纸的部分铰链，再分别修改对应厚板的板厚去除厚板的台阶，构造两种具有平整展开表面的单自由度厚板折纸。

应用顶点拆分法可在保证折纸对称运动的前提下，从 diamond 型折纸中构造了一系列单自由度折纸。包含有四折痕、五折痕和六折痕顶点的混合型单自由度折纸的产生为单自由度折纸的设计提供了新思路。此外，通过去除铰链构造具有平整展开表面的单自由度厚板折纸，有利于厚板折纸的工程应用。

- **结论与展望**

本文着眼于机构学与折纸科学的交叉融合，通过研究空间机构网格、厚板折纸与刚性折纸之间的内在关系，提出了折纸到可展机构网格的基于厚板折纸的转化法、减少折纸自由度的顶点拆分方法，为设计新型可展机构网格、刚性折纸、

厚板折纸提供了新途径。

此外，本文的研究工作还可以在如下几方面进行进一步的深入研究：

（1）刚性折纸到可展机构网格的基于厚板折纸的转化法可以扩展应用在更多的刚性折纸中，如 waterbomb 折纸和 Resch 折纸，从而构造更多的由空间过约束机构组成的可展机构网格。此外，该转化法可以应用在多层刚性折纸到可展机构网格的转化中，以获得由多层机构组成的机构网格，如应用于多层 Miura-ori 折纸中。对于已经讨论的四折痕折纸中，发现存在一种 Bennett 机构网格未与已知折纸相对应，因此，此机构网格可能对应一种新型的折纸，后续可以对此开展进一步的研究。

（2）在研究 diamond 厚板折纸及其对应的面对称 Bricard 机构网格中，单顶点六折痕的 diamond 折纸拥有三个自由度和线面对称特性。文中只讨论了折纸在面对称运动条件下的厚板折纸形式。当该折纸引入线对称运动条件时，其厚板折纸形式可以产生线对称 Bricard 机构网格。

（3）在拆分折纸顶点减少自由度的研究中，针对 diamond 折纸提出了两种拆分顶点的方式，同时构造了一系列与 diamond 折纸具有等价对称运动的单自由度折纸。如何扩大顶点拆分法的应用范围，提出一般化的顶点拆分法以减少其它折纸的自由度数需要进一步研究。具体包括：第一，改变拆分顶点的方向和增加折痕的方向；第二，计算应用一般化的顶点拆分法获得的折纸的自由度；第三，通过研究增加或切开折痕与折纸自由度的关系，将拆分顶点获得的非刚性折纸转化成为单自由度的折纸。

（4）在厚板折纸上通过去除部分铰链得到具有平整展开表面的厚板说明了由两个 Bennett 机构构造 Waldron 混联六杆机构的过程可以影响厚板折纸形状的变化。对于其它基于 Bennett 机构构造的机构，如 Goldberg 五杆机构和 Goldberg 六杆机构，其构造过程可能会产生更多的新型厚板折纸。

（5）本文仅在机构网格和刚性折纸方面开展理论研究。并未考虑机构网格中杆件的截面积与厚板折纸中连接处的铰链数对厚板强度和刚度的影响，以及制造误差对机构运动的影响。此外，在工程应用中，可展结构的目标工作状态和折叠体积是其设计的关键参数，因此可展机构网格与刚性折纸的设计参数与目标工作状态和折叠体积之间的关联关系也需要进一步的研究。

关键词：刚性折纸，厚板折纸，机构网格，Bennett 机构，Bricard 机构，转化法，顶点拆分法

Publications and Research Projects during PhD's Study

Papers:

[1] Zhang X, Chen Y, Mobile assemblies of Bennett linkages from four-crease origami patterns [J], Proceedings of the Royal Society A: Mathematical, Physical and Engineering Science, 2018, 474: 20170621.

[2] Zhang X, Chen Y, The diamond thick-panel origami and the corresponding mobile assemblies of plane-symmetric Bricard linkages [J]. Mechanism and Machine Theory, 2018, 130: 585-604.

[3] Xu R, Zhang X, Ma J, Chen Y, Cao Y, and You Z, Folding a rigid flat surface around a square hub [C]. Proceedings of the ASME 2018 International Design Engineering Technical Conferences and Computers and Information in Engineering Conference, American Society of Mechanical Engineers, 2018: V05BT07A060.

[4] Zhang X, Chen Y, Vertex-Splitting on Diamond Origami Pattern [J], Journal of Mechanisms and Robotics, Under Review.

Research Projects Participated in:

[1] The Excellent Young Scientists Fund, National Natural Science Foundation of China, Kinematics of Mechanism and Motion Structures (Grant No. 51422506)

[2] The National Natural Science Foundation General Program, Essential Design Theory Research of the Deployable Structures in the Reconfigurable Robots (Grant No. 51275334)

Acknowledgements

My deepest gratitude goes first and foremost to Prof. Yan Chen, my supervisor, for her constant encouragement and patient guidance throughout my PhD's study. Her constructive suggestions and valuable guidance towards my work and life have been the driving force to complete my research and life compass to realize my bright future. Furthermore, her patience and generosity with students, her enthusiasm and rigorous attitude with academic research, and her immense knowledge will continue to influence my future work and life.

I would also like to thank Prof. Jiayao Ma and Prof. Zhong You for their advices and help on my research, Prof. Rongjie Kang, Prof. Zhibin Song and Ms. Yunyan Wang for their kind help. Appreciation also goes to Miss Huijuan Feng, Mr. Fufu Yang, Mr. Jeff Lee, Mr. Zufeng Shang and Miss Mengyan Shi. Discussions with them widen my vision and deepen my understanding of the research. Meanwhile, I would like to thank my colleagues in Motion Structure Laboratory, in particular Miss Shixi Zang, Mr. Rui Peng, Mr. Weilin Lv, Mr. Jichao Song, Mr. Xuesong Chen, Miss Xiaochen Yang, Mr. Yuanqing Gu, Mr. Mingyuan Yang, Mr. Linfeng Zhang and Mr. Degao Hou for their friendly help and contribution to many unforgettable occasions. Also I would like to my friends, in particular Mr. Kai Zhang, Mr. Xiangfeng Zhang for helping me to go through many hard times in the study life.

Scholarship Fund by China Scholarship Council, the financial support by the National Natural Science Foundation of China (Projects 51275334, 51290293, 51422506, 51535008 and 51721003), by the Ministry of Science and Technology of China (Project 2014DFA70710), and the University PhD Scholarship by Tianjin University are also gratefully acknowledged.

Finally, I would like to express my thanks to my parents, my grandparents and my elder sister for their encouragement, support and confidence in me, and give special thanks to my dear wife Qingfeng Luan for her patience, encouragement and love. All of them give me courage and belief to overcome any difficulty in my study and life.